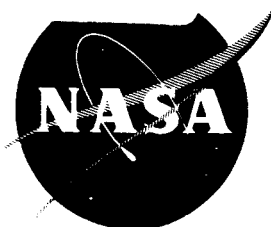


N64-31011
(ACCESSION NUMBER)
135
(PAGES)
NASACR-54164
(NASA CR OR TMX OR AD NUMBER)

(THRU)
1
(CODE)
27
(CATEGORY)

NASA CR-54104
RAD-TR-64-32



ELECTROTHERMAL ENGINE RESEARCH
AND DEVELOPMENT

prepared for

NATIONAL AERONAUTICS AND SPACE ADMINISTRATION

CONTRACT NAS 3-4101

OTS PRICE

XEROX \$ 4.00 FS
MICROFILM \$ 0.75 mf.

RESEARCH AND ADVANCED DEVELOPMENT DIVISION
AVCO CORPORATION
Wilmington, Massachusetts

NOTICE

This report was prepared as an account of Government sponsored work. Neither the United States, nor the National Aeronautics and Space Administration (NASA), nor any person acting on behalf of NASA:

- A.) Makes any warranty or representation, expressed or implied, with respect to the accuracy, completeness, or usefulness of the information contained in this report, or that the use of any information, apparatus, method, or process disclosed in this report may not infringe privately owned rights; or
- B.) Assumes any liabilities with respect to the use of, or for damages resulting from the use of any information, apparatus, method or process disclosed in this report.

As used above, "person acting on behalf of NASA" includes any employee or contractor of NASA, or employee of such contractor, to the extent that such employee or contractor of NASA, or employee of such contractor prepares, disseminates, or provides access to, any information pursuant to his employment or contract with NASA, or his employment with such contractor.

Requests for copies of this report should be referred to

National Aeronautics and Space Administration
Office of Scientific and Technical Information
Attention: AFSS-A
Washington, D. C. 20546

CASE FILE COPY

SUMMARY REPORT

ELECTROTHERMAL ENGINE RESEARCH AND DEVELOPMENT

PHASE I

Prepared for

NATIONAL AERONAUTICS AND SPACE ADMINISTRATION

July 20, 1964

CONTRACT NAS 3-4101

Technical Management
NASA Lewis Research Center
Cleveland, Ohio
Electric Propulsion Office
Harold Ferguson

RESEARCH AND ADVANCED DEVELOPMENT DIVISION
AVCO CORPORATION
Wilmington, Massachusetts

ELECTROTHERMAL ENGINE RESEARCH AND DEVELOPMENT

ABSTRACT

31011
A 3-kw resistojet thruster based on a wire coil heat exchanger was developed. In a 293-hour endurance test the thruster used a propellant flow rate of 0.065 gram/second of hydrogen and produced a specific impulse of 840 seconds at an overall efficiency of 67 percent with an input power of 3 kw.

Data are presented on the compatibility of tungsten, molybdenum, and boron nitride in a hydrogen flow at temperatures in the range 2,000° to 3,000°K.

The thruster supersonic nozzle design was based on an analytical study which included the effects of boundary layer growth. An area ratio of 30 at a conical expansion total angle of 30 degrees was chosen.

Author

ELECTROTHERMAL ENGINE RESEARCH AND DEVELOPMENT

Research and Advanced Development Division

Avco Corporation

SUMMARY

The objective of this first phase of the electrothermal engine program was the development of a thruster characterized by the performance parameters: input power, 2 to 3 kw; specific impulse, 800 to 950 seconds; overall efficiency, 60 to 70 percent. A resistojet thruster for operation in this performance range was developed and life tested.

The basic heat exchanger is a cylindrical chamber containing a set of 5 series-connected wire coils. Each coil comprises 4 parallel connected 0.015-inch diameter wires. The wire material is an alloy of 75 percent tungsten with 25 percent rhenium. The overall wire length is approximately 70 inches. This heat exchanger design offers several advantages: (1) the electrical resistance of the heater at operating temperature is of the order of one ohm, which is sufficient to keep lead losses at a low level, (2) the configuration can be readily modified by changing the overall length or diameter of the wires to suit the electrical characteristics of the power supply, without requiring major design changes, and (3) the coils are easily fabricated from off-the-shelf material. The major drawback which had been thought to be associated with the wire coil concept is wire evaporation leading to thruster failure, but this has turned out to be a relatively unimportant consideration at a specific impulse level of 840 seconds.

The major experimental difficulties are centered around boron nitride which appears to be the most suitable high temperature electrical insulator. The evaporation rate of boron nitride at temperatures in the 2,000°K range is unacceptable for thruster operation over periods of weeks or months; in addition, boron nitride in contact with tungsten or molybdenum at high temperatures forms boride layers in the metals; these have undesirable characteristics including low melting points. The physical design of the thruster has been adjusted so that insulators are not required at the high temperature locations. At lower temperatures, of the order of 1500°K, boron nitride is satisfactory.

An analytical study was made of the supersonic nozzle, including the effects of boundary layer growth and with the assumption of frozen flow. The theoretical performance curves for area ratios to 60 yielded no maximum. However, the calculated performance improvement in going from an area ratio of 30 to one of 60 was quite small, and beyond the capability of the thrust measuring system to detect. An area ratio of 30 and a conical nozzle angle of 30 degrees were selected.

The measured performance of the resistojet thruster agrees with theoretical estimates.

A thruster developed during this program was life tested for 293 hours at an efficiency of 67 percent. The propellant (hydrogen) specific impulse was 840 seconds at the 3-kw input power level.

CONTENTS

I.	Introduction	1
II.	Thruster Design	2
	A. Materials Selection	2
	B. Wire Coil Heat Exchanger Design	5
	C. Nozzle Design	7
	D. Engine Design	9
	E. Tungsten Sphere Heat Exchanger	25
III.	Thruster Performance	32
	A. Performance Measurements	32
	B. Voltage-Current Characteristics	39
IV.	Endurance Tests	42
	A. 50-Hour Test, Mark III, Mod 3	42
	B. 293-Hour Test, Mark III, Mod 4	42
	C. Analysis of Endurance Test Performance	46
V.	Applied Research	51
	A. Impact Pressure Profile	51
	B. Pressure Tap Engine	52
VI.	Program Direction	62
VII.	References	63
Appendixes		
	A. Recrystallization and Grain Growth	67
	B. Boride Formation	77
	C. Test System and Experimental Error	86
	D. Heat Transfer	88
	E. Nozzle Design	97
	F. Bibliography of References on Boron Nitride	123

ILLUSTRATIONS

Figure	1	Tungsten Evaporation Rate Per Unit Wire Length versus Wire Temperature	3
	2	Wire Current versus Wire Radiative Equilibrium Temperature	6
	3	Optimum Performance Variation with Geometric Area Ratio	8
	4	Mark II, Mod 1 Thrustor Design	10
	5	Mark II, Mod 2 Thrustor Design	12
	6	Mark II, Mod 2 Thrustor, Disassembled	13
	7	Mark II, Mod 2 Thrustor, Assembled	14
	8	Mark II, Mod 3 Thrustor Design	16
	9	Mark III, Mod 1 Thrustor Design	18
	10	Mark III, Mod 1 Thrustor, Disassembled	19
	11	Mark III, Mod 1 Thrustor, Assembled	20
	12	End View of Boron Nitride Wire Holder	21
	13	Mark III, Mod 2 Thrustor Design	22
	14	Mark III, Mod 3 Electrical Connections	26
	15	Mark III, Mod 3 Thrustor Design.....	27
	16	Cross Section of Mark III, Mod 3 Thrustor	28
	17	Mark III, Mod 4 Thrustor Design	29
	18	Internal Wiring Schematic of the Mark III, Mod 5 Thrustor	30
	19	Sketch of Tungsten Sphere Thrustor	31
	20	Specific Impulse Variation with Electrical Input Power..	38

ILLUSTRATIONS (Cont'd)

Figure	21	Applied Voltage versus Current, Mark II, Mod 2 Thrustor	40
	22	Applied Voltage versus Current, Tungsten Sphere Thrustor	41
	23	Performance of Mark III, Mod 3 Thrustor During 50-Hour Test	44
	24	Performance of Mark III, Mod 4 Thrustor During 293-Hour Test	45
	25	Pressure Normalized Throat Mass Flux versus Plenum Chamber Enthalpy, for Hydrogen.....	49
	26	Greyrat Enthalpy Probe.....	55
	27	Front View of Probe Insertion Unit	56
	28	Rear View of Probe Insertion Unit.....	57
	29	Closeup of Microswitch for Gilman Slide Drive Assembly.....	58
	30	Resistojet Impact Pressure Profile.....	59
	31	Mark II, Mod 2 Thrustor with Pressure Ports	60
	32	Experimental Static to Stagnation Pressure Ratios From the Pressure Tap Thrustor, $A/A^* = 3.34$	61
A-1		30-mil Thoriated Tungsten Wire, Unused	68
A-2		30-mil Thoriated Tungsten Wire, After 120 minutes at 2400°K	69
A-3		30-mil Thoriated Tungsten Wire, After 240 minutes at 2400°K	71
A-4		75 percent Tungsten-25 percent Phanium Wire.....	73
A-5		75 percent Tungsten-25 percent Rhenium Wire, After 293 hours at 2800°K	75

ILLUSTRATIONS (Cont'd)

Figure A-6	30-mil Thoriated Tungsten Wire, 45 minutes at 2400°K without Boron Nitride Contact.....	76
B-1	Failure Location of 30-mil Thoriated Tungsten Wire After 240 minutes at 2400°K	78
B-2	Distorted Portion of Tungsten Support Pin, Showing Tungsten Boride	81
B-3	Crack Forming in Tungsten Support Pin Showing Tungsten Boride	82
B-4	Wire Microstructure showing Presence of Tungsten Boride	83
B-5	Microhardness Indentations in the Tungsten and Tungsten Boride Phases	84
B-6	Molybdenum Support Segment After 293-Hours	85
D-1	Tungsten Wire Radiation versus Temperature for Different Diameters	91
D-2	Equilibrium Inner Chamber Wall Temperature for Various Wire Temperatures	93
D-3	Linear Temperature Gradients in Tungsten Wire.....	95
E-1	Frozen Overall Efficiency as a Function of Area Ratio, Hydrogen	101
E-2	Frozen Specific Impulse as a Function of Area Ratio, Hydrogen	103
E-3	Operating Envelope for Frozen Hydrogen Flow, $T_o = 2600^\circ\text{K}$	104
E-4	Overall Efficiency Increase with Area Ratio, Hydrogen	105
E-5	Frozen Specific Impulse Increase with Area Ratio, Hydrogen	106

III. REFERENCES (Concl'd)

Figure	E-6	Ratio of Exhaust Velocity to Throat Acoustic Speed as a Function of Area Ratio	107
	E-7	Throat Reynolds Number Variation with Stagnation Pressure, Hydrogen	110
	E-8	Nozzle Exit Cone Drag Parameter Variation with Mach Number For $\beta = 0.6$	115
	E-9	Effect of Boundary Layer Displacement Thickness on Area Ratio	117
	E-10	Thrust Variation with Exit Cone Half Angle at Constant Geometric Area Ratio, Hydrogen. Venting Pressure = 1 mm Hg.....	118
	E-11	Thrust Variation with Exit Cone Half Angle at Constant Geometric Area Ratio, Hydrogen. Venting Pressure = 0	119

TABLES

Table I	Performance of the Mark II, Mod 2 Thrustor	33
II	Performance of the Mark II, Mod 3 Thrustor	34
III	Performance of the Mark III, Mod 1 Thrustor	35
IV	Performance of the Mark III, Mod 4 Thrustor	36
V	Performance of the Experimental Tungsten Sphere Thrustor	37
VI	Performance of the Mark III, Mod 3 Thrustor, 50-Hour Test	43
VII	Performance of the Mark III, Mod 4 Thrustor, 293-Hour Test	43
VIII	Data From the Experimental Mark II, Mod 2 Thrustor with Pressure Taps	54

I. INTRODUCTION

The objective of Phase I of the program in Electrothermal Engine Research and Development has been the development of a 2- to 3-kw thruster system to produce a specific impulse in the range 800 to 950 seconds at an efficiency of 60 to 70 percent. The desired overall efficiency is sufficiently high that the frozen flow efficiency must itself be nearly unity. This, coupled with the given range of specific impulse, forces the choice of hydrogen as the propellant.¹ To achieve this performance range with hydrogen a resistojet configuration was selected.

Several configurations have been proposed to heat a gaseous propellant by resistojet action, including flow through high temperature pipes,² flow through a porous high temperature solid³ (or, similarly, flow through the interstices of an assemblage of high temperature solid objects), and flow over heated wires.⁴ For the purposes of this program the heated wire was selected as the primary configuration, with a backup configuration consisting of an array of tightly packed solid spheres. The advantages of the wire heater are that (1) the voltage-current characteristic of the heater can be predicted and varied easily by changing wire length and diameter, (2) a heater resistance of the order of one ohm is easily achieved, small enough to be compatible at the 3-kw power level with the upper limit voltage capabilities expected of solar panels and at the same time large enough to reduce lead losses to tolerable values, and (3) the heater elements are inexpensive and easily fabricated. The major disadvantage was thought to be the danger of heater burnout through wire evaporation, but this proved not to be a serious problem at specific impulse values up to 840 seconds.

The major difficulties encountered during the program were in the area of high temperature materials behavior and compatibility. For the most part physical design of the heat exchanger was sufficient to alleviate the materials problems, and, at the conclusion of this Phase I a 3-kw resistojet thruster had been operated for a 295-hour time period at a specific impulse of 840 seconds and an efficiency of 67 percent.

The participants in this research and their areas of particular contribution include Mr. K. Clark, Fluid Mechanics and Aerodynamics, Mr. J. T. Smith, Materials Investigations; Messrs. J. Malenda and G. Enos, Thruster System Design and Development; Messrs. J. Sexton and P. Talbot, Thruster Operation and Performance Measurement. Mr. J. F. Connors was Project Engineer, and Dr. S. Bennett was Project Director. Much valuable aid was received from Dr. R. R. John who was an active consultant to the program.

This program was managed for the NASA Lewis Research Center by Messrs. H. Hunczak and H. Ferguson of the Electric Propulsion Office, whose advice and assistance are gratefully acknowledged.

II. THRUSTOR DESIGN

During the course of this program a number of design modifications of the basic wire coil heat exchanger were employed. In addition, preliminary development of a backup heat exchanger configuration involving an assembly of solid spheres was pursued. In the next three paragraphs of this section general discussions are given of Materials Selection (paragraph A), Wire Coil Heat Exchanger Design Principles (paragraph B), and Nozzle Design (paragraph C). Paragraph D lists and describes each of the wire coil thrustor models developed during the course of the program. Finally, paragraph E summarizes the effort on the backup sphere heat exchanger.

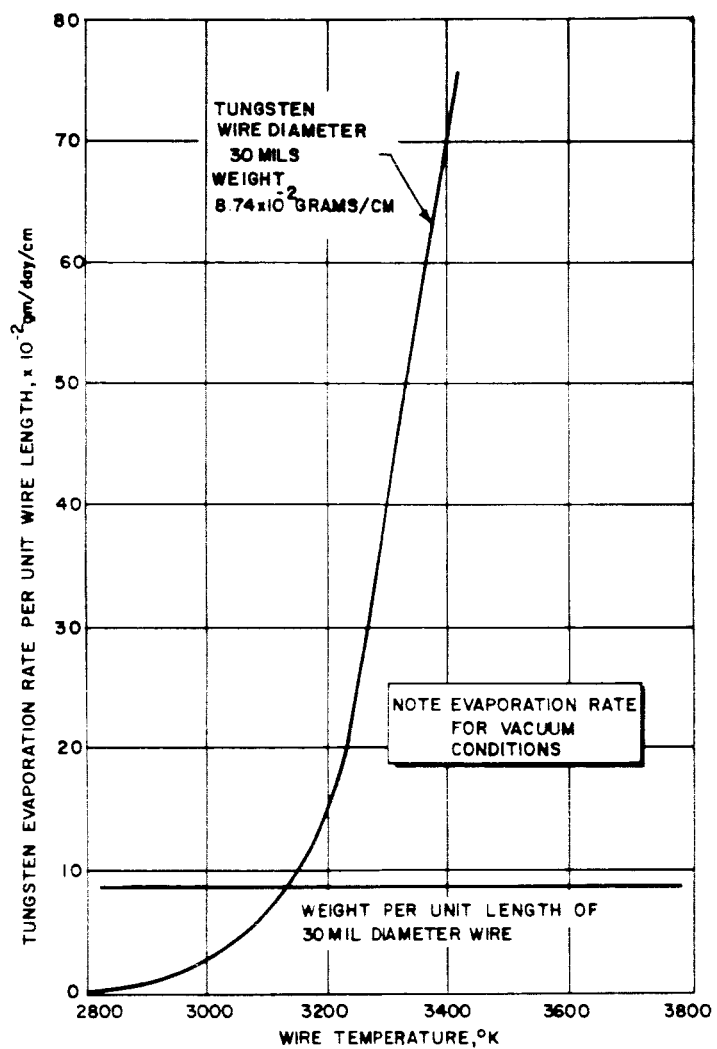
A. MATERIALS SELECTION

1. Heater Material

The desired specific impulse range can be translated, for hydrogen, into a stagnation temperature range of approximately 2500° to 3000°K (see reference 1). Anticipating that the heater element temperatures will be required to exceed the propellant stagnation temperatures by as much as several hundred degrees, the heater elements must be operated at temperatures in excess of 2500°K. This operating temperature range forces the choice of tungsten or a tungsten alloy as the heater material.

During the course of the experimental program, heater wires of pure tungsten and of three alloys of tungsten were tested. Pure tungsten was rejected shortly after the program was initiated because of its poor ductility which made coil fabrication difficult. Subsequent experience with the alloys 98 percent tungsten-2 percent thoria, 97 percent tungsten-3 percent rhenium, and 75 percent tungsten-25 percent rhenium is detailed in appendix A. The general conclusion reached after considerable operating experience was obtained with each alloy is that the 75 percent tungsten-25 percent rhenium alloy is preferable for use in the resistojet configurations employed on this program. This alloy shows superior ductility initially and at all stages of use. No heater failures attributable to coil embrittlement occurred with this alloy.

The basic problem remaining with regard to the heater element involves the evaporation rate at elevated temperatures. The situation with regard to pure tungsten in vacuum is well known, and standard handbook values have been used to draw figure 1, which presents the evaporation rate for a 0.030-inch diameter wire in grams per day per centimeter length versus temperature in °K. The weight per unit length of this wire is also given in figure 1, and the clear inference to be drawn from the figure is that wire temperatures much above 2800°K will produce significant evaporation rates.



63-10361

Figure 1 TUNGSTEN EVAPORATION RATE PER UNIT WIRE LENGTH VERSUS WIRE TEMPERATURE

The rates indicated in figure 1 are subject to modification in practice because the wire is not pure tungsten and because the ambient conditions are a hydrogen flow rather than vacuum. It has been reported^{4a} that significantly different evaporation rates are applicable for the flow situation. It is unlikely, however, that great improvements over the situation diagrammed in figure 1 can be expected from alloying or from the flow condition, in particular since the evaporation rate rises so steeply with temperature.

Therefore, the required heater temperature is bounded from below by the propellant stagnation temperature requirement, and from above by the evaporation rate of tungsten. The operating range is then 2600° to 2800°K.

2. Insulator

At the outset of the program, uncertainties existed with regard to the suitability of commercially available boron nitride for use in the electrothermal thruster. It had been reported in the literature⁵ that although pure boron nitride retains its strength undiminished up to the sublimation point of 3000°K, the addition of small quantities of boric oxide as a bonding agent during fabrication degrades this high temperature performance severely. Therefore, an effort was made to investigate the possibility of fabricating pure boron nitride without the use of boric oxide binder. This effort began with a literature survey as well as consultation with Avco RAD staff members who have extensive experience with high temperature ceramics. The conclusion of this survey was that the problem was not so severe as had been anticipated; if necessary the boron nitride can be fabricated with boric oxide binder and heat treated after fabrication to remove the binder, leaving pure boron nitride. Further, while this survey was in process, laboratory experience was being obtained with commercially available boron nitride in the early thruster designs. No significant problems associated with boric oxide were encountered. Commercially available boron nitride which has been carefully handled to avoid collection of moisture, or which has been baked out at relatively low temperatures to drive off accumulated moisture, seems to function adequately. For this reason this aspect of the program was deemphasized.

A bibliography resulting from the literature survey is presented as appendix F, for future reference.

However, a problem unrelated to the presence of boric oxide was encountered, and proved to be the most significant material problem throughout the program. In contact with tungsten or molybdenum at high temperatures (and probably other metals as well, although experience was obtained only with the two metals named above), boron nitride serves as a source of boron atoms which diffuse into the metallic structure and form borides. These borides are generally characterized by lower melting temperatures than the base metal; further, the metallic boride and the base metal can form

a eutectic with a radically depressed melting point. (For tungsten and tungsten boride, the eutectic melting point is approximately 2300°K, well below the required heater operating temperatures.) This problem is discussed in detail in appendix B. The conclusions of the investigation summarized there, are that the thruster design should not permit the contact (or close proximity) of boron nitride to the heater elements.

Finally, in the longest engine test (293 hour duration) the sublimation of boron nitride posed an additional problem. Although no extensive investigation was undertaken, it appears that the thruster design must also eliminate the location of boron nitride in high temperature regions of the thruster. For temperatures up to the order of 1500°K, boron nitride is a useful insulating material. At higher temperatures it forms borides in contact with tungsten or molybdenum which are injurious, and it sublimates over long periods of time.

3. Other Materials

No difficulties were encountered in terms of engine life or performance in other materials areas. The main thruster body was made of molybdenum and the fittings and regenerative tubing of stainless steel, while seals were accomplished with stainless steel C-rings. These materials were selected for their high temperature properties, machinability, and availability.

B. WIRE COIL HEAT EXCHANGER DESIGN

Two wire coil heat exchanger configurations were tested; the first consisted of a single coil wrapped around a supporting mandrel and aligned parallel to the flow direction, while the second consisted of five series-connected coils mounted normal to the flow direction. With regard to basic requirements on the coil size the two configurations are similar, and the discussion which follows can be considered to apply to either.

1. Wire Size

The requirement for compatibility of this wire coil heat exchanger with a solar cell power supply, which is expected to supply a maximum output voltage of 56 volts, suggests a wire resistance, at operating temperatures, of approximately 1 ohm for power levels of 2 to 3 kw. A higher resistance requires a higher input voltage to achieve the desired power level and a much lower resistance requires a large current flow to achieve the desired power level. In the first case compatibility with solar cells is jeopardized, and in the second case lead losses may become severe.

A nominal wire diameter may be determined by considering wire radiation. The effects of wire cooling by convection, and heating by reabsorption of radiation can then be evaluated empirically. Figure 2 is a plot of wire

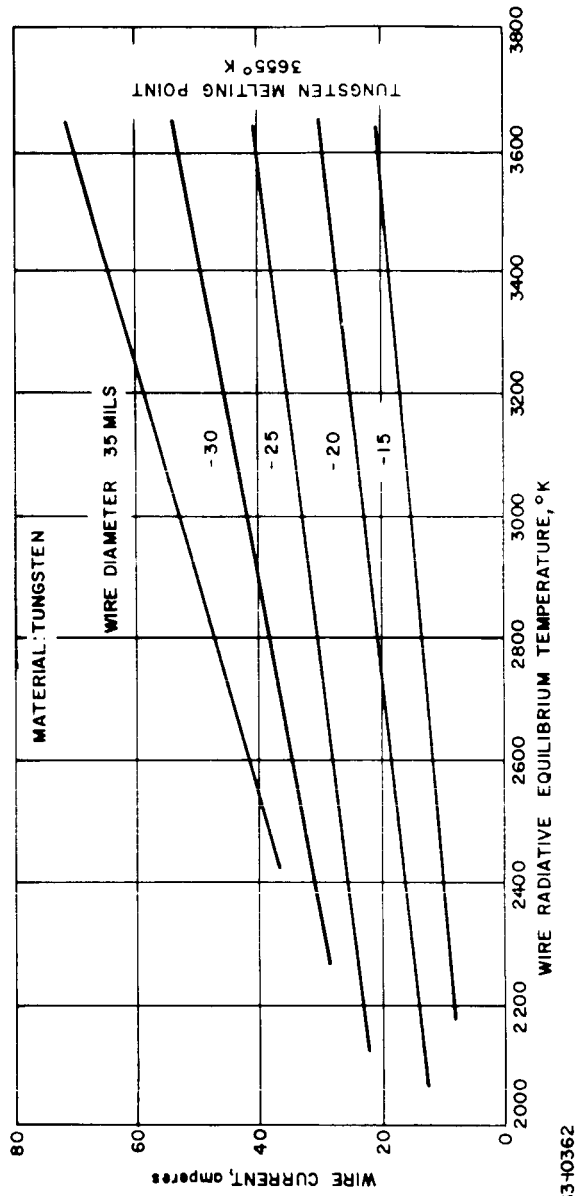


Figure 2 WIRE CURRENT VERSUS WIRE RADIATIVE EQUILIBRIUM TEMPERATURE

current, in amperes, versus the wire radiative equilibrium temperature. The assumptions of figure 2 are that the wire is pure tungsten and that there is no radial temperature gradient in the wire. The lines of figure 2 are drawn for selected wire diameters. Each line represents the locus of points for which

$$I^2 R = \epsilon \sigma A T^4 \quad (1)$$

where I is the wire current in amperes, R the resistance per unit length in ohms/cm, ϵ is the emissivity, σ the Stefan-Boltzman constant (5.67×10^{-12} in watt/cm² - °K⁴), A the surface area of unit length of the wire, and T the absolute wire temperature in °K.

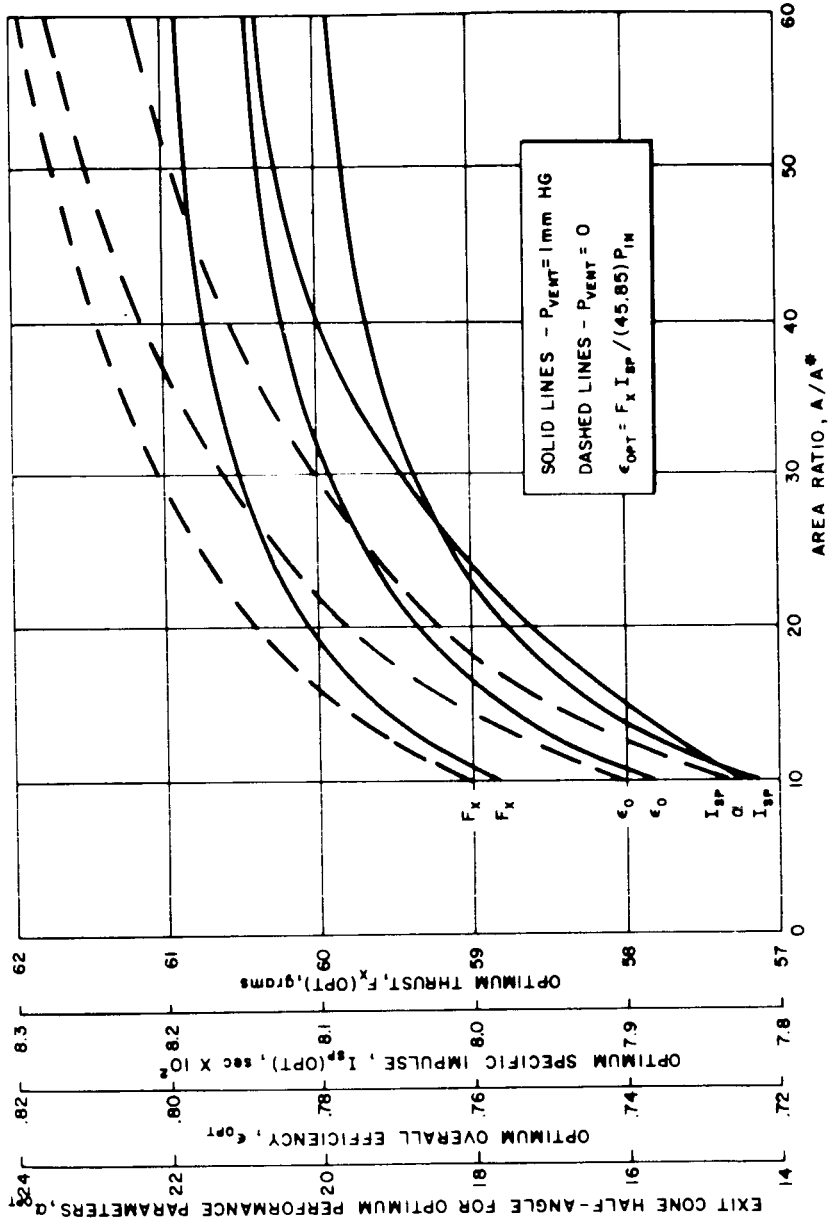
The meaning of figure 2 is that at any point on a line the wire can radiate away the input energy if the wire diameter is appropriate for the line, and that the wire surface temperature in this case is given by the abscissa of the point. Actually, significant heat transfer occurs by convection to the flow rather than the indication of figure 2. Hence, if a wire surface temperature of 2800°K is desired to yield reasonable propellant specific impulse while keeping evaporation to tolerable levels and if a current of the order of 50 amperes is selected to keep compatibility with solar cells at the 2- to 3-kw level, a wire diameter of approximately 30 mils is indicated. Small departures in wire diameter from this value can be tolerated.

Since the wire diameter and resistance have now been selected, the wire length follows from the resistivity. This is a function of temperature, but at the temperature region of interest a length of approximately 45 cm is desired.

The remaining question concerns the adequacy of a tungsten wire with a diameter near 30 mils and a length of approximately 45 cm, maintained at a temperature in the vicinity of 2500 ° to 2800°K, to transfer the required heat to the flow. This question is examined in detail in appendix D, with the conclusion that as much as 3 kw of power can be transferred by such a wire.

C. NOZZLE DESIGN

An analysis of the supersonic nozzle including certain of the effects of the boundary layer is given in appendix E. Here, in figure 3, the major results of this analysis are summarized. Figure 3 displays, as a function of geometric area ratio, the thrust, specific impulse, efficiency, and optimum nozzle half angle for a conical nozzle. The calculations assume a propellant (hydrogen) stagnation temperature of 2600°K, a stagnation pressure of 2.88 atmospheres, a throat of 0.050-inch diameter, and a mass flow rate of 0.075 gm/sec. The plotted efficiency is calculated by dividing the thrust power by an input power of 3 kw, and is thus the efficiency of conversion of electric to thrust power. The overall



64-784

Figure 3 OPTIMUM PERFORMANCE VARIATION WITH GEOMETRIC AREA RATIO

efficiency can be obtained by dividing the thrust power by 3.32 kw, thus including the thermal power content of the propellant as it enters the thruster (assuming that it is at room temperature), and is therefore equal to 0.9 of the plotted efficiency.

Figure 3 includes calculated curves for a venting pressure of 1 mm Hg, as well as for venting into a perfect vacuum.

The operating conditions for the resistojet thrusters developed during this program were slightly different from those for which figure 3 was calculated; specifically, the mass flow rate in actual operation is lower than that of figure 3 (0.065 rather than 0.075 gm/sec), the stagnation pressure is lower, and the throat somewhat larger. However, the sensitivity of the calculated results to these variances is quite small. Therefore the results of figure 3, and in particular the trends are expected to describe actual engine performance.

The principal indications of the figure are that for testing at venting pressures of the order of 1 mm Hg in a significant performance gain can be expected in going from an area ratio of 10 to one of 30; however, the incremental gain associated with further increase of the area ratio is quite small. In fact, the gain in thrust is well within the experimental uncertainties of performance measurement (see appendix C). The optimum nozzle angle increases slightly with area ratio, but the variation for an area ratio variation of 10 to 60 is only from 14 to 20 degrees.

The engines developed under this program after completion of the nozzle analysis were designed with a geometric area ratio of 30, and an expansion half angle of 15 degrees.

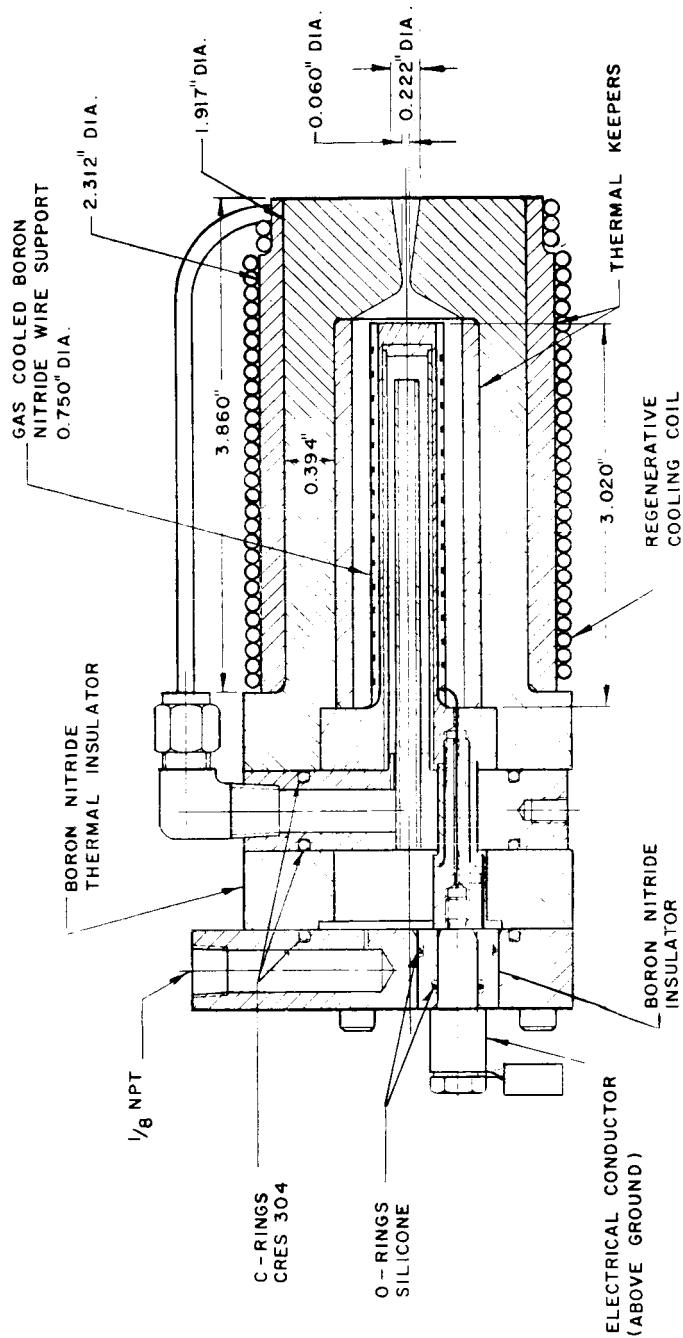
D. ENGINE DESIGN

Prior to the initiation of this program, a resistojet thruster based on the wire coil design of Jack and Spisz⁴ had been developed. This, the Mark I thruster, demonstrated the feasibility of operating a resistojet at the 3-kw power level at specific impulse values of 800 seconds. The thrusters developed under this program were designated with Mark and Mod numbers, starting with Mark II. Each of the complete thruster designs is described in the remainder of this paragraph D. In a number of cases the differences between configurations is minor, but separate Mod designations are made for clarity.

1. Mark II Series

a. Mod 1

The Mark II, Mod 1 thruster design is sketched in figure 4. The main engine housing is made of molybdenum, as well as the support for the boron nitride mandrel. Stainless steel is used for the gas inlet mounting



OVERALL LENGTH - 7.06"
MAX. HEIGHT - 3.250"

ALL DIMENSIONS IN INCHES

Figure 4 MARK II, MOD 1 THRUSTOR DESIGN

63-10363

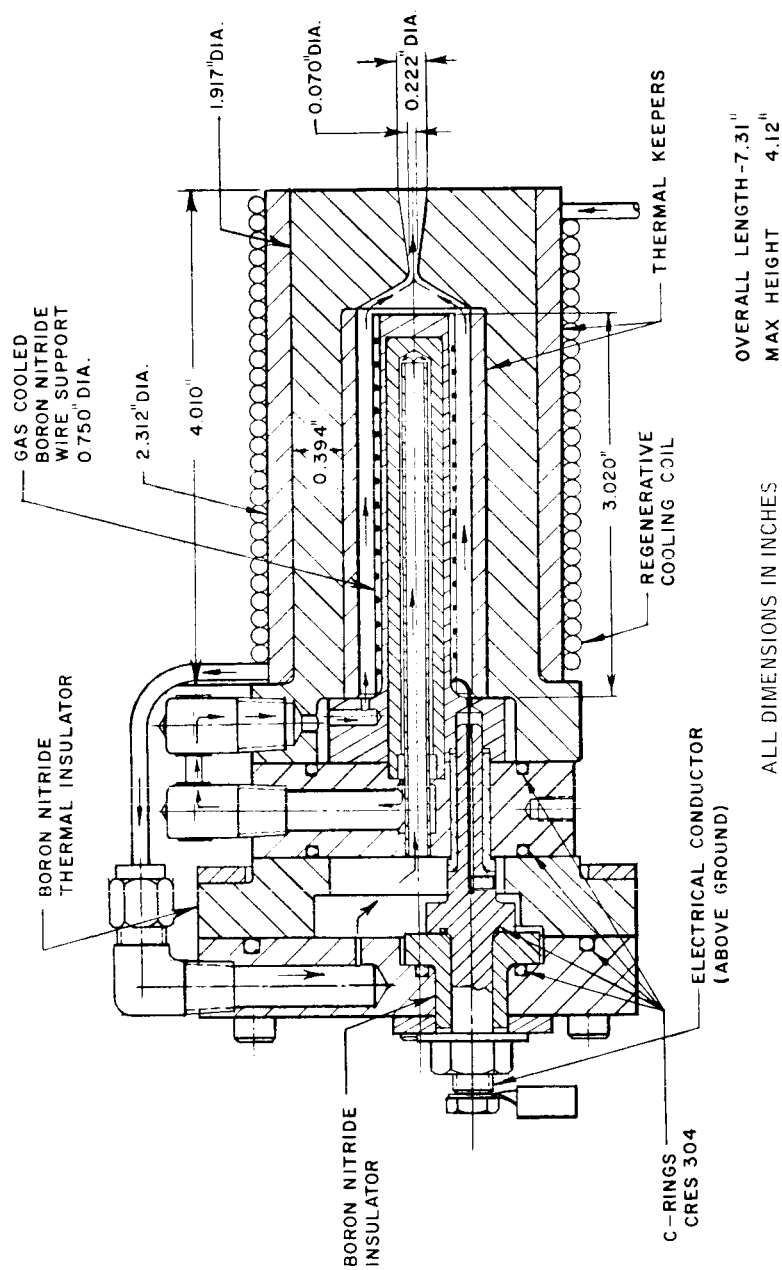
bracket and for all tubing connections, and boron nitride for thermal and electrical insulators. The heating element is 2 percent thoriated tungsten.

The propellant enters this thruster through the rear support structure, passes into the boron nitride insulator surrounding the heater wire connection to the external terminal, and then down the center of molybdenum support for the boron nitride mandrel. Here it serves to cool the wire return path, which is down the axis of the engine. After passing the length of the heater region in the downstream direction it returns upstream still within the molybdenum support as a result of a baffle. The propellant now passes through copper coils around the engine exterior, upstream to the entrance region. It is then passed into the flow region between the wire heater coil and the external housing, through the throat, and out of the nozzle.

This design suffered from a number of faults which were corrected in the next modification. These include: inadequate support for the boron nitride mandrel, poor choice of braze materials for sealing the mandrel (gold), insufficient pressure on the C-rings used to seal the rear portion of the engine, too much heating of the silicone O-rings, and improper design of the regenerative passages. (It was possible that the gas brought heat to the engine exterior rather than carrying it away because of the order in which various portions of the engine were traversed by the propellant.) For this thruster the area ratio was 11.6 and the conical expansion angle was 14 degrees.

b. Mod 2

The Mark II, Mod 2 thruster design is sketched in figure 5, and shown in the photographs of figures 6 and 7. Although basically similar to the Mark II, Mod 1 configuration, it offers the following improvements: gas enters the cooling coil at the nozzle end of the engine and then returns to the stainless steel rear structure, passes down and back up the molybdenum support for the boron nitride mandrel, through an external shunt (which is quite short) and then through the heating region and into the nozzle; iron powder is used for brazing the molybdenum support structure rather than gold to improve high temperature performance, and the braze at the downstream end of the tube is eliminated; a metal bolt circle is added to allow increased pressure on the C-rings, and 8 bolts are used for assembly rather than 4; the O-rings are replaced with C-rings. The throat diameter in this engine increased to 0.070 inch with no visible effect on performance. The expansion angle of 14 degrees was retained, and the area ratio became 10.



63-10364

Figure 5 MARK II, MOD2 THRUSTOR, DESIGN

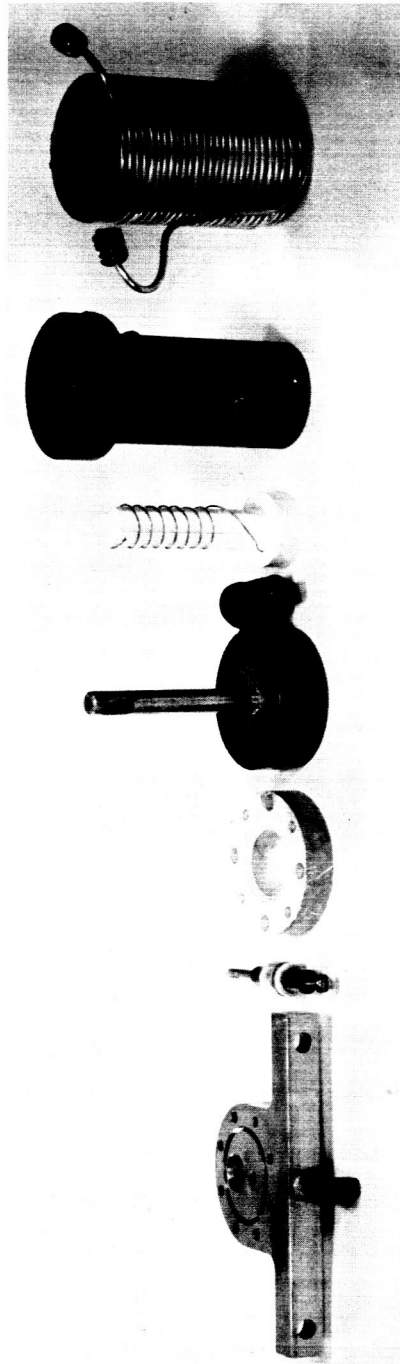


Figure 6 MARK II, MOD 2 THRUSTOR, DISASSEMBLED

10222 - B

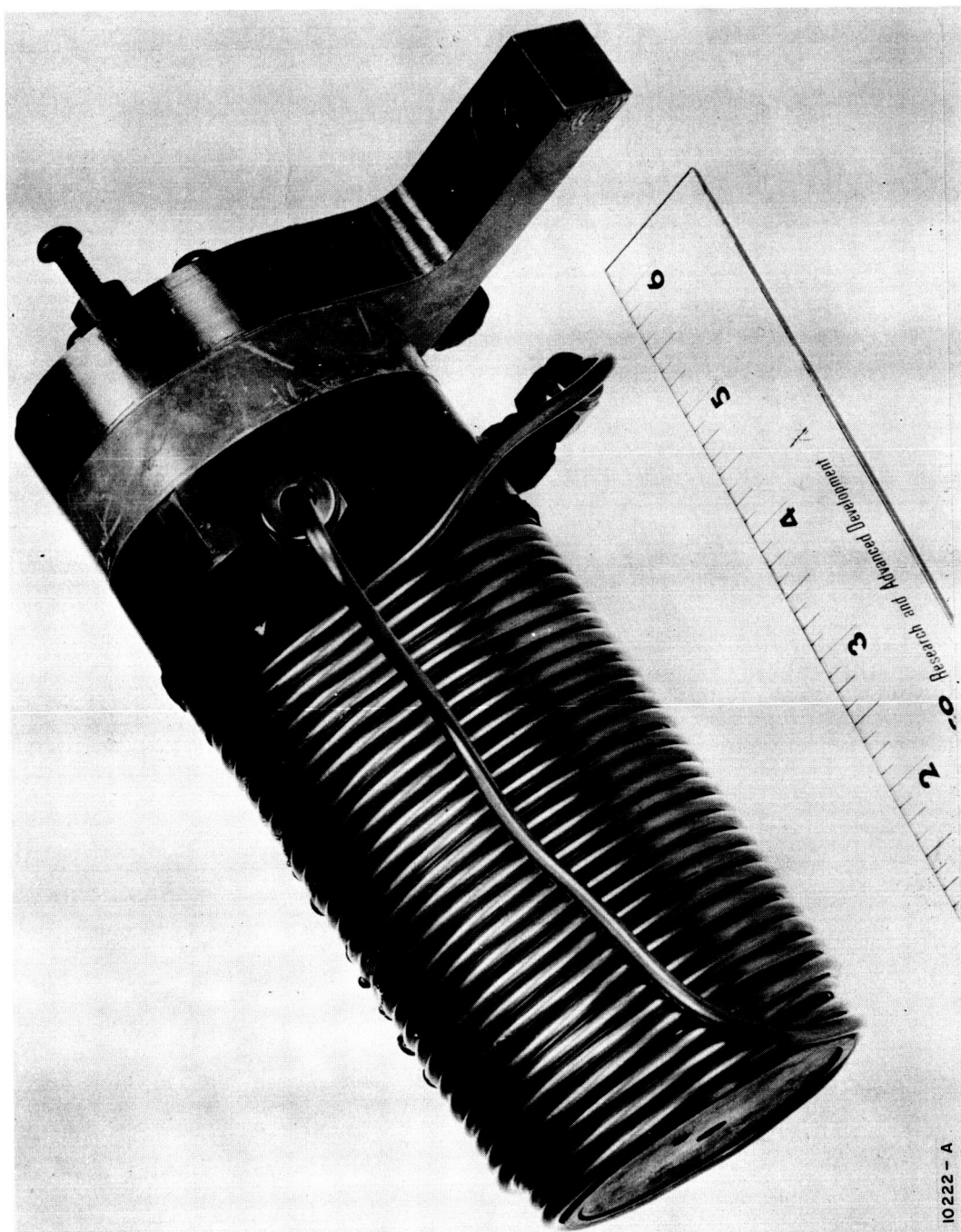
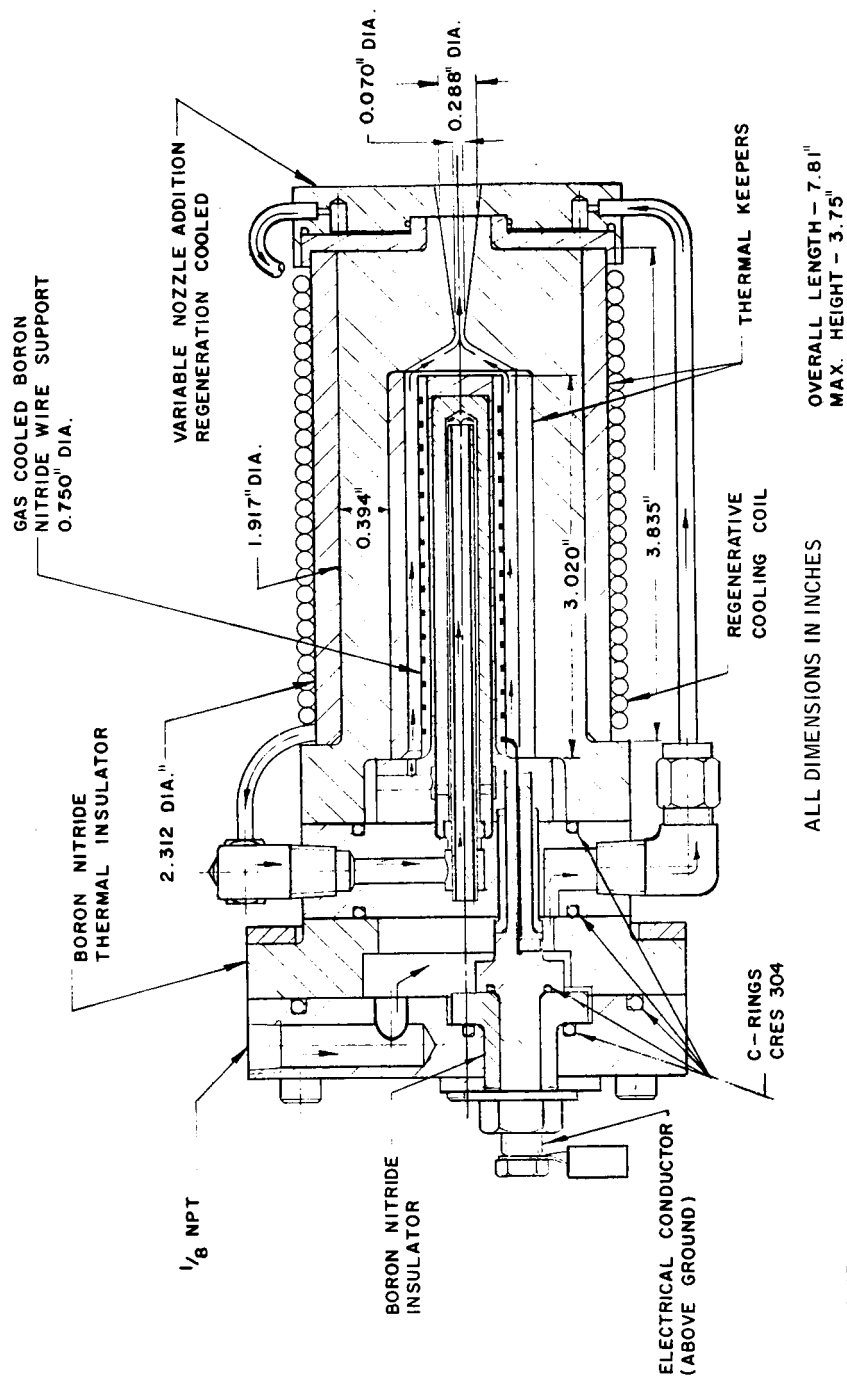


Figure 7 MARK II, MOD 2 THRUSTOR, ASSEMBLED



63-10367

Figure 8 MARK II, MOD 3 THRUSTOR DESIGN

2. Mark III Series

a. Mod 1

The Mark III, Mod 1 thruster is shown in figures 9, 10, and 11. The greatest change in this design was in the wire holder which was altered to decrease the area of contact of the tungsten wire with the wire holder. The cross sections of the Mark II, Mod 3, and the Mark III, Mod 1 wire holders are shown in figure 12. The four boron nitride rods of the Mark III, Mod 1 design are supported by three spacers on the central molybdenum shaft. This new wire holder design also eliminates the requirement for a regenerative cooling passage within the wire holder because the molybdenum central support rod acts as part of the circuit, thereby, eliminating the need to pass the wire filament back down the wire holder as in the Mark II series.

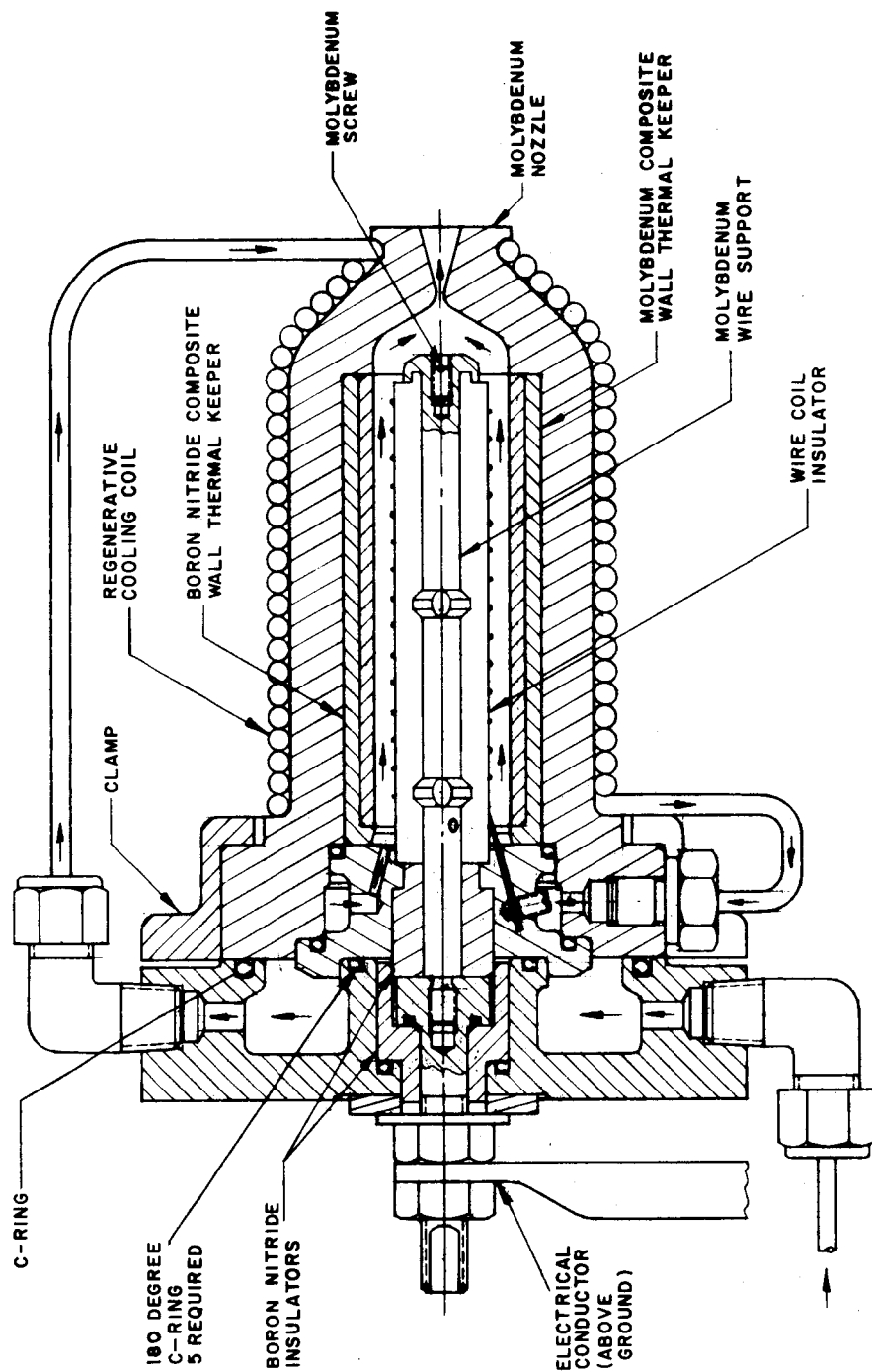
At this time some of the results of the metallographic analyses became available, and it was realized that contact between the heater wire and boron nitride must be avoided. This led to development of the Mod 2 thruster of this series.

b. Mod 2

The Mark III, Mod 2 thruster is shown in figure 13. The regenerative cooling passage for this engine follows a path similar to that utilized in the Mark III, Mod 1 thruster. Briefly, the cool hydrogen gas enters the thruster through a rear support structure cooling the rear electrical connector. The gas then passes through an external coil surrounding the nozzle and thruster body. It then reenters the engine, cools the innermost electrical connector, and flows into the thrust chamber.

The greatest change in this particular configuration was the wire coil holder. Rather than being wound around a boron nitride mandrel, the wire was supported on tungsten pins. The pins are, in turn, imbedded in strips of boron nitride which run axially along a molybdenum mandrel. The molybdenum mandrel acts as the return current path thereby eliminating the need for regenerative cooling of the mandrel.

This particular thruster configuration was prompted by the results of the metallographic analysis. Since the X-ray analysis had not been completed at this time, the tentative conclusion had been drawn that hot spots were caused in the wire by insufficient convective cooling of the wire by the passing hydrogen gas. Hence, the purpose of the pins was to raise the wire from the boron nitride mandrel thereby promoting a uniform heat transfer between the wire and the propellant. Hot spots would not develop at the contact points between the wire heater element and the pins since the metallic pins effectively reduce the electrical resistance at the contact points.



64-744

Figure 9 MARK III, MOD 1 THRUSTER DESIGN

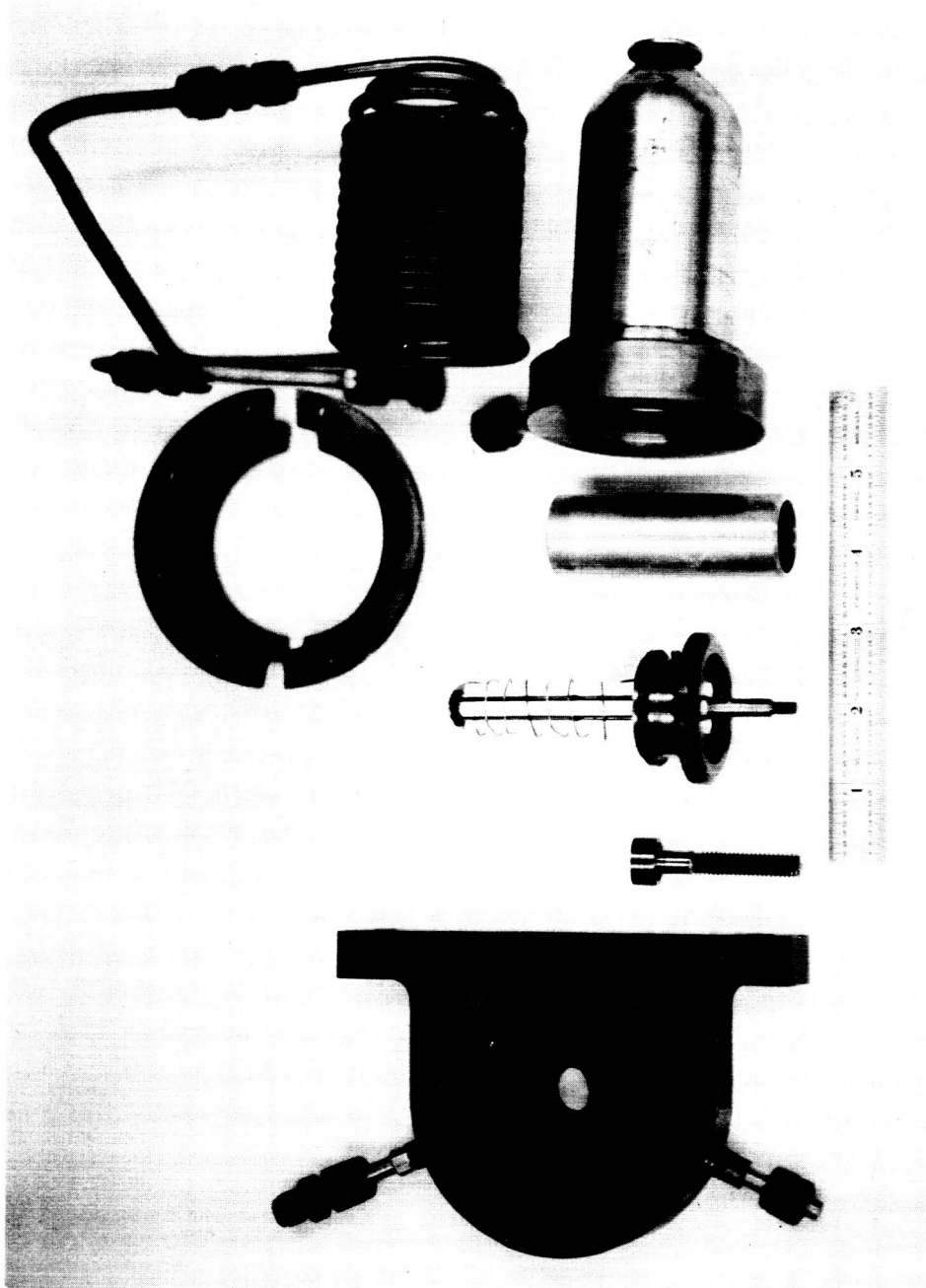


Figure 10 MARK III, MOD 1 THRUSTOR, DISASSEMBLED
64-10353

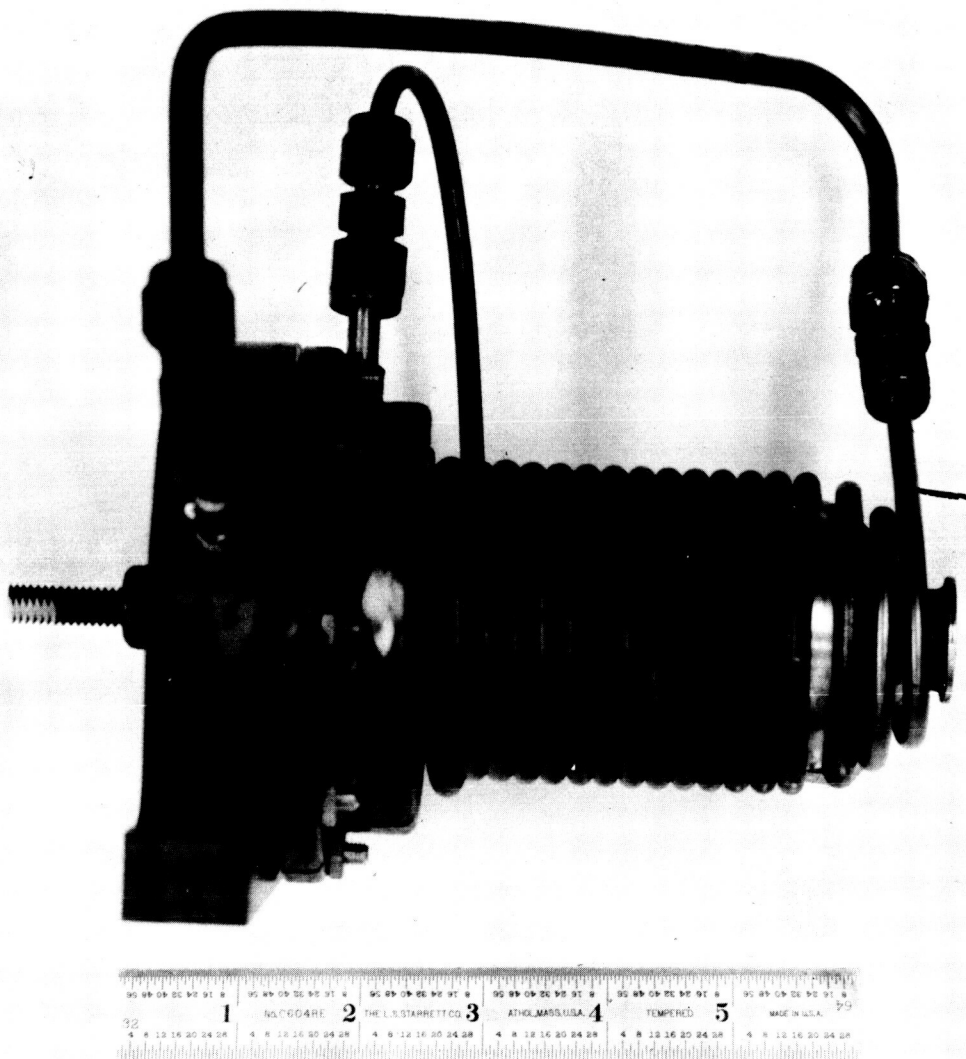
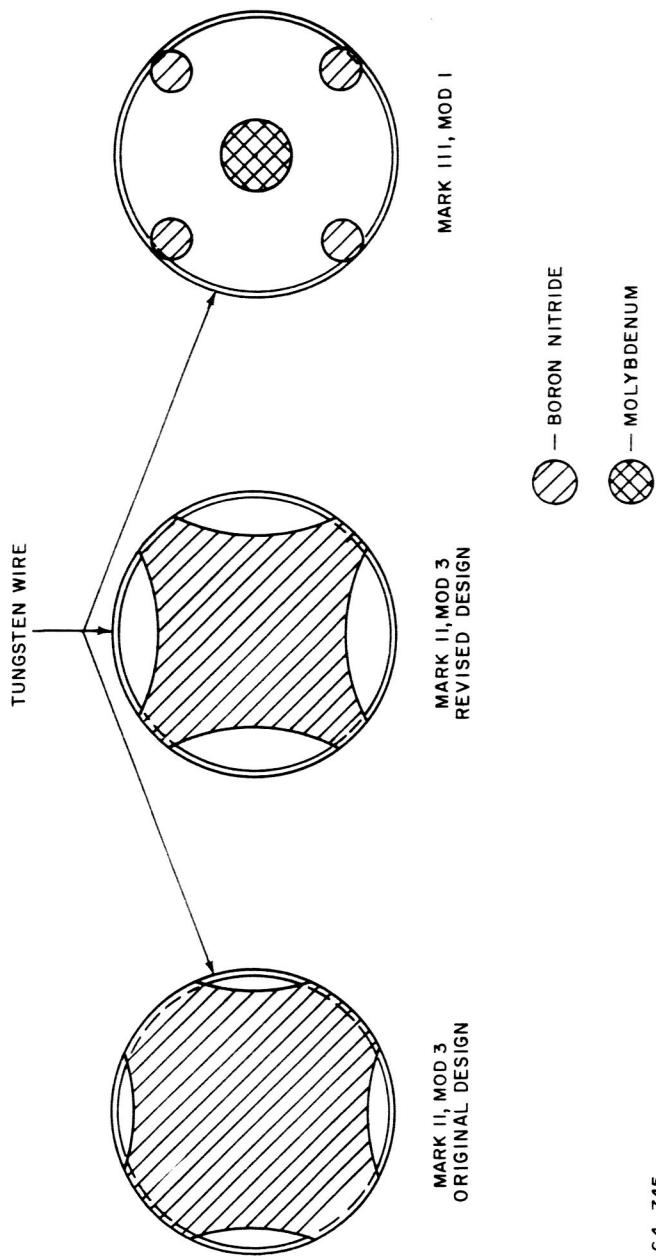


Figure 11 MARK III, MOD 1 THRUSTOR, ASSEMBLED
64-10354



64-745

Figure 12 END VIEW OF BORON NITRIDE WIRE HOLDER

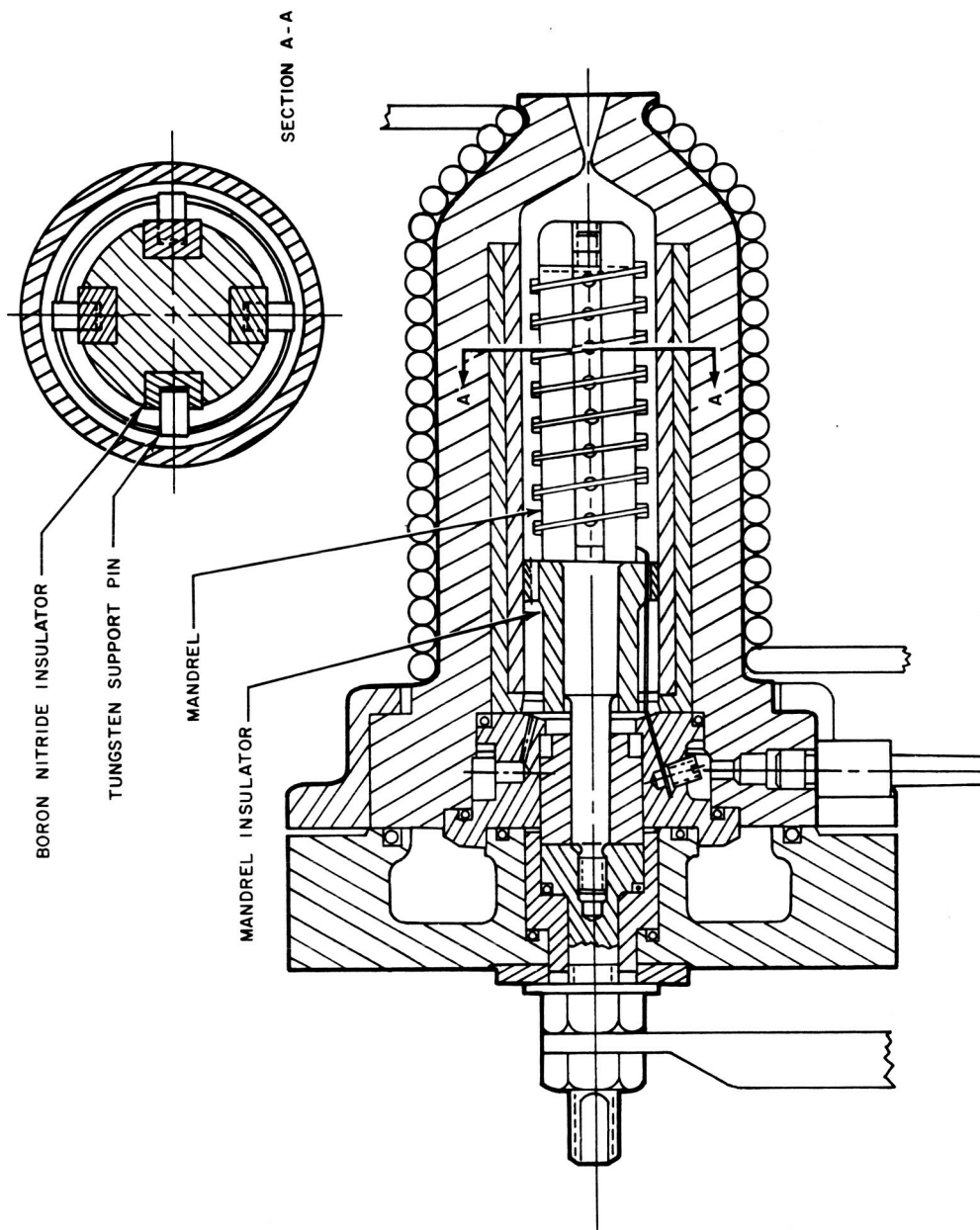


Figure 13 MARK III, MOD 2 THRUSTOR DESIGN

64-3755

The Mark III, Mod 2 thruster was satisfactory from the point of view of propulsive performance. It also appeared satisfactory from the standpoint of heater element lifetime as the wire showed no signs of localized hot spots after tests of a few hours duration. However, as the X-ray analysis of failure locations on other tungsten heater elements predicted, the tungsten pins were severely deformed and cracked at the end in contact with the boron nitride strips in the mandrel. This adverse reaction was caused by the previously discussed eutectic melting of tungsten and tungsten boride. At this point, it was concluded from the metallographic and X-ray analyses that for a resistojet thruster of the wire-coil type to be capable of long duration running times, any contact between tungsten and boron nitride at a temperature greater than 2300°K must be avoided.

c. Bench Tests

Two new configurations were then bench tested. Each of these avoided hot tungsten-boron nitride contact areas. The first of these consisted of sectioning the standard-length heater-element coil into five coils of shorter length which were then connected in series to give the desired voltage-current characteristics. These coils were connected to massive molybdenum sections which formed the inner cylindrical walls of the chamber heat transfer area. The molybdenum sections were, in turn, separated by pieces of boron nitride for electrical insulation. A secondary advantage of this arrangement was that the coils lie in a radial rather than an axial direction thereby contributing to better forced convective heat transfer. During the operation of this heat transfer core at 3 kw of power with hydrogen gas passed over the heater elements, pyrometer measurements showed that the temperature of the molybdenum pieces reached approximately 1700° to 1800°K, a temperature low enough to prevent sublimation of boron nitride. The test was terminated voluntarily after five hours with subsequent materials examination showing an extremely small amount of deterioration.

The second configuration which was bench tested was a single-coil heater element suspended from molybdenum blocks by five wire hooks fabricated from 0.015-inch diameter tungsten wire. These support wires were sufficiently long so that the temperature drop through each of them was approximately 900°K. The coil was suspended axially in a quartz tube and run at the 3-kw level with hydrogen passed over the wire for five hours. After voluntary termination of the test, postrun observation again showed negligible erosion of all elements including the boron nitride piece which supported the molybdenum blocks. However, between adjacent support wires, the heater element was observed to sag sufficiently so that it made contact in three places with adjacent coils shorting out a small segment of the wire. Although this problem could have been alleviated by the incorporation of additional support wires, the thruster assembly

procedure would then have been extremely complex. Thus, of the two configurations tested, the former appeared more feasible.

Both of the configurations tested utilized a heater element made up of four 0.015-inch diameter wires wound together. The material was a composition of 75 percent tungsten and 25 percent rhenium rather than the former material of 98 percent tungsten and 2 percent thorium oxide. The smaller diameter wires and the rhenium additive proved to be a significant improvement in retarding grain growth. Physical evidence of the smaller grain sizes was shown when after the five-hour bench tests, the rhenium-additive wires were still extremely ductile whereas thoriated-tungsten wires, run for the same length of time, were severely embrittled.

d. Mod 3

On the basis of these bench tests, a new configuration designated the Mark III, Mod 3 thruster was constructed. The thruster is shown in figures 14, 15, and 16. With the exception of the chamber-heat transfer section, the Mark III, Mod 3 thruster is identical to the Mark III, Mod 2 thruster. The chamber-heat transfer section of the Mark III, Mod 3 incorporates all the improvements shown to be advantageous by the bench tests:

- 1) The single-coil heater element has been replaced by five self-supporting coils electrically connected in series so as to yield a characteristic resistance of approximately 1 ohm.
- 2) All coil axes are normal to the propellant flow direction, and adjacent coils are also normal to each other thereby improving the convective-heat transfer characteristics.
- 3) The ends of the heater coils are connected to molybdenum segments which form the inner walls of the cylindrical chamber; these molybdenum segments eliminate contact points between tungsten and boron nitride.
- 4) Each heater coil is composed of four 0.015-inch diameter 75 percent tungsten-25 percent rhenium wires.

e. Mod 4

The Mark III Mod 4 configuration sketched in figure 17 comprises several minor improvements on the Mark III Mod 3 configuration. These improvements were (1) molybdenum spoilers were added in the heat transfer section to increase the surface area and to deflect the flow over the wire coils, (2) a molybdenum fillet was inserted between

the end of the heat transfer section and the throat to improve the aerodynamics, and (3) a second regenerative coil was added outside of the first coil to reduce heat loss from the engine surface.

f. Mod 5

The Mark III Mod 5 was designed after termination of the life test of the Mod 4 after slightly more than 12 days (293 hours). The apparent cause of termination was sublimation of the boron nitride insulators between molybdenum segments in the heat exchanger section. It was planned then to remove all boron nitride from high temperature locations. The Mod 5 is intended to accomplish this; the heater design is indicated in figure 18. This engine has undergone preliminary tests, but has not yet been lifetested.

E. TUNGSTEN SPHERE HEAT EXCHANGER

As a backup to the wire coil heat exchanger, in the event that wire evaporation proved insurmountable with regard to lifetime, an entirely different thruster configuration was pursued. When it became clear that wire evaporation would not prove a serious limit to lifetime of the wire coil heat exchanger this effort was deemphasized. However, some performance data were obtained.

The heat exchanger (see figure 19) consists of an array of tungsten spheres which are packed in a tube in layers. The tube is closed at each end with a carbon plug which serves to make electrical contact with the sphere array. The downstream carbon plug is also the nozzle. The spheres used were 0.18 to 0.19 inch in diameter, this being the smallest size which could conveniently be fabricated without an extensive development effort. The tube was boron nitride.

The tungsten sphere heat exchanger was operated both with three spheres to a layer and with four.

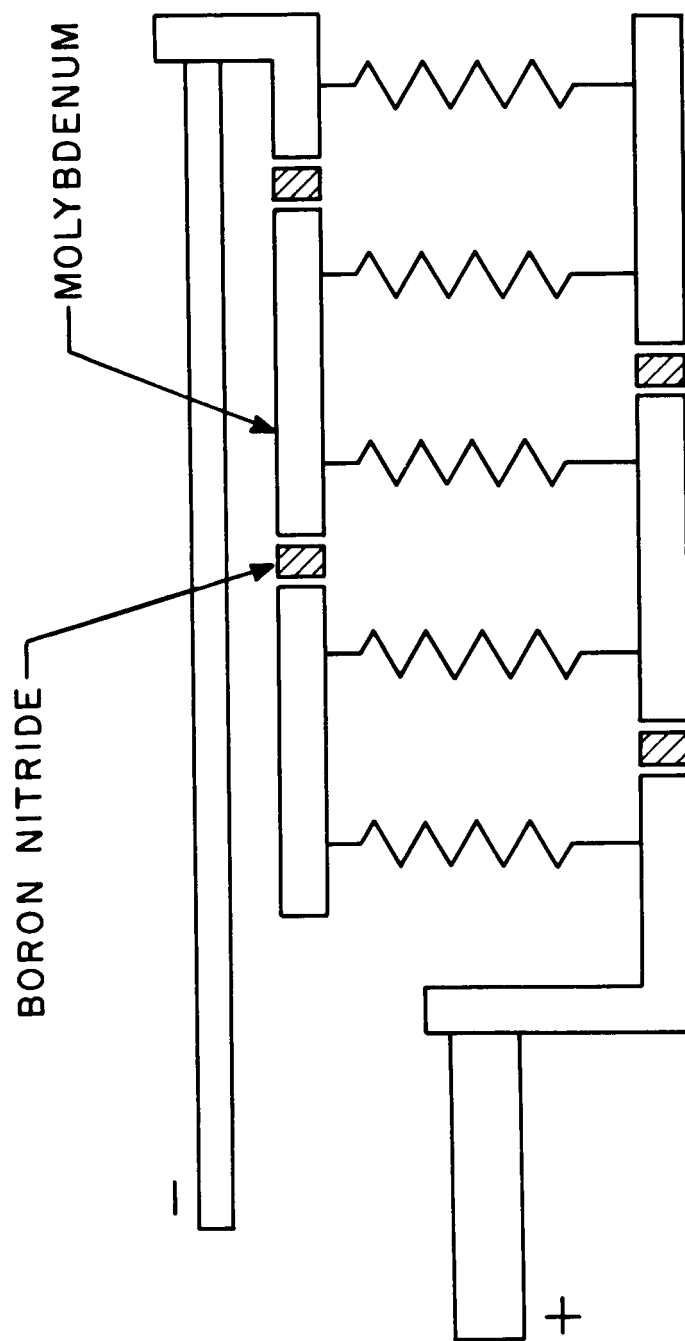


Figure 14 MARK III, MOD 3 ELECTRICAL CONNECTIONS

64-3297

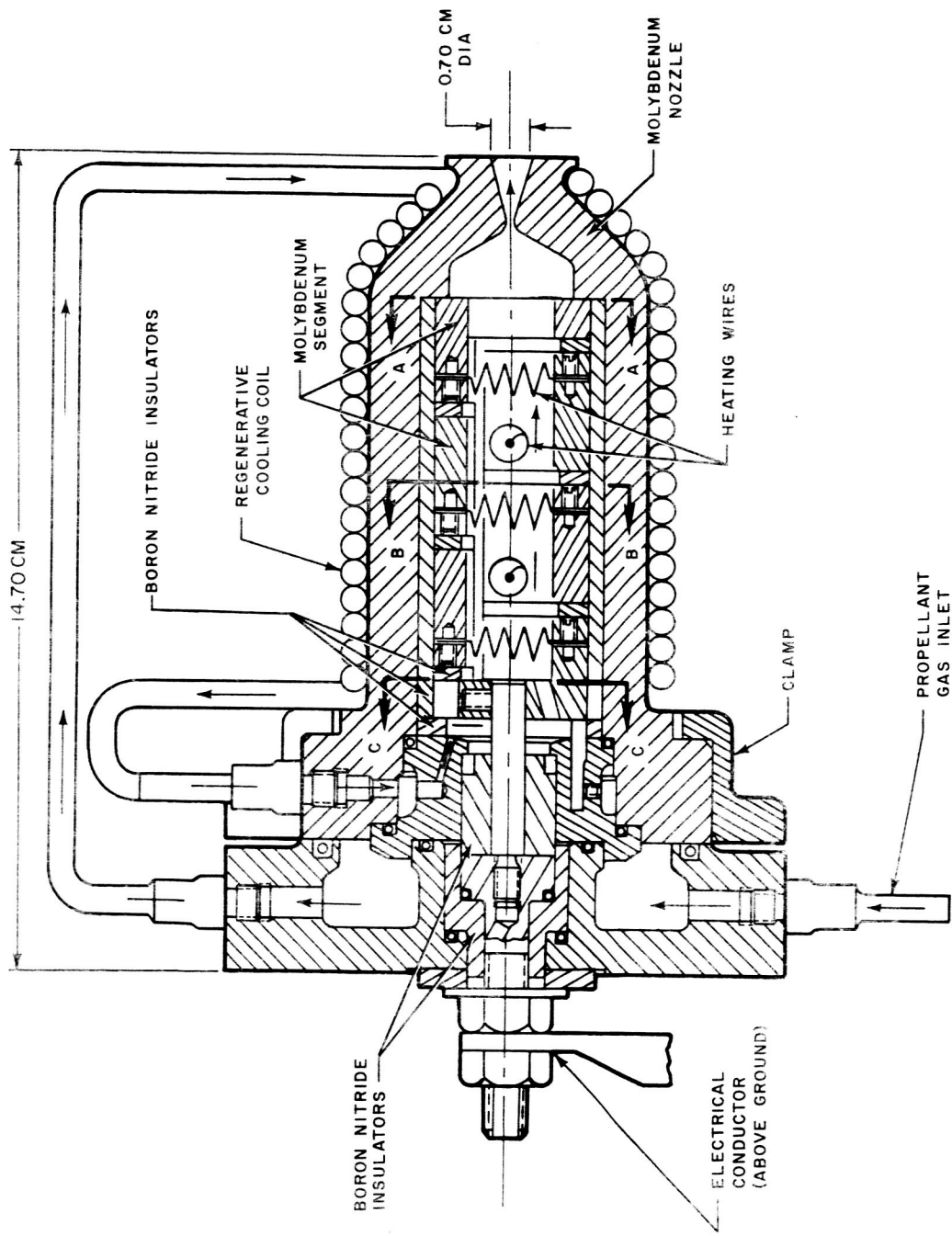
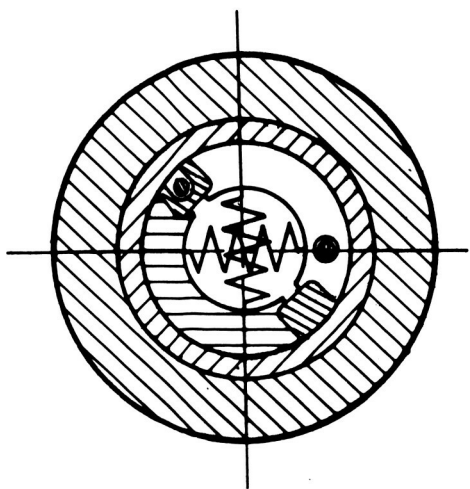
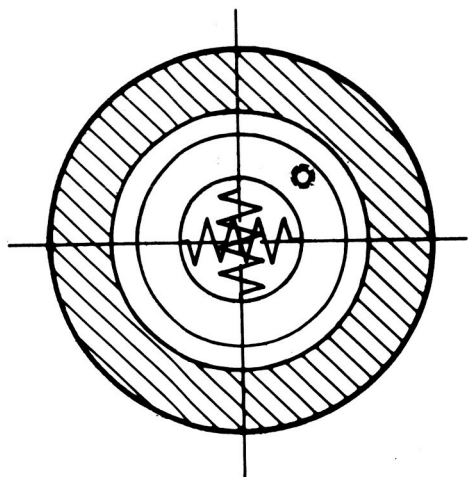


Figure 15 MARK III, MOD 3 THRUSTOR DESIGN

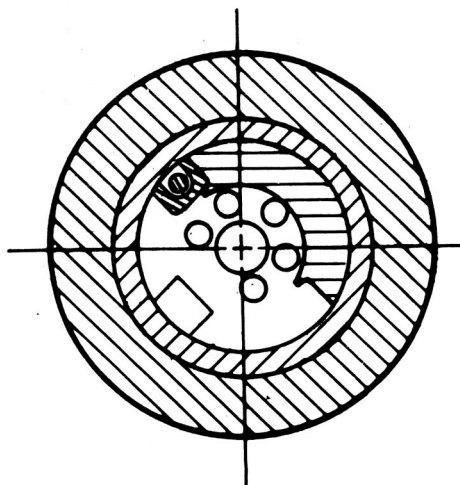
64-3763



SECTION B-B



SECTION A-A



SECTION C-C

64-3750

Figure 16 CROSS SECTION OF MARK III, MOD 3 THRUSTOR

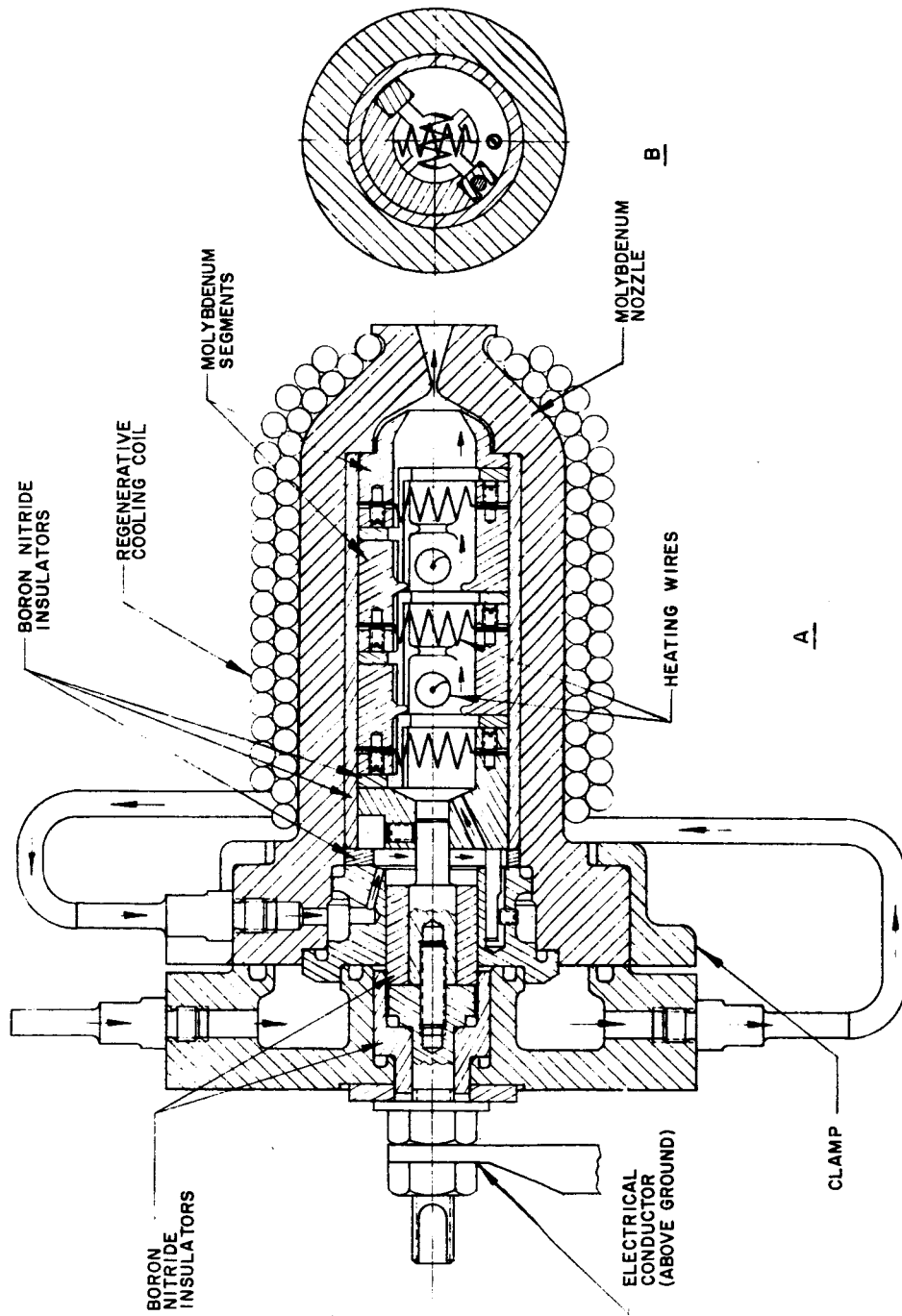
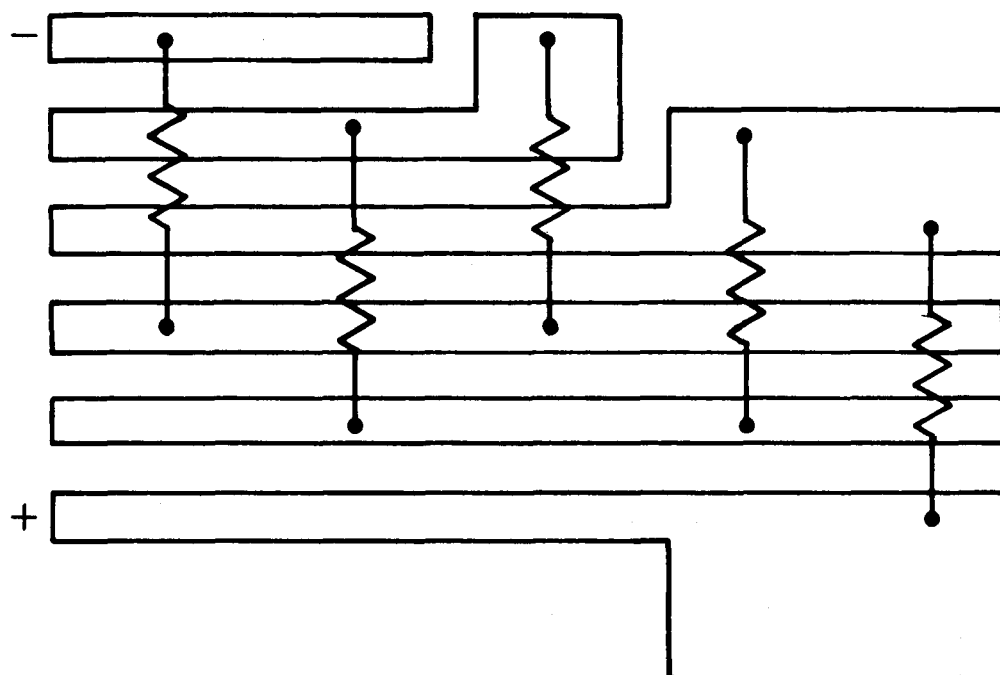


Figure 17 MARK III, MOD 4 THRUSTOR DESIGN

64-7057



64-7058

Figure 18 INTERNAL WIRING SCHEMATIC OF THE MARK III, MOD 5 THRUSTOR

III. THRUSTOR PERFORMANCE

A. PERFORMANCE MEASUREMENTS

Performance measurements obtained from the Mark II, Mods 2 and 3, and the Mark III, Mods 1 and 4, and tungsten sphere thrusters are presented in tables I through V. The method of obtaining these measurements was as follows: the thruster was mounted on the thrust stand, the test tank closed off and evacuated; after an ambient pressure below 1 mm Hg had been obtained the thrust stand was calibrated; the propellant flow was then initiated and the cold flow specific impulse measured and checked against theoretical values; without interrupting the flow of propellant power was supplied to the thruster; after steady state conditions had been reached at the initial power setting (no change with time of voltage, current or thrust) the tabulated data were recorded; power was increased to the next setting and approximately 10 minutes then elapsed to ensure steady state conditions at this power setting; the data were recorded and another power increase made; after the data had been recorded at the highest power point, power was interrupted; after the engine had cooled off the mass flow was interrupted; the thrust stand was then recalibrated, checking the initial calibration. In these tables the following quantities were directly measured: time (minutes), propellant flow rate (grams/sec), applied voltage (volts), current (amperes), thrust (grams), tank venting pressure, (mm Hg); the following quantities are derived from the measurements:

$$P_{in} = \text{voltage} \times \text{current} \times 10^{-3}, \text{ kw}$$

$$I_{sp} = \text{thrust/mass flow rate}, \text{ sec}$$

$$\text{Thrust Power} = \frac{4.8 \times 10^{-5}(\text{thrust})^2}{\text{mass flow rate}}, \text{ kw}$$

$$\text{Efficiency} \begin{matrix} \text{(with "cold")} \\ \text{(H}_2 \text{ power)} \end{matrix} = \frac{\text{thrust power}}{\text{total input power}}$$

Figure 20 shows calculated specific impulse as a function of input power for each of the thrusters. Superimposed on this figure are theoretical curves drawn for efficiencies of 50, 65, and 80 percent at a mass flow rate of 0.065 gram/second. These efficiencies were calculated as the thrust power/total input power, including the power associated with the cold incoming hydrogen gas. In general, the data points lie near the 65 percent line with a slight decrease evident at the higher powers. This slight efficiency falloff is most probably due to increased frozen flow losses and proportionally greater heat losses to the engine and then to the environment as the power is increased.

TABLE I

PERFORMANCE OF THE MARK II, MOD 2 THRUSTOR

Wire (0.030 x 15 Inch 98 Percent W, 2 Percent ThO₂)Mass Flow Rate: 0.065 gm/sec H₂, Venting Pressure: 0.4 mm Hg)

Test Point	Time (minutes)	Voltage (volts)	Current (amperes)	Power (kilowatts)	Thrust (grams)	Isp (seconds)	Thrust Power (kilowatts)	Efficiency (percent)
1	0	0	0	0	15.0	230		
2	10	3.0	43.0	0.13	27.5	423		
3	20	7.5	55.0	0.41	30.0	461		
4	30	14.0	61.0	0.85	33.0	507		
5	40	19.5	62.0	1.21	35.2	542		
6	50	23.0	63.5	1.46	38.0	584	1.06	60.9
7	60	26.0	65.0	1.69	41.0	630	1.24	63.0
8	70	30.0	68.0	2.05	44.2	680	1.44	61.8
9	80	33.0	70.0	2.31	47.0	722	1.63	62.9
10	90	38.0	72.0	2.74	49.2	758	1.79	59.2
11	100	40.0	74.3	2.98	51.0	784	1.92	58.9
12	110	42.0	75.0	31.5	53.0	815	2.07	60.4

TABLE II

PERFORMANCE OF THE MARK II, MOD 3 THRUSTOR

Wire (0.030 x 15 Inch 98 Percent W, 2 Percent ThO₂)

Nozzle: 0.050 Inch Throat, 30 Degrees Included Angle, 30 to 1 Area Ratio

Mass Flow Rate: 0.065 gm/sec H₂, Venting Pressure \approx 1 mm Hg

Test Point	Time (minutes)	Voltage (volts)	Current (amperes)	Power (kilowatts)	Thrust (grams)	I _{sp} (seconds)	Thrust Power (kilowatts)	Efficiency (percent)
1	0	0	0	0	16.0	246	-	-
2	6	5.0	45.0	0.23	29.0	446	-	-
3	12	8.0	56.0	0.45	32.0	492	-	-
4	18	14.0	62.0	0.87	35.0	533	-	-
5	24	20.0	63.0	1.26	37.0	569	1.01	65.6
6	30	24.0	64.0	1.54	40.8	628	1.23	67.5
7	36	26.0	66.0	1.72	44.0	677	1.43	71.5
8	42	30.0	68.0	2.04	47.2	726	1.64	70.7
9	48	33.0	71.0	2.34	50.0	769	1.84	70.2
10	54	38.0	73.0	2.78	53.0	815	2.07	67.6
11	60	39.0	74.0	2.89	53.0	815	2.07	65.3

TABLE III

PERFORMANCE OF THE MARK III, MOD 1 THRUSTOR

Wire (0.30 x 14 Inch 98 Percent W, 2 Percent ThO₂)Mass Flow Rate: 0.064 gm/sec H₂, Venting Pressure 1 mm Hg

Test Point	Time (minutes)	Voltage (volts)	Current (amperes)	Power (kilowatts)	Thrust (grams)	I _{sp} (seconds)	Thrust Power (kilowatts)	Efficiency (percent)
1	0	0	0	0	14.0	219	--	--
2	10	10.0	56.0	0.56	33.0	516	--	--
3	20	21.0	58.0	1.22	35.0	547	0.92	61.4
4	30	30.0	62.0	1.86	43.0	672	1.39	65.0
5	40	36.0	64.0	2.30	47.0	734	1.66	64.3
6	50	40.0	65.0	2.60	50.0	781	1.88	65.3
7	60	45.0	67.0	3.01	52.0	812	2.03	61.7
8	90	45.0	67.0	3.01	52.0	812	2.03	61.7
9	120	45.0	67.0	3.01	52.0	812	2.03	61.7
10	150	46.0	66.0	3.04	52.0	812	2.03	61.2

TABLE IV

PERFORMANCE OF THE MARK III, MOD 4 THRUSTOR

Wire (0.030 x 19 inch 75 percent W, 25 percent Re)
 Nozzle: 0.056 inch throat, 30 degrees included angle, 30/1 area ratio
 Mass Flow Rate: 0.065 gm/sec H₂, Venting Pressure: 0.6 mm Hg

Test Point	Time (Minutes)	Voltage (volts)	Current (amps)	Power (kw)	Thrust (grams)	Isp (seconds)	Thrust Power (kw)	Eff: with "cold" H ₂ power (percent)	Eff: no "cold" H ₂ power (percent)
1	0	0	0	0	15.3	236	---	---	---
2	4	47.0	48.0	2.26	38.0	585	---	---	---
3	12	47.3	47.5	2.25	41.0	630	---	---	---
4	21	47.0	47.0	2.21	44.0	677	---	---	---
5	35	50	49.5	2.48	46.0	708	---	---	---
6	45	49.5	50.0	2.47	48.0	738	1.70	61.8	69.0
7	60	50.0	50.5	2.52	49.0	753	1.78	64.0	70.0
8	71	52.0	54.0	2.81	52.0	799	1.99	64.5	71.0
9	86	54.0	56.0	3.02	54.0	830	2.15	65.1	71.1

TABLE V

PERFORMANCE OF THE EXPERIMENTAL TUNGSTEN SPHERE THRUSTOR

Length of Tungsten Sphere Array: 5.5 Inches
 Throat Diameter: 0.080 Inch
 Mass Flow Rate: 0.060 gm/sec H₂
 Venting Pressure: 0.8 mm Hg

Data Point	Voltage (volts)	Current (amperes)	Power (kilowatts)	Thrust (gm)	I _{sp} (seconds)	Thrust Power (kilowatts)	Efficiency (percent)
1	0	0	0	13.6	227		
2	7.5	33.5	0.252	26.0	413		
3	8.0	47.0	0.376	28.0	467		
4	8.0	60.0	0.480	29.0	483		
5	9.5	71.0	0.674	31.0	517		
6	12.0	78.0	0.936	34.5	575		
7	12.0	94.5	1.14	35.5	592		
8	12.5	100.0	1.25	37.0	617		
9	12.0	117.0	1.40	39.5	656		
10	11.5	155	1.78	39.0	650	1.22	59.2
11	11.5	196	2.25	43.0	715	1.48	58.5

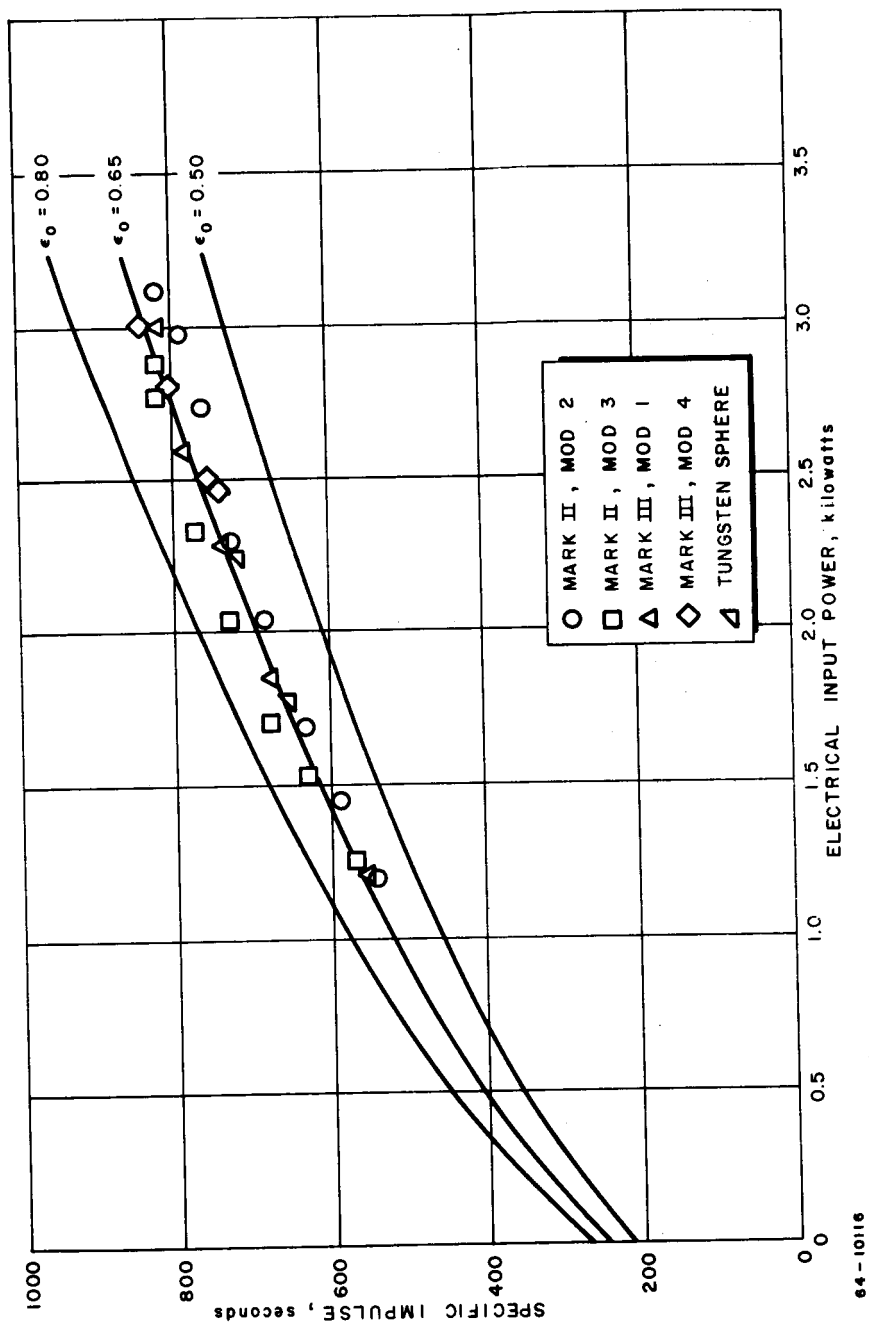


Figure 20 SPECIFIC IMPULSE VARIATION WITH ELECTRICAL INPUT POWER

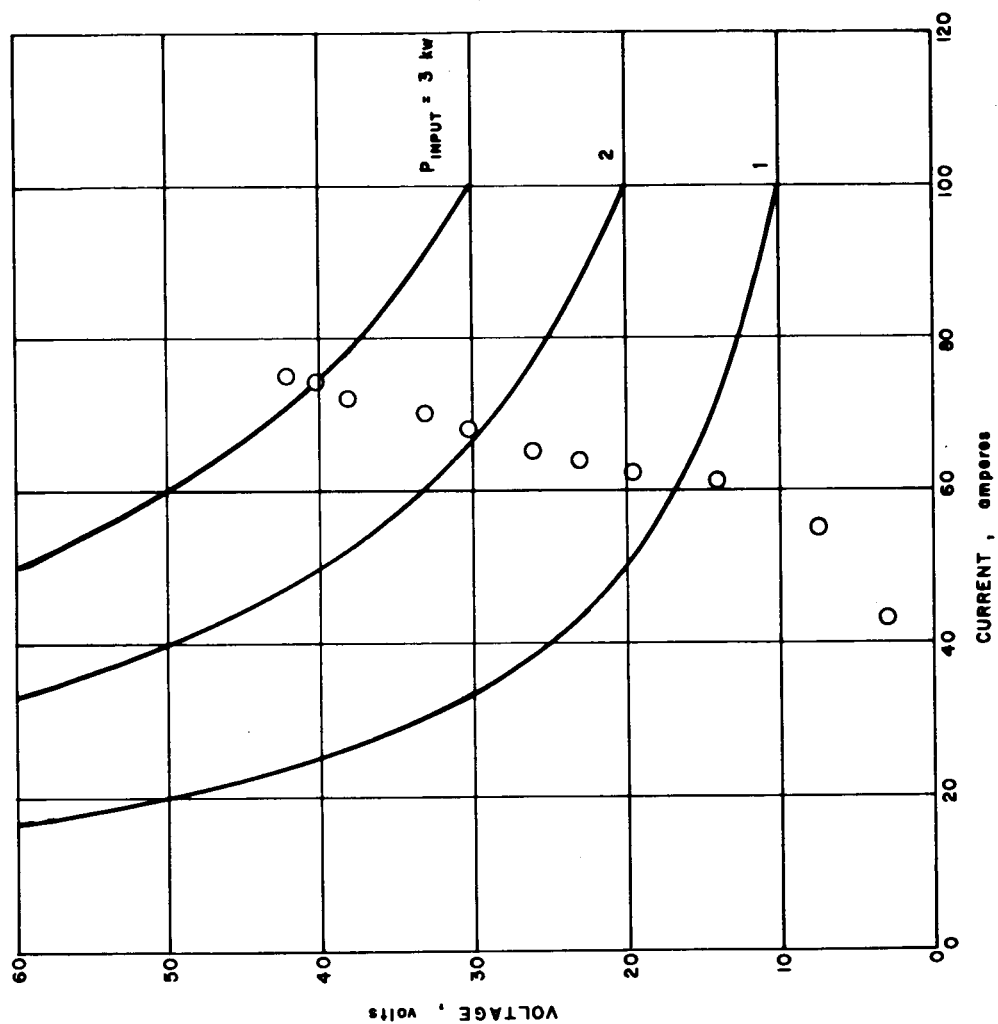
B. VOLTAGE-CURRENT CHARACTERISTICS

1. Wire Coil Heat Exchanger

Figure 21 shows typical voltage-current characteristics for a wire coil thruster, the data being from the Mark II, Mod 2 thruster. The curve shows measured applied voltage as a function of measured current. Superimposed on the figure are lines of constant input power. It can be seen from the figure that, at the higher power levels, the wire coil approximates a constant current device; that is, power increases are accomplished largely by voltage increases.

2. Tungsten Sphere Heat Exchanger

Figure 22 presents typical voltage-current characteristics of the two configurations of this type which were investigated. Again, lines of constant power have been superimposed upon the applied voltage versus measured current data. Of the two configurations investigated, one had four spheres per layer while the other had three spheres per layer. It is noted in figure 22 that the thruster with three spheres per layer actually has a lower apparent resistance (lower voltage to current ratio) than the configuration with four spheres per layer. It was anticipated that the three spheres per layer configuration would present a greater electrical resistance since the total current path would, in effect, be longer and there would be fewer contacts per layer. It is possible that the lower resistance behavior of the three spheres per layer thruster arose from the fact that, in order to eliminate propellant leakage from the system, the carbon plugs were tightened much more than for the four spheres per layer thruster. This in turn caused greater pressure at the contact joints between tungsten spheres lowering the contact resistance. The data also presents the possibility that the overall resistance is not caused by a uniform contact resistance between each pair of tungsten spheres, which would lend itself to scaling for greater overall resistance, but instead is caused by a few high resistance contacts randomly occurring within the array of spheres.



63 - 10370

Figure 21 APPLIED VOLTAGE VERSUS CURRENT, MARK II, MOD 2 THRUSTOR

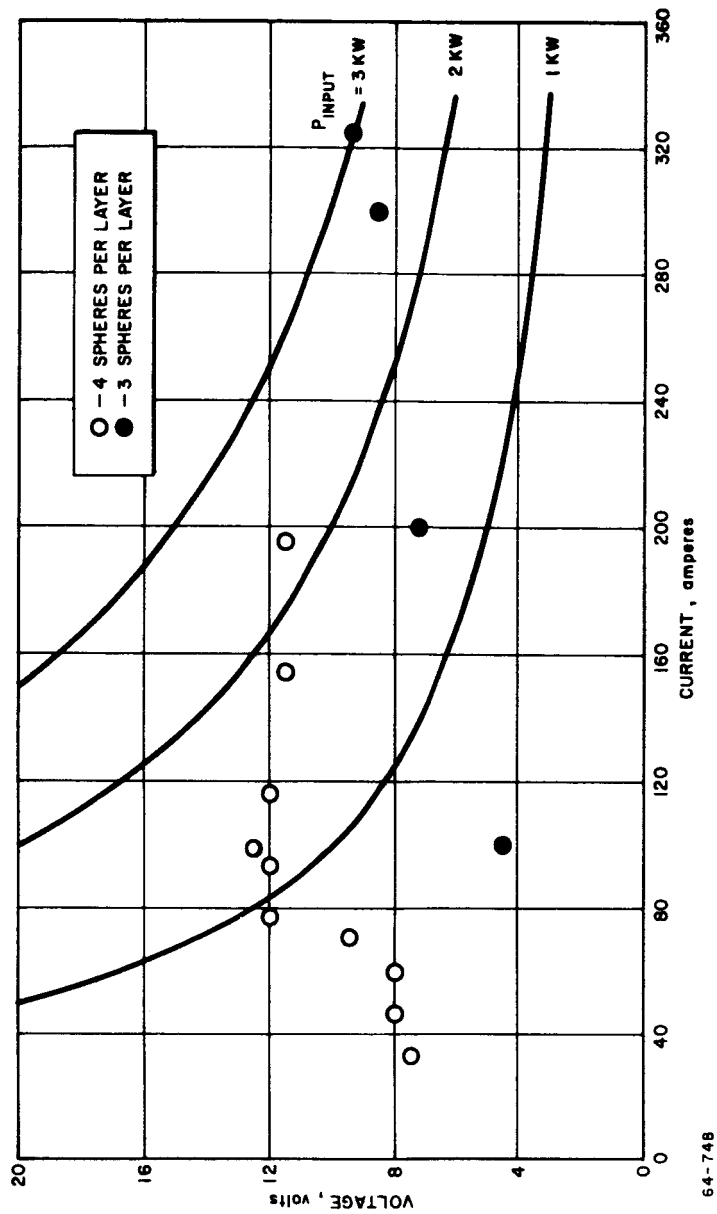


Figure 22 APPLIED VOLTAGE VERSUS CURRENT, TUNGSTEN SPHERE THRUSTOR

IV. ENDURANCE TESTS

After the major thruster design problem (eutectic melting of the heater elements) was understood and the thruster design modified to eliminate tungsten-boron nitride contact area, a 50-hour endurance test of the Mark III, Mod 3 thruster was accomplished at the 3-kw power level. Postrun materials analyses indicated that the thruster could have run for a much longer time. An endurance test of the Mark III, Mod 4 was then initiated, and 293 hours were completed. Postrun materials inspection is thought to have pointed out the cause of failure, and the Mark III, Mod 5 thruster was designed to avoid the structural weakness. The Mod 5 thruster has not yet been performance tested.

A. 50-HOUR TEST, MARK III, MOD 3

The test system employed is described in appendix C. The endurance test of the Mark III, Mod 3 thruster was initiated 3 March 1964 at 1100. The test was interrupted once after a period of 47 hours due to an interruption of power to the rectifier. This electrical fault was cleared within 1 minute and the thruster was restarted immediately without opening the test tank. The performance is summarized in table VI and in figure 23, where thrust, efficiency, and voltage are plotted against time. The voltage is seen to decrease irregularly with time, which may indicate partial electrical shorting of one or more coils with use. The thrust and efficiency, however, are constant.

Postrun materials analysis (see appendixes A and B) indicated that the heater elements had not deteriorated significantly, the boron nitride insulator segments suffered a weight loss of 1 to 2 percent, and the molybdenum wire holders showed molybdenum boride formation to a depth of 0.003 inch for the downstream segments and progressively less for upstream segments.

Comparison of measured and calculated performance for this endurance test is given in paragraph C below.

B. 293-HOUR TEST, MARK III, MOD 4

The endurance test of the Mark III, Mod 4 thruster was initiated 22 April 1964, at 1640. The test was interrupted after 293 hours of continuous running.

Performance is summarized in table VII and in figure 24, where thrust, efficiency, and voltage are plotted against time. As in the 50-hour run the voltage is seen to decrease irregularly with time while the thrust and efficiency are constant.

Postrun materials examination (see appendixes A and B) indicated that the heater elements were still in relatively good condition and the molybdenum boride formation on the wire holders was deeper than after 50 hours but still tolerable; however, the weight loss of the boron nitride insulating segments was extreme,

TABLE VI

PERFORMANCE OF THE 3-KILOWATT RESISTOJET DURING A
50-HOUR TEST

Input Power	3.0 kilowatts
Current	60 amperes
Voltage	50 volts
Mass Flow Rate	0.065 gm/sec
Thrust	52.5 grams force
Specific Impulse	810 seconds
Efficiency	62 percent
Test Duration	51 hours
Total Propellant Flow	11.9 kilograms
Total Impulse	2.1×10^4 lb-sec

TABLE VII

PERFORMANCE OF THE 3-KILOWATT RESISTOJET
DURING 293-HOUR TEST

Input Power	3.0 kilowatts
Current	64 amperes
Voltage	47 volts
Mass Flow Rate	0.065 grams/sec
Thrust	54.5 grams force
Specific Impulse	838 seconds
Efficiency	67 percent
Test Duration	293 hours
Total Propellant Flow	68.8 kilograms
Total Impulse	1.27×10^5 lb/sec

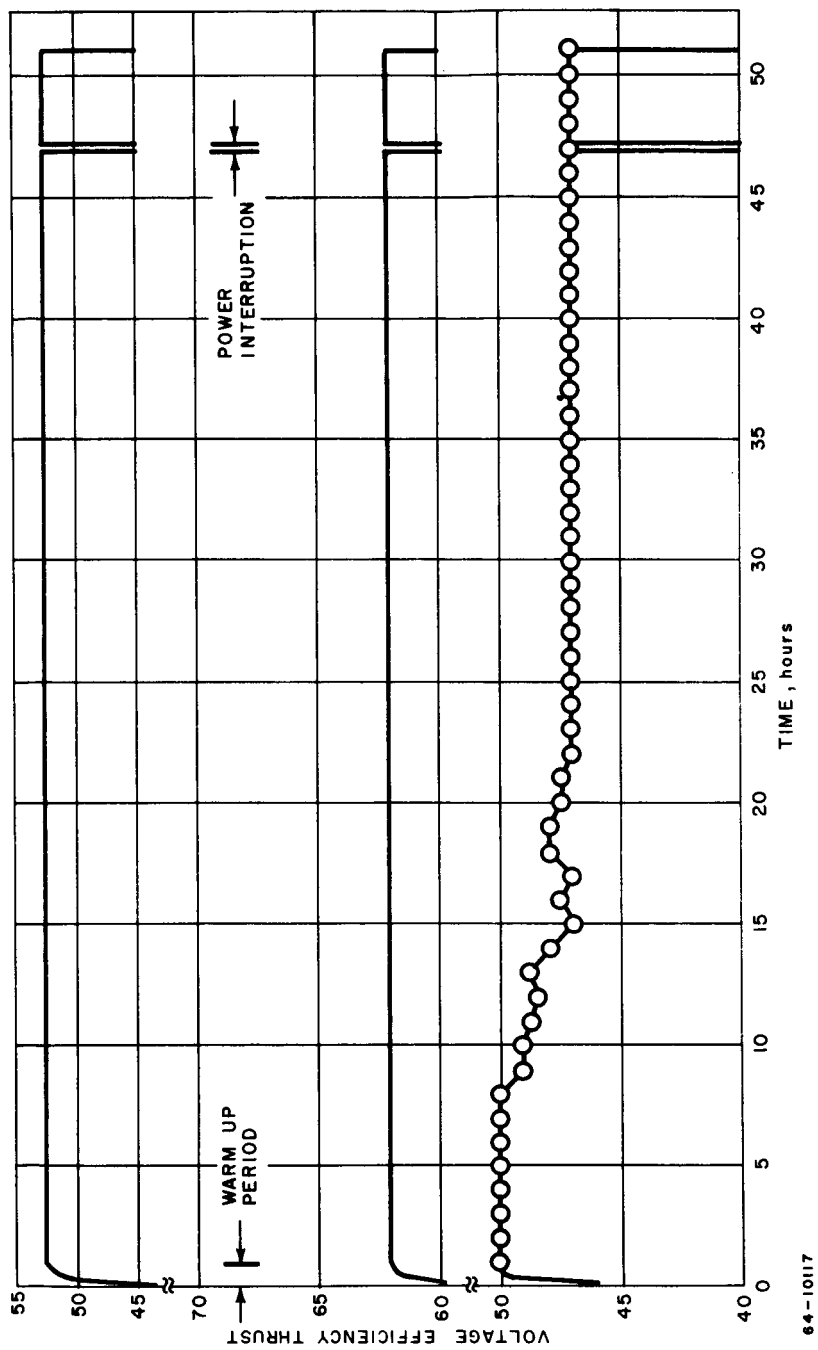


Figure 23 PERFORMANCE OF MARK III, MOD 3 THRUSTOR DURING 50-HOUR TEST

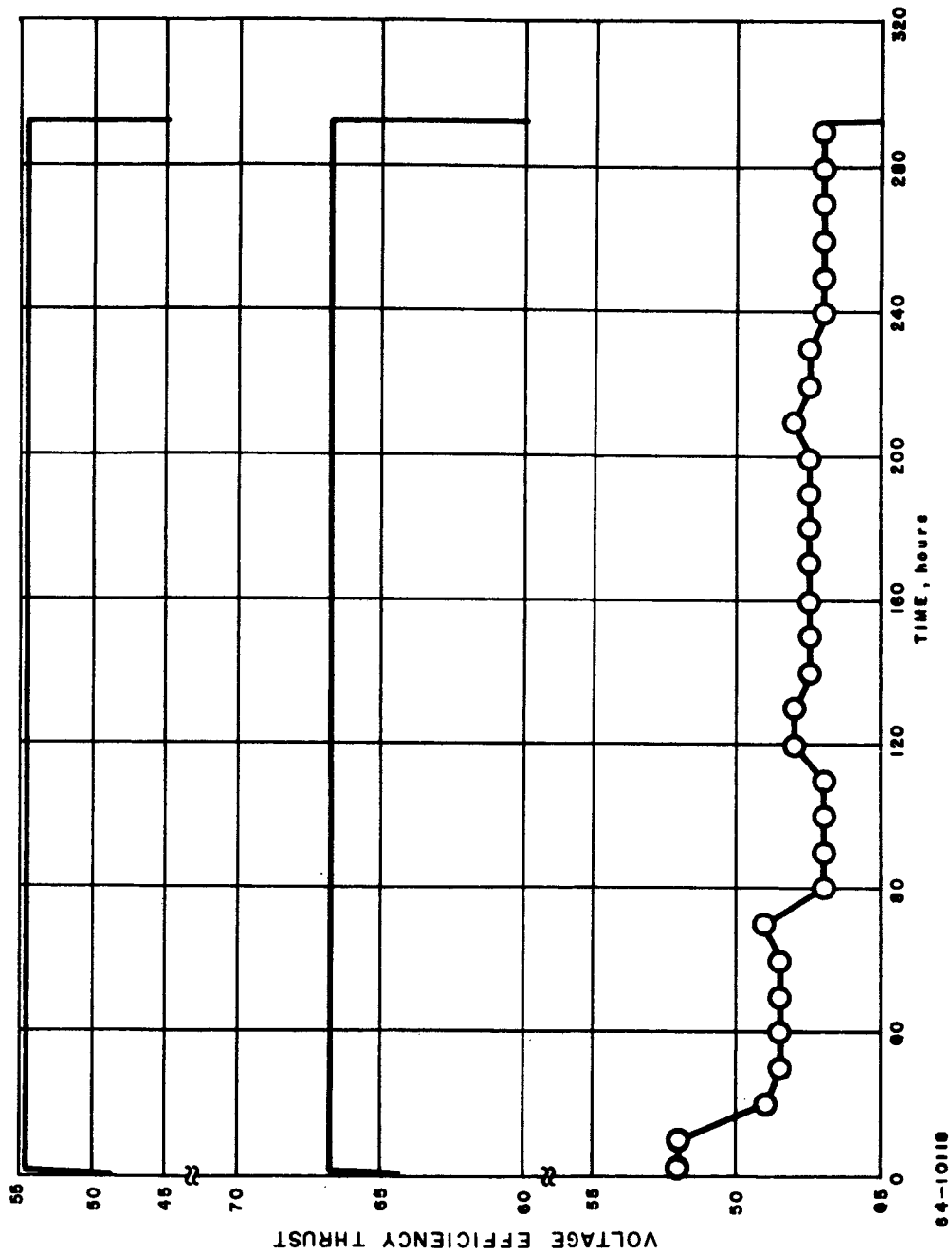


Figure 24 PERFORMANCE OF MARK III, MOD 4 THRUSTOR DURING 293-HOUR TEST

with the most downstream segment losing nearly 75 percent. It was thought possible that the wire holders on either side of this insulator touched, shorting out one coil and resulting in the voltage drop which caused termination of the test. This hypothesis prompted design of the Mod 5 thruster (see page 25), which has not yet been tested. The measured performance of the Mod 4 engine is compared with theory in paragraph C below.

C. ANALYSIS OF ENDURANCE TEST PERFORMANCE

In the following calculations the thrust, efficiency, and specific impulse are evaluated using the following measured values (chamber pressure, mass flow rate, nozzle geometry) and assumed values (ratio of specific heats and nozzle wall temperatures):

	Mod 3 (50-hour run)	Mod 4 (293-hour run)
Chamber pressure, P_o	2.03 atm	2.36 atm
Mass Flow Rate, \dot{m}	0.065 gm/sec	0.065 gm/sec
Throat area, A^*	0.01533 gm/sec	0.0137 cm ²
Geometric Area Ratio, A_{ex}/A^*	25.4	29.0
Nozzle half angle	15 degrees	15 degrees
Ratio of specific heats	1.3	1.3
Throat wall temperature T_w^*	1800°K	1800°K
Exit Wall Temperature, $T_w(ex)$	1500°K	1500°K

1. Thrust

The calculated value of thrust is obtained from the general thrust equation

$$F = \dot{m} U_{ex} \left(\frac{1 + \cos \alpha_{eff}}{2} \right) + (P_e - P_{amb}) A_{ex} - D_T \quad (1)$$

where

F = thrust

U_{ex} = flow velocity at the exit plane

α_{eff} = the nozzle divergence half-angle associated with the effective area ratio

P_e = static pressure at the exit plane

P_{amb} = ambient pressure at the nozzle exit

A_{ex} = the geometric area at the nozzle exit

D_T = total nozzle drag due to viscous effects.

To determine the static conditions at any point in the nozzle, an isentropic one-dimensional analysis is used in which the flow is assumed to be frozen at the plenum chamber conditions. Before an absolute value of thrust can be calculated the viscous effects in the nozzle (friction on the nozzle wall and boundary layer buildup which reduces the actual expansion area) must first be evaluated. The following subsection entitled (a) Actual Throat Size, (b) Stagnation Temperature, (c) Boundary Layer Displacement Thickness, (d) Viscous Drag, and (e) Thrust, all constitute steps in the overall calculation of engine thrust.

a. Actual Throat Size

The throat areas given in the table above are based on room temperature. It has been assumed that, in operation, the throat wall temperature is 1800°K. Using a coefficient of expansion for molybdenum of approximately 5×10^{-6} cm/cm-°K, the throat areas at operating temperature become 0.01554 cm² for the Mod 3 and 0.0139 cm² for the Mod 4.

b. Stagnation Temperature

The stagnation temperature, T_o is calculated from

$$a^* = \frac{\gamma M^* A^* P^*}{\dot{m}} = \left(\frac{\gamma R T^*}{\bar{M}} \right)^{1/2} \quad (2)$$

where

a^* = acoustic speed at the throat

M^* = Mach number at the throat

p^* = static pressure at the throat

R = universal gas constant

\bar{M} = molecular weight

T^* = static temperature at the throat

It is assumed that the expansion is isentropic and one-dimensional, characterized by a γ of 1.3. Then, $p^* = 0.546 P_0$ and $T^* = 0.87 T_0$. This results, for the Mod 3, in a T_0 of 2605°K, and for the Mod 4, in a T_0 of 2805°K.

c. Boundary Layer Displacement Thickness

The boundary layer displacement thickness is calculated from the relations presented by Burke and by Burke and Bird; and discussed in detail in appendix E.

The result of the coupled calculation is to give an actual area ratio of 15.6 for the Mod 3, and 17.5 for the Mod 4.

d. Viscous Drag

The drag forces are calculated according to the procedures specified in appendix E. The results are a total drag force of 4.99×10^3 dynes for the Mod 3, and 5.21×10^3 dynes for the Mod 4.

e. Thrust

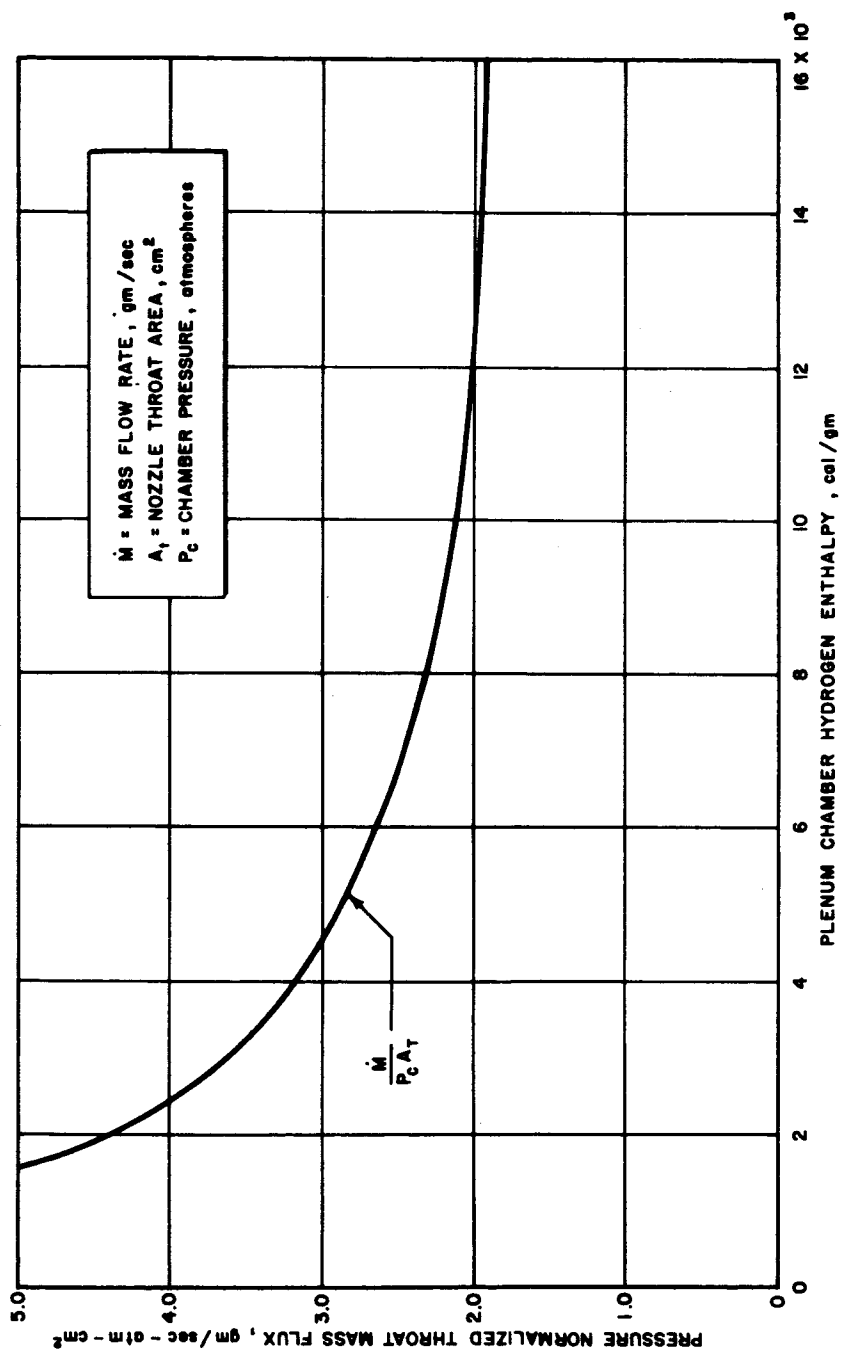
The actual nozzle thrust can now be calculated from the general thrust equation (1). For the Mod 3 test at the reduced area ratio of 15.6, the velocity is 8.14×10^5 cm/sec and the exit static pressure is 10.6×10^3 dynes/cm². Using an ambient pressure of 0.5 mm Hg, the thrust becomes 52.4 grams force. For the Mod 4 engine, with a reduced area ratio of 17.6, the exit velocity is 8.51×10^5 cm/sec and the static pressure 10.4×10^3 dynes/cm². Using an ambient pressure of 0.20 mm Hg, the thrust becomes 54.6 grams force.

2. Efficiency and Specific Impulse

The overall efficiency of the thruster is defined as the product of the separate heater, frozen flow, and nozzle efficiencies where the heater efficiency, ϵ_{heat} , is the ratio of the power delivered to the gas to the total input power, the frozen flow efficiency, ϵ_{froz} , is the ratio of the power available for conversion to thrust to the power in the gas, and the nozzle efficiency ϵ_{noz} , is the ratio of the actual thrust power to the power available for conversion to thrust. The thrust power is here defined as

$$P_{\text{TH}} = \frac{1}{2} \frac{F^2}{\dot{m}} \quad (3)$$

The heater efficiency can be determined from the pressure normalized throat mass flux, $\dot{m}/P_0 A^*$. For the Mod 3 this is calculated as 2.06 gm/sec-atm-cm². Referring to figure 25, this suggests an enthalpy for the Mod 3



64-754

Figure 25 PRESSURE NORMALIZED THROAT MASS FLUX VERSUS PLENUM CHAMBER HYDROGEN ENTHALPY

test of 11,600 cal/gm and for the Mod 4 test of 11,900 cal/gm. The total power in the gas is the product of the enthalpy and the mass flow rate, being 3.15 kw for the Mod 3 and 3.23 kw for the Mod 4. In turn, these are translated into heater efficiencies of 0.96 for the Mod 3 and 0.98 for the Mod 4. (The input power is 3-kw electrical + 0.28-kw initial thermal power). For hydrogen at a stagnation pressure of 2 atm and a stagnation temperature of 2600°K, the frozen flow efficiency is 0.93. Therefore, the nozzle efficiency is $(0.62)/(0.93)(0.96) = 0.70$. For the Mod 4 the nozzle efficiency is 0.76, since the frozen flow efficiency at 2800°K and 2.36 atmospheres is 0.89. Referring to figure 3, these nozzle efficiencies are in accord generally with theory.

From the enthalpies obtained from the pressure normalized throat mass flux an estimate of I_{sp} can be made, using

$$h_{ex} = I_{sp}^2 / 87.2$$

where

$$h_{ex} = \text{exhaust enthalpy, calories/gm}$$

For the Mod 3 one finds $I_{sp} = 810$ seconds, while for the Mod 4 it is 840 seconds.

The internal consistency of these numbers, along with their agreement with experiment lend confidence to the data obtained during the long runs of the Mods 3 and 4.

V. APPLIED RESEARCH

Throughout the analytical fluid flow studies of the resistojet, particularly the nozzle optimization study which appears as appendix E, two important assumptions have been made. The assumptions are: 1) the flow through the nozzle exhaust is one-dimensional (assumed because of the large heat transfer area and uniform heat transfer processes within the resistojet - see appendix D) and 2) the ratio of specific heats, γ , is equal to 1.3 (assumed as a direct result of Avco computer programs analyzing ideal one-dimensional isentropic flow and the thermodynamic behavior of hydrogen -- see appendix E). Two experiments were conducted to serve as a validation for these assumptions. They were an impact pressure probe of the resistojet exhaust to check the one-dimensional flow assumption and the operation of a thruster with various pressure taps in the flow to check the specific heats ratio assumption.

A. IMPACT PRESSURE PROFILE

1. Apparatus

The probe used to obtain the impact pressure profile was a total enthalpy probe, figure 26, manufactured by the Greyrad Corporation, Princeton, New Jersey; its design and performance are discussed in references 6 and 7. The probe was used as an impact pressure probe because its small dimensions (0.35 cm outside diameter and 0.089 cm sampling diameter, nozzle exit diameter = 0.712 cm) enabled taking a profile with good resolution.

The hydraulic probe insertion unit is shown in figures 27 and 28 in the retracted and extended positions respectively. (The probe shown on the insertion apparatus is not the Greyrad probe.) The probe itself is mounted on top of a structure containing two Gilman slides which permit movement in the nozzle exit plane. Also shown is a 0 to 5 psia strain gage pressure transducer connected directly to the probe to ensure a quick system response time.

The probe adjustment structure is mounted on circular roller bearings sliding on the surface of case-hardened steel bars. The entire insertion unit is bolted to a sliding track in the test tank which permits adjustment of the axial position of the probe relative to the nozzle exit plane.

The Gilman slides are motor driven; a microswitch and two pins in the vernier head of each Gilman slide are arranged so that after every half turn (corresponds to 0.0125-inch lateral motion) the motor stops automatically. Figure 29 shows the details for the horizontal motion. Both a mechanical counter and a channel on the recorder indicate the position of the probe during a traverse. It has been found that this unit permits location

of the probe during a traverse. Not shown in figures 27 and 28 is a copper, water-cooled heat shield mounted on the probe insertion sliding structure which protects the transducer, Gilman slide threads, and bearing surfaces from the nozzle exhaust. In addition, the transducer is also cooled by copper coils, also not shown. The Gilman slides are lubricated with a type of molybdenum grease which is 10 percent pure molybdenum powder colloiddally dispersed in a polyalkaline glycol compound. It was found that ordinary lubricants volatilized due to the vacuum leaving a residue that became semihard after prolonged exposure to heat.

2. Results

The data from impact pressure profiles taken at both 2.35 and 2.97 kw are shown in figure 30. Also shown in the same figure are the nozzle geometric exit diameter and the calculated boundary layer displacement thickness at the 3-kw power level. Both profiles are very flat over the area free from any boundary layer effects, that is, out to a radius of 0.060 inch. Hence, the assumption of one-dimensional flow appears to be valid. The sharp rises in the profile just before the rapid decay at the edge are not thought to actually exist in the flow but are instead an effect caused when the supersonic flow pattern at the nose of the probe is substantially altered by the probe body entering the boundary layer. Numerical integrations of both profiles yield thrust values of approximately 45 grams force, which are in qualitative agreement with experimental measurements and previous analytical studies.

B. PRESSURE TAP ENGINE

In order to determine the static pressure at various locations in the thruster chamber and nozzle, the Mark II, Mod 2 thruster was modified with four static pressure taps as shown sketched in figure 31. The taps are located in the chamber at the beginning of the converging section of the nozzle, at the nozzle throat, and at a geometric area ratio of 5.84. Data from two runs of this configuration are presented in table VIII.

Figure 32 presents data from the pressure tap engine at a geometric area ratio of 5.84. The two solid lines on the graph represent values of static to stagnation pressure ratios for area ratios of 5.84 and 4.70 using different values of γ . The values were taken directly from standard isentropic flow tables, as can be found, for example, in reference 8. The area ratio of 4.70 is the reduced area ratio, derived by calculating the boundary layer thickness using a γ of 1.3 (see appendix E). It should be noted on this figure that data from the instrumented thruster can only be represented by a line parallel to the abscissa. Therefore, a horizontal dash is just the crossing of one of the data lines with a theoretical curve. Considering the assumptions that go into the evaluation of the boundary layer displacement thickness and that all the data lie between γ values of 1.2 and 1.3, it appears that the assumption of $\gamma = 1.3$ is a valid one. Data taken from the pressure tap located at the nozzle throat,

although having no greater percentage error than the data at an area ratio of 5.84, was not amenable to drawing conclusions concerning the effective value of γ . This is because at the nozzle throat, γ is much more sensitive to variations in pressure than it is in the divergent section of the nozzle. Hence, the same scatter in pressure data that was experienced at an area ratio of 5.84 produces a greater variation in values of effective γ at the throat.

TABLE VIII

DATA FROM THE EXPERIMENTAL MARK II, MOD 2 THRUSTOR WITH PRESSURE TAPS

Wire(0.030 x 16 Inch 98 Percent W, 2 Percent ThO₂)Mass Flow Rate: 0.066 gm/sec H₂

Run 1 (venting pressure = 0.5 mm Hg)

Test Point	Times (minutes)	Voltage (volts)	Current (amperes)	Power (kilowatts)	Tap 1 (mm Hg)	Tap 2 (mm Hg)	Tap 3 (mm Hg)	Tap 4 (mm Hg)
1	0	0	0	0	2.4	15.2	12.7	15.3
2	25	21.0	62.0	1.30	24.1	378.0	696.0	712.0
3	32	26.0	64.0	1.66	27.6	406.0	786.0	817.0
4	40	29.5	66.5	1.96	29.8	474.0	874.0	894.0
5	45	36.0	72.5	2.61	32.8	492.0	936.0	956.0
6	50	40.5	76.0	3.08	34.2	562.0	993.0	1003.0

Run 2 (venting pressure = 0.4 mm Hg)

Test Point	Times (minutes)	Voltage (volts)	Current (amperes)	Power (kilowatts)	Tap 1 (mm Hg)	Tap 2 (mm Hg)	Tap 3 (mm Hg)	Tap 4 (mm Hg)
1	0	0	0	0	0.8	12.7	1.0	17.0
2	10	13.5	53.0	0.72	18.6	334.0	611.0	627.0
3	15	20.0	56.0	1.12	21.8	378.0	676.0	688.0
4	20	25.5	60.0	1.53	24.7	422.0	755.0	770.0
5	25	33.5	64.0	2.14	29.1	490.0	864.0	884.0
6	30	37.0	66.0	2.44	30.9	515.0	905.0	926.0
7	40	40.0	75.0	3.00	33.5	556.0	977.0	990.0

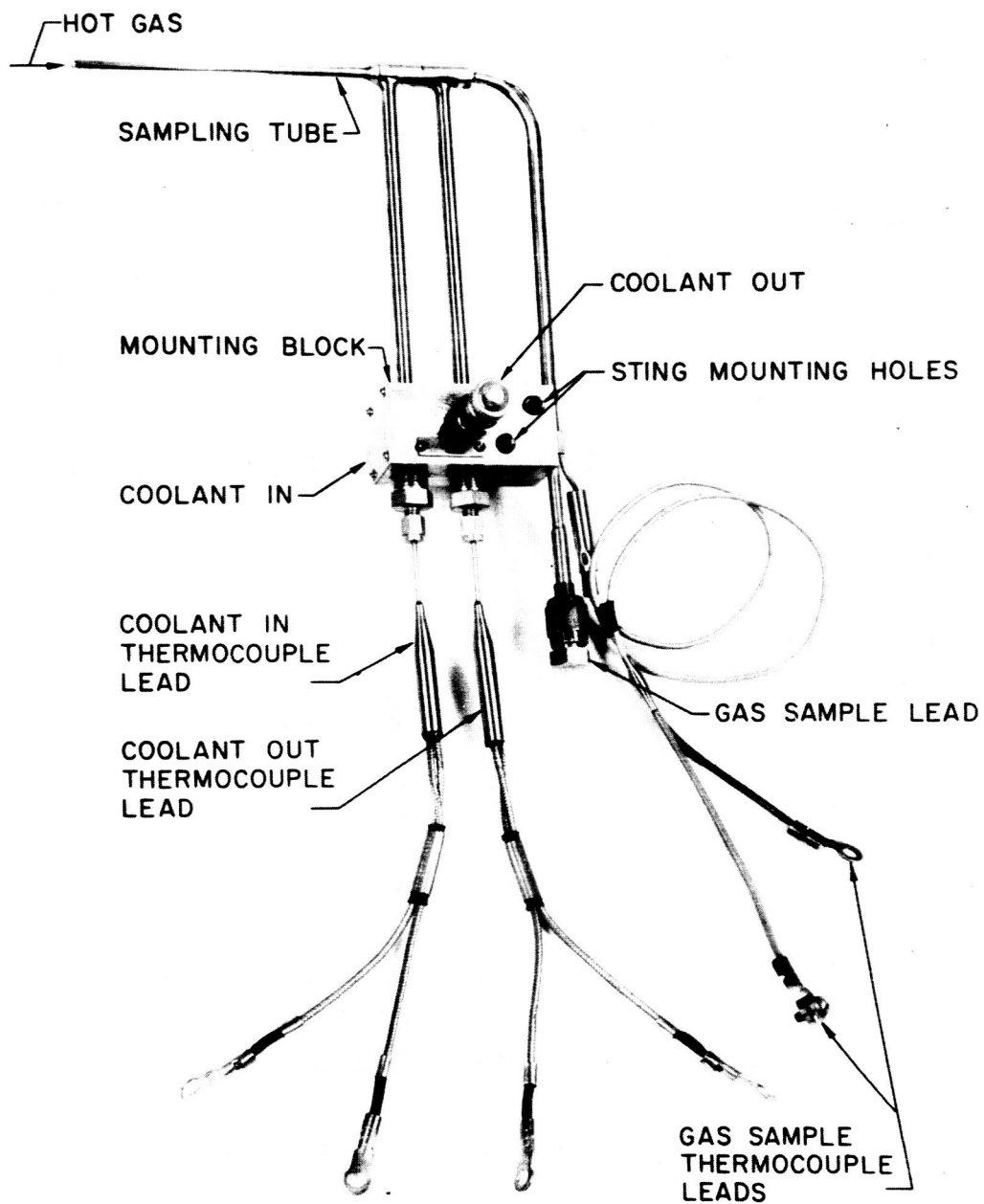


Figure 26 GREYRAD ENTHALPY PROBE
64-10355

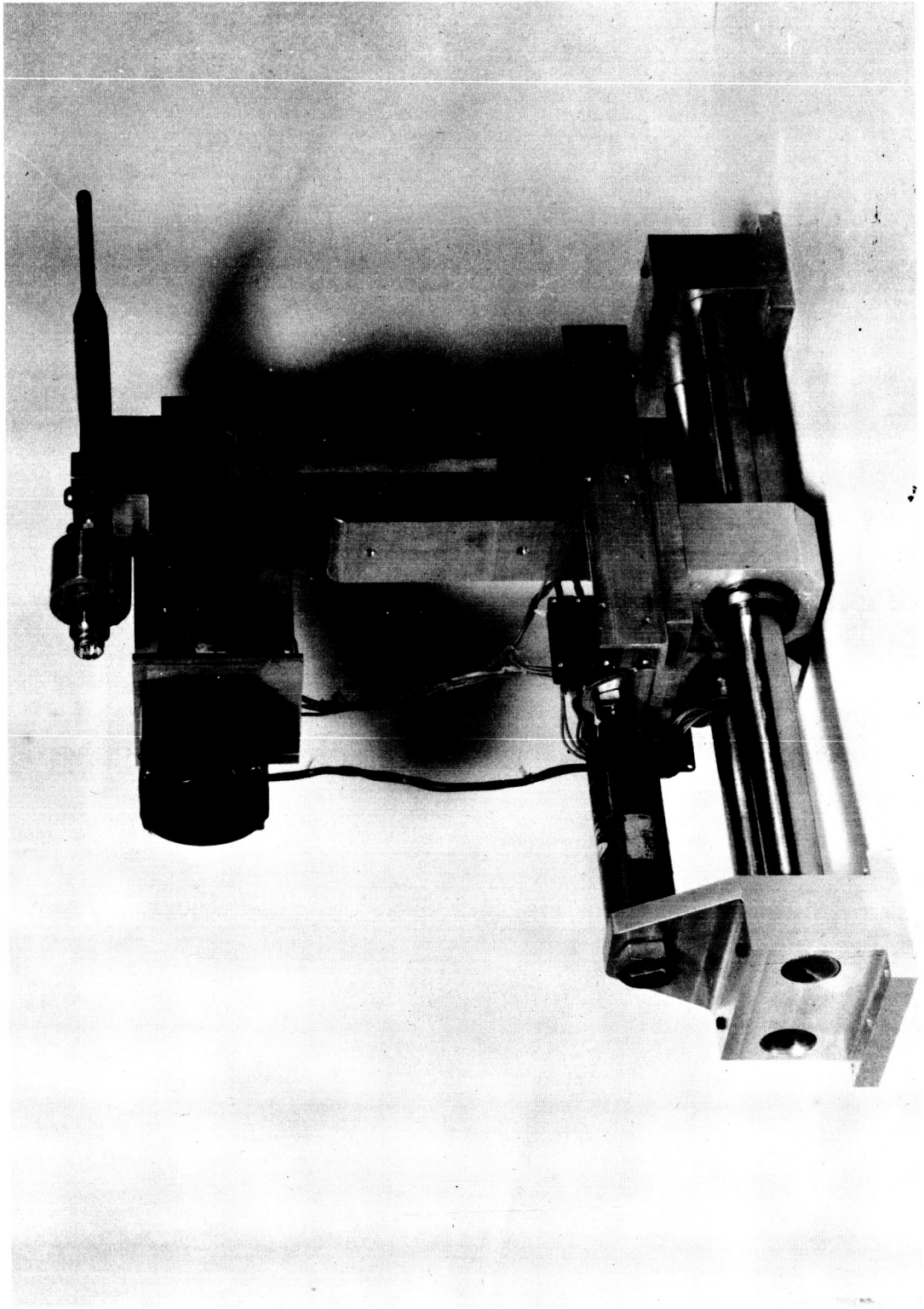


Figure 27 FRONT VIEW OF PROBE INSERTION UNIT
64-10356

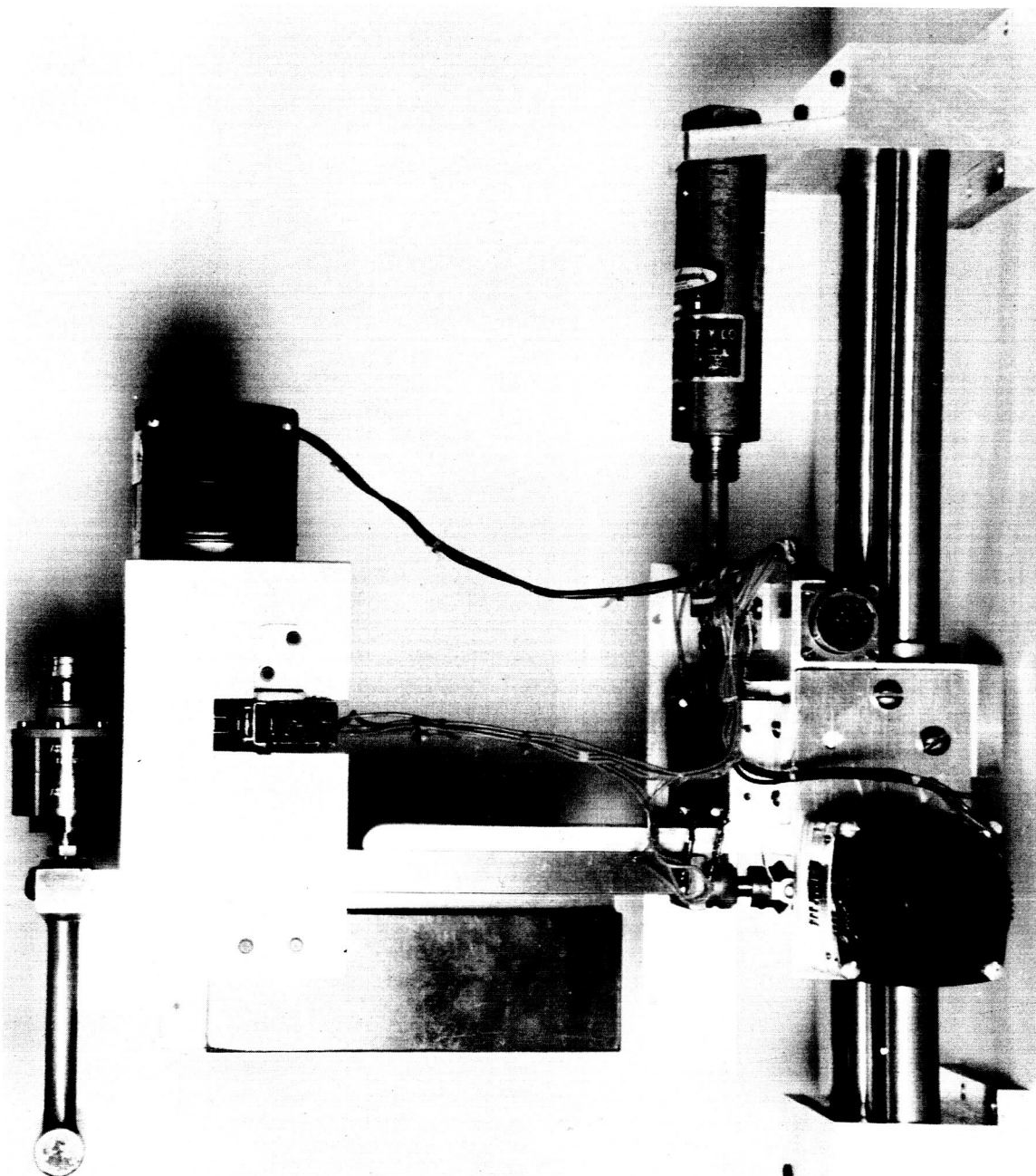


Figure 28 REAR VIEW OF PROBE INSERTION UNIT
64-10357

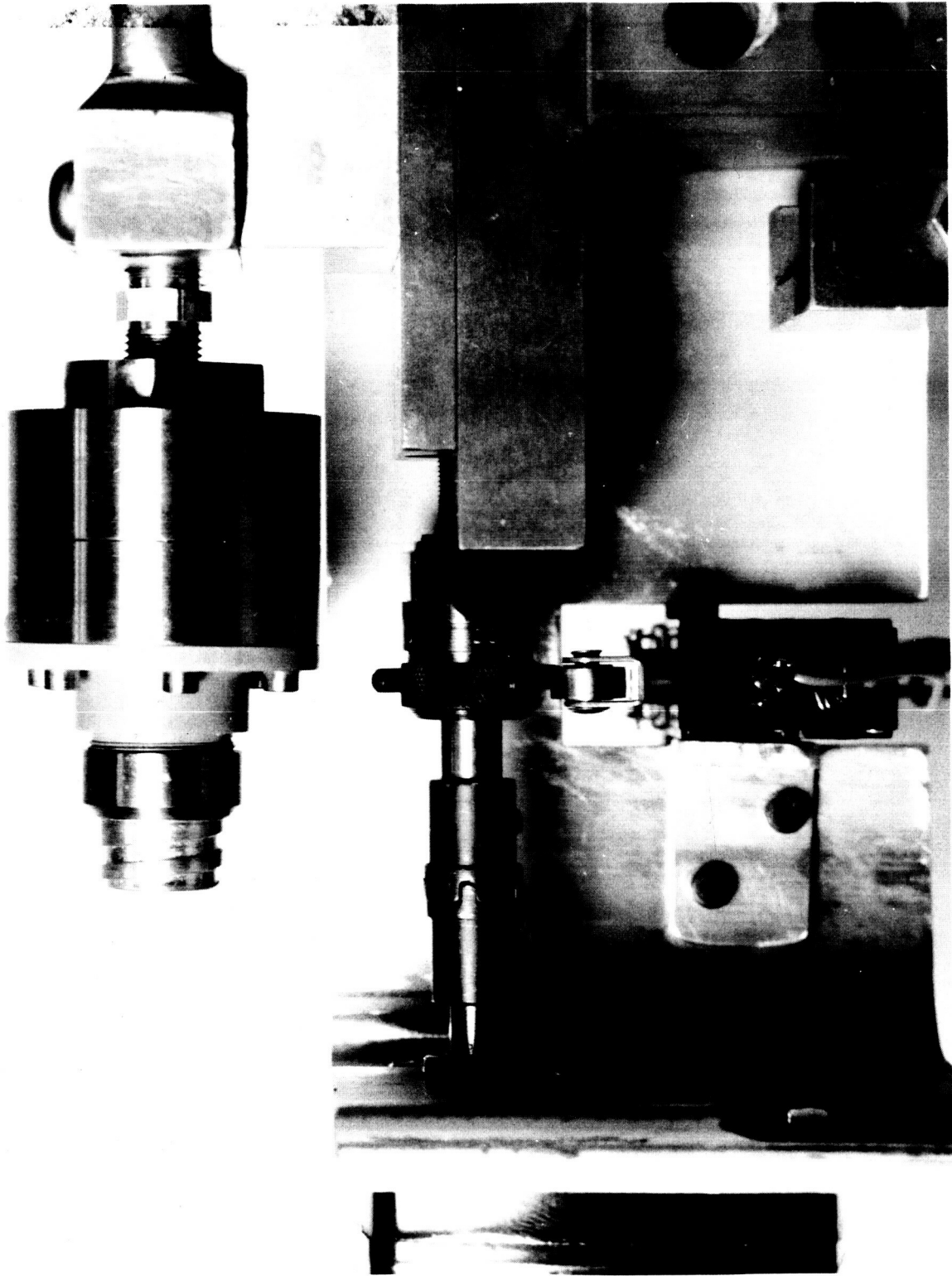


Figure 29 CLOSEUP OF MICROSWITCH FOR GILMAN SLIDE DRIVE ASSEMBLY

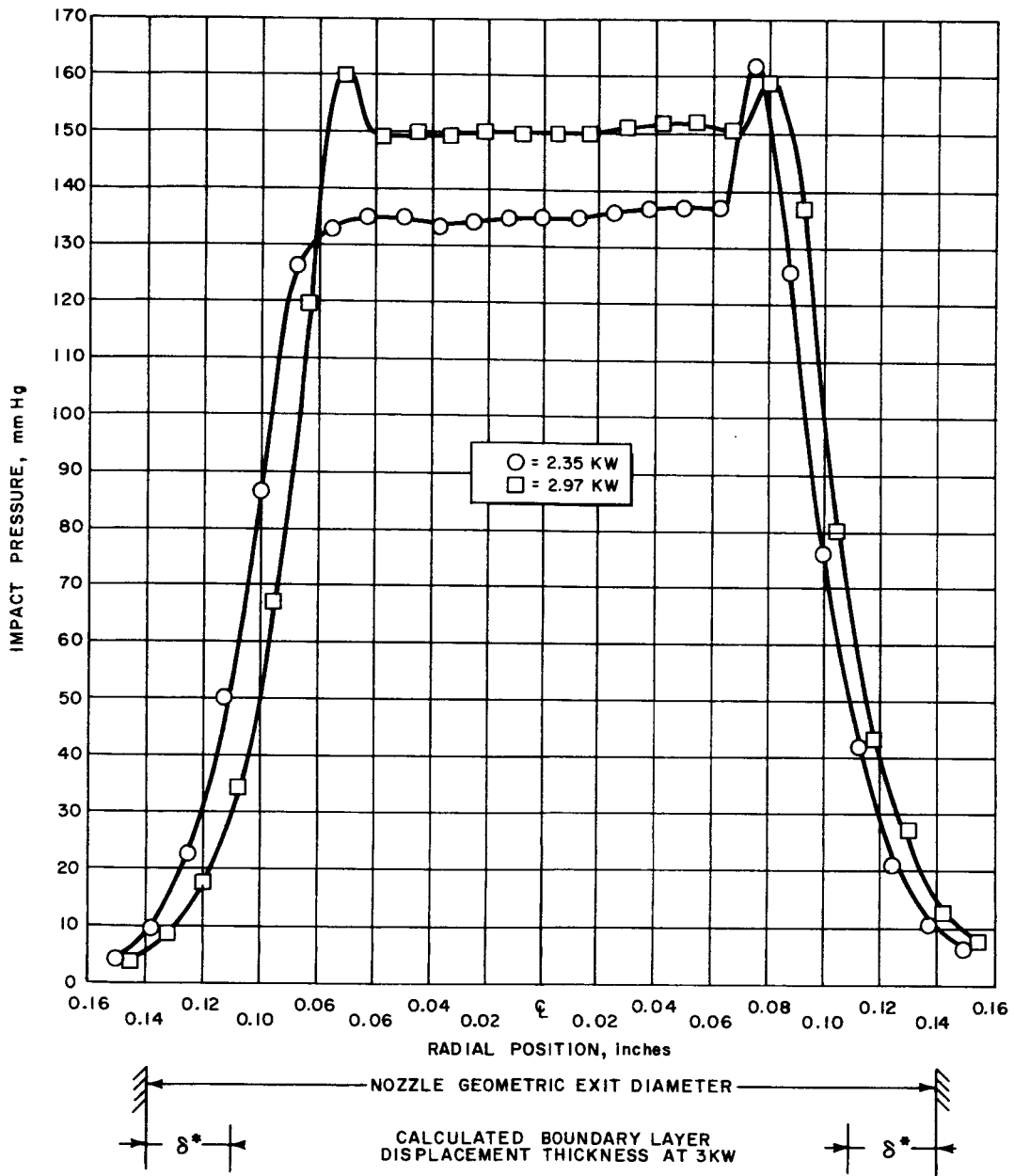
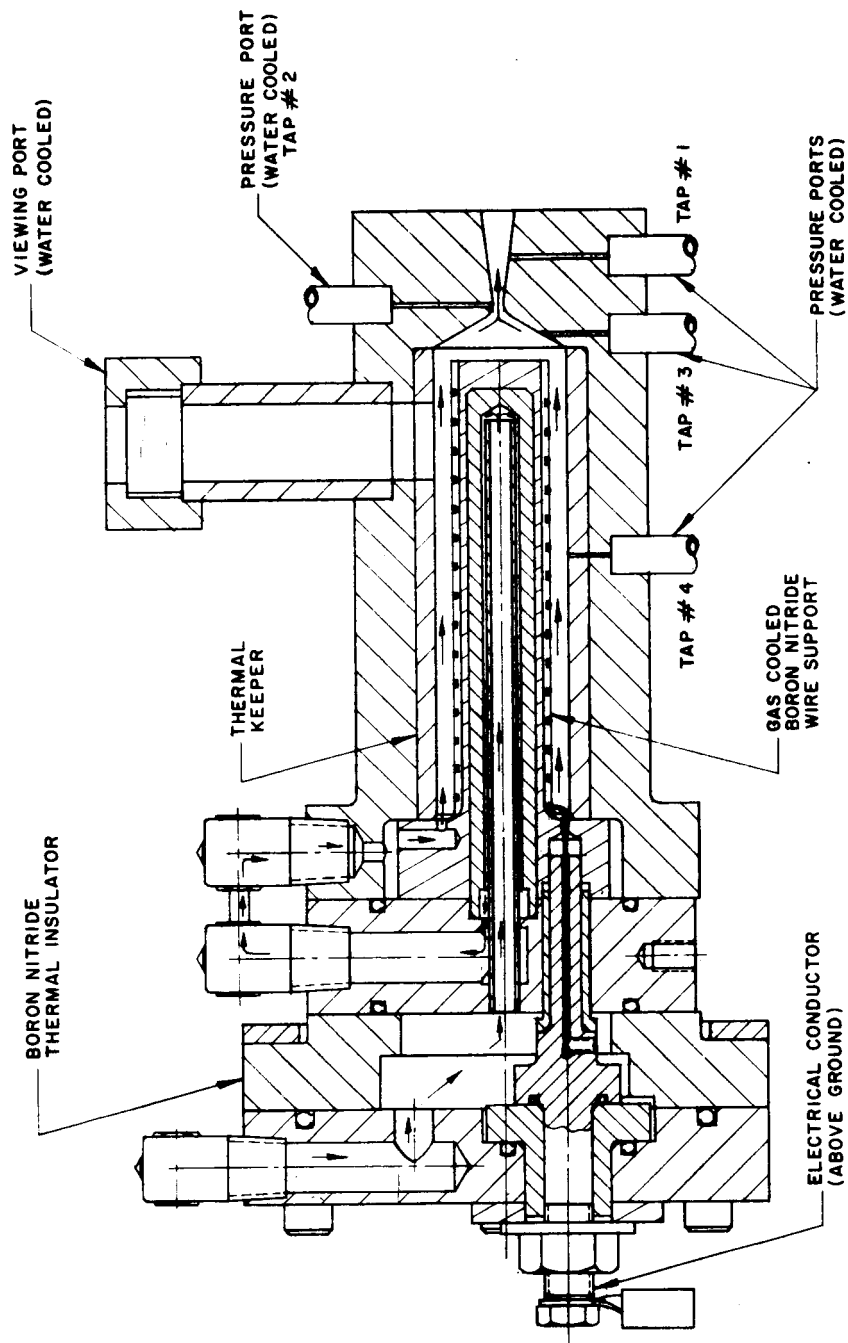


Figure 30 RESISTOJET IMPACT PRESSURE PROFILE



64-750

Figure 31 MARK II, MOD 2 THRUSTOR WITH PRESSURE PORTS

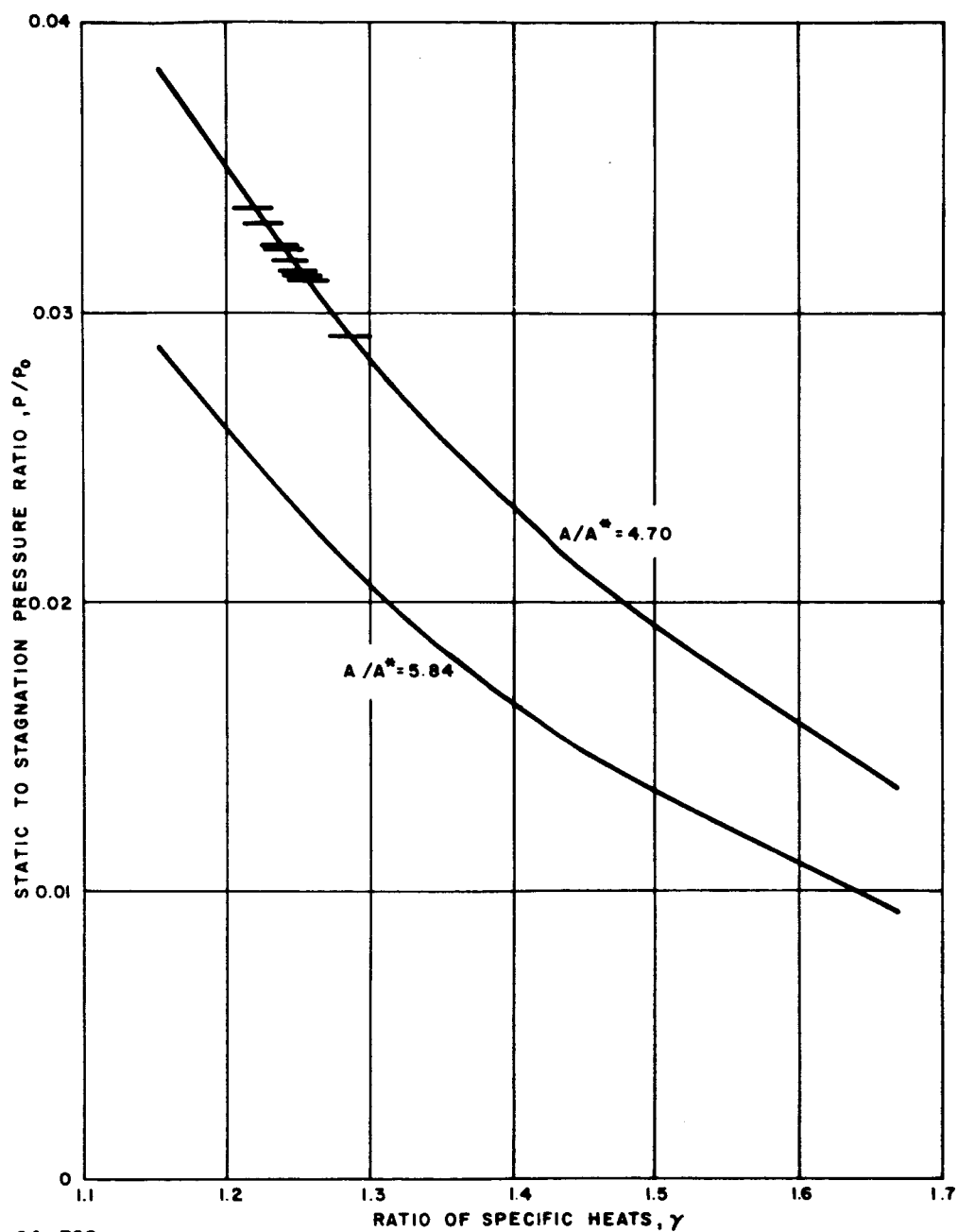


Figure 32 EXPERIMENTAL STATIC TO STAGNATION PRESSURE RATIOS FROM THE PRESSURE TAP THRUSTOR, $A/A^* = 5.84$

VI. PROGRAM DIRECTION

Thrustor lifetime of several months for the performance range $I_{sp} = 800$ to 850 seconds and $P_{in} = 2$ to 3 kw appears to be within reach, at efficiencies of approximately 65 percent. This conclusion is based on the facts that (1) this performance range has been obtained with the Mark III series of thrustors, and (2) the thrustor failure after 293 hours was not associated with the heater elements, and is considered not to be basic to the wire coil heater concept. A physical redesign has been made which may eliminate the problem.

Future program emphasis should be placed on the development of thrustors and thrustor systems for operation in the pulsed mode.

VII. REFERENCES

1. Jack, J. R., Theoretical Performance of Propellants Suitable for the Electrothermal Jet Engine, ARS J. 31, 1685-1689 (1961).
2. Howard, J., The Resistojet, ARS Space Flight Report to the Nation, ARS Preprint 61-2126 (October 1961).
3. Howard, J., Op. cit.
4. Jack, J. R., and E. Spisz, NASA Research on Resistance Heated Hydrogen Jets, AIAA Electric Propulsion Conference, AIAA Preprint 63-023 (March 1963).
- 4a. Short, G. R., and J. Howard, Sublimation of tungsten by hydrogen, AIAA preprint 63-024 (March 1963).
5. Howard, J., op. cit.
6. Grey, J., P. F. Jacobs, and M. P. Sherman, Rev. Scien. Inst., 33, 738, (1962).
7. Grey, J., Rev. Scien. Inst., 34, 857, (1963).
8. Shapiro, A. H., The Dynamics and Thermodynamics of Compressible Fluid Flow, Vol. 1, Roland Press Co., New York (1953).

APPENDIXES

APPENDIX A

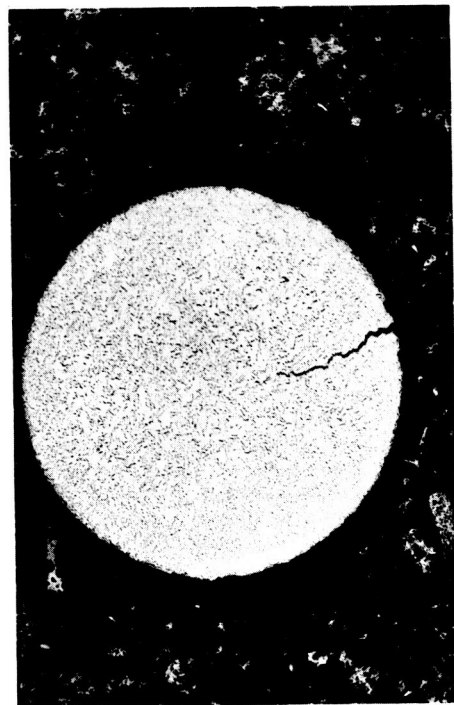
RECRYSTALLIZATION AND GRAIN GROWTH

The requirement of sustained operation at temperatures in the range 2500° to 3000°K has led to the selection of tungsten, or a tungsten alloy, for use as the wire coil heater element. In order to determine the effects of high-temperature operation on the microstructure of these elements, a metallographic study was undertaken.

Figure A-1 shows the photographs of the microstructure of an unheated, 30-mil diameter thoriaated tungsten (98 percent W-2 percent ThO_2) wire; the photographs show the structure perpendicular (top) and parallel (bottom) to the wire drawing direction. (The crack present in the cross section occurred during metallographic preparation.) The dispersed thoria phase is not apparent at the 100 x magnification. Examination at greater enlargements showed the thoria to be reasonably uniform in size and evenly dispersed throughout the cross section of the wire. The thoria proved unaffected during high temperature runs. The most important observation from figure A-1 is the fine, uniform grain structure which is apparent in both cross sections. The sections of wire shown in figure A-2 are representative of wire which has been in a resistojet engine for 120 minutes at about 2400°K. Figure A-2a shows the microstructure perpendicular to the wire drawing axis. After comparing this structure to that in figure A-1, it is apparent that grain coarsening has occurred. In the corner of the photomicrograph is a wire cross section parallel to the drawing axis. This structure also illustrates the onset of grain coarsening. The structure in figure A-2b shows considerable grain growth. It is from the same wire as the top photomicrograph but at a different location along the wire. Figure A-2c shows the structure along the longitudinal axis of the wire at the position where the coarse grains (figure A-2b) were observed. The change in microstructure from coarse grains to finer ones is readily apparent.

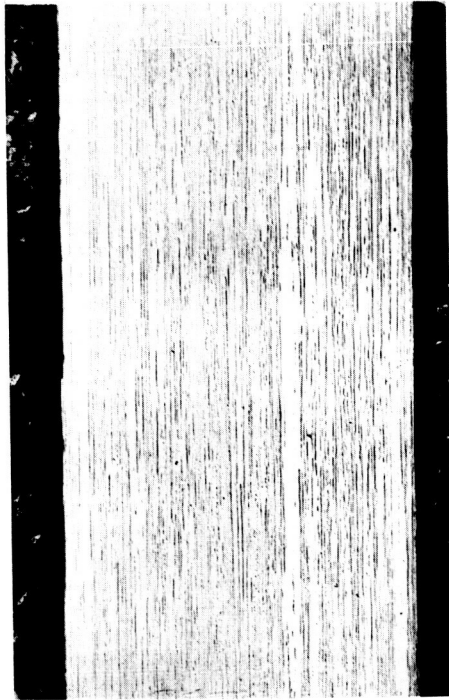
The recrystallization temperature for tungsten with 2 percent thoria is in the range 1800° to 2000°C depending on the amount of deformation sustained during the wire drawing operation.^{A-1} Since the nominal operating temperature of this wire is only slightly above the wire recrystallization temperature, the differences in microstructure in figure A-2 presumably resulted from minor temperature variations along the wire.

The microstructures shown in figure A-3 are representative of a wire run for 240 minutes at about 2400°K. The perpendicular and parallel microstructures both exhibit an extremely large grain size which result from recrystallization and grain growth. The larger grain size in these structures, compared to those recrystallized and enlarged grain size structures in figure A-2, is the result of longer time at temperature. The wire shown in figure A-3 was completely recrystallized as compared to the partially recrystallized structures in figure A-2.



P3395

100x

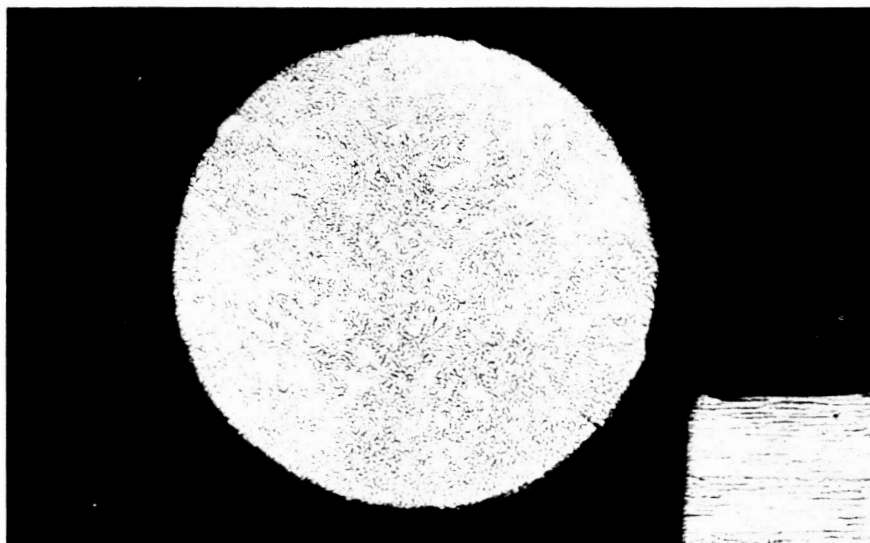


P3395A

100x

64-767

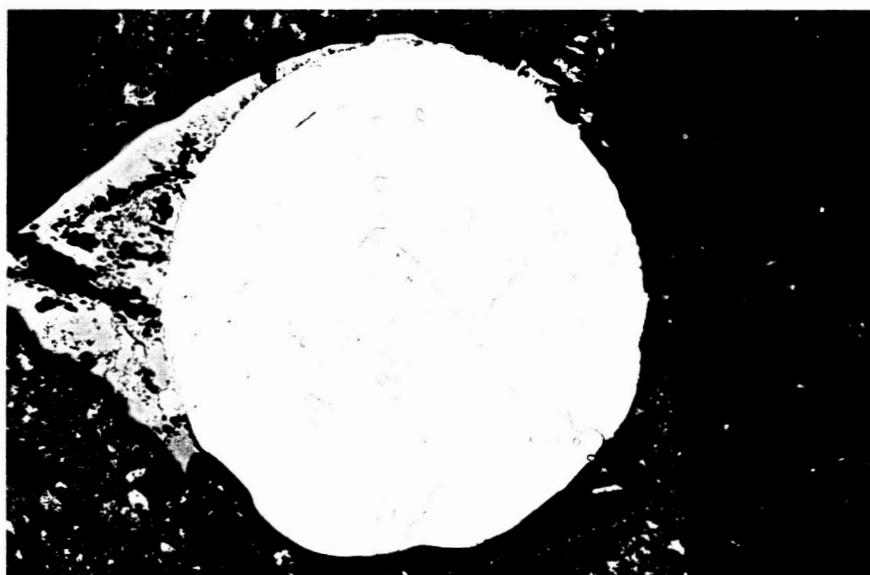
Figure A-1 30-MIL THORIATED TUNGSTEN WIRE, UNUSED



P 3395 B

A

100 x



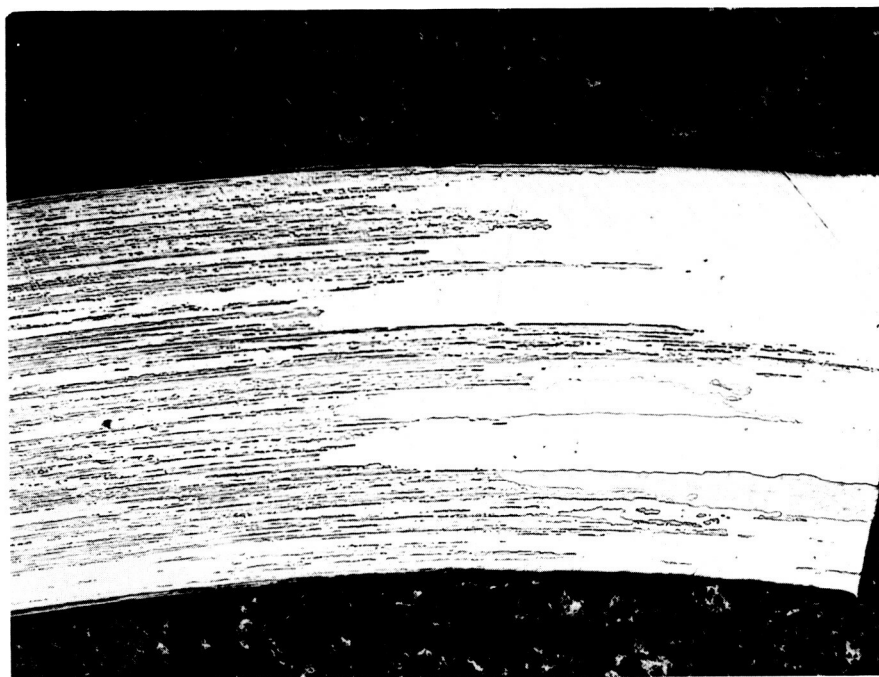
P3399E

B

100 x

64-769

Figure A-2 30-MIL THORIATED TUNGSTEN WIRE, AFTER 120 MINUTES AT 2400 °K



P 3395 C
64-769

C

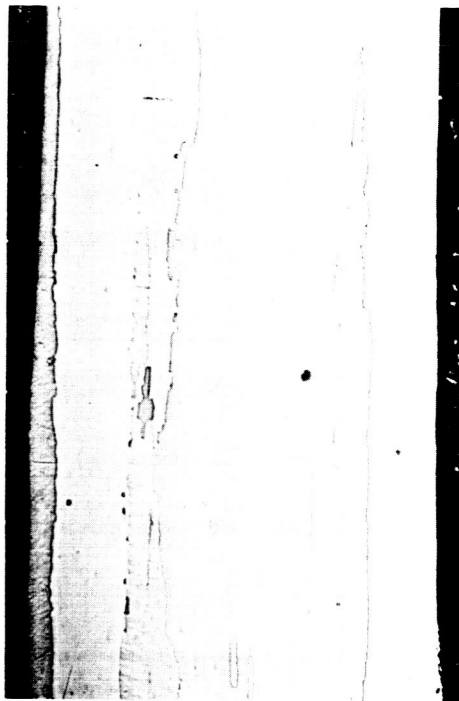
100 x

Figure A-2 (Concl'd)



P 3395 D

100 x



P 3395 E

100 x

64-770

Figure A-3 30-MIL THORIATED TUNGSTEN WIRE, AFTER 240 MINUTES AT 2400 °K

These figures indicate a severe grain growth after four hours of operation at approximately 2400°K. Based on this rate of growth, grains having a diameter equal to the wire diameter would form in running times much shorter than 50 hours. Since materials are generally weaker along the adjacent faces of grains, these large grains could lead to possible failure of the heater element. Hence, a study was undertaken to find a tungsten alloy with an additive that more effectively prohibited grain growth than the 2 percent thoria did and hence would exhibit greater ductility.

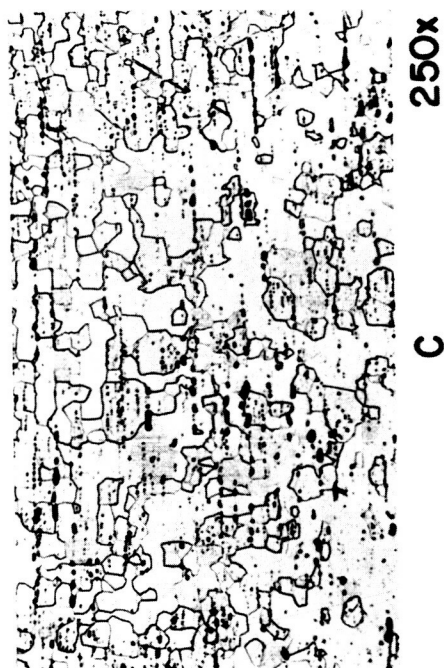
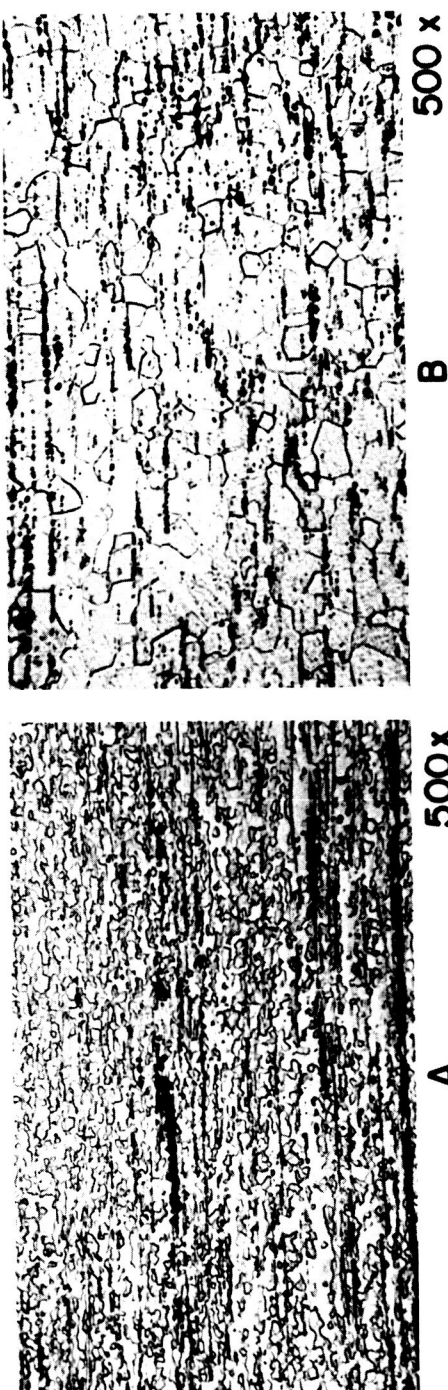
One of the materials studied was an alloy of 75 percent tungsten-25 percent rhenium. Wires made of this alloy were extremely ductile at room temperature. Figure A-4 shows photomicrographs of tungsten rhenium wires at various stages of heating. In figure A-4a an unused wire is shown. The grain size is very small and uniform. Figure A-4b shows a wire specimen that had been run in a bench test configuration for one hour at approximately 2700°K. Although recrystallization and some grain growth occurred, the sample was still ductile enough to unwind the coil. A tungsten-rhenium wire run in a thruster configuration for 50 hours at a temperature of about 2800°K is shown in figure A-4c. The wire coil was still extremely ductile after completion of the test. It is evident that this ductility is caused by the fact that the amount of grain growth has not substantially changed between run times of one and 50 hours. Hence, the conclusion can be drawn for heating elements composed of 75 percent tungsten-25 percent rhenium that recrystallization and grain growth occur quite rapidly during running times of the order of 1 hour, but for running times longer than 1 hour the rate of grain growth rapidly decreases.

Photomicrographs of a microstructure representative of that found in the 75 percent tungsten-25 percent rhenium heating elements run for 293 hours at 2800° to 3000°K are shown in figures A-5a and A-5b. The black spots result from small grains being pulled out of the sample during preparation. These photomicrographs illustrate the large grain size which has developed from extended operation at elevated temperature. This amount of grain growth is not prohibitively large since the heating elements were still fairly ductile and could be removed from the thruster without breakage after the run.

The possibility of boron or nitrogen diffusing from the boron nitride into the tungsten and influencing the recrystallization characteristics of the wire was also examined. To accomplish this, a tungsten wire was heated in hydrogen for 45 minutes at a nominal temperature of about 2400°K but without contact with boron nitride. As shown in figure A-6, recrystallization and grain growth did occur. Because of the similarity between figure A-6 and figure A-2 (a wire heated in contact with boron nitride for 120 minutes at about 2400°K), it was concluded that boron nitride does not exert a measurable influence on the recrystallization characteristics of tungsten.

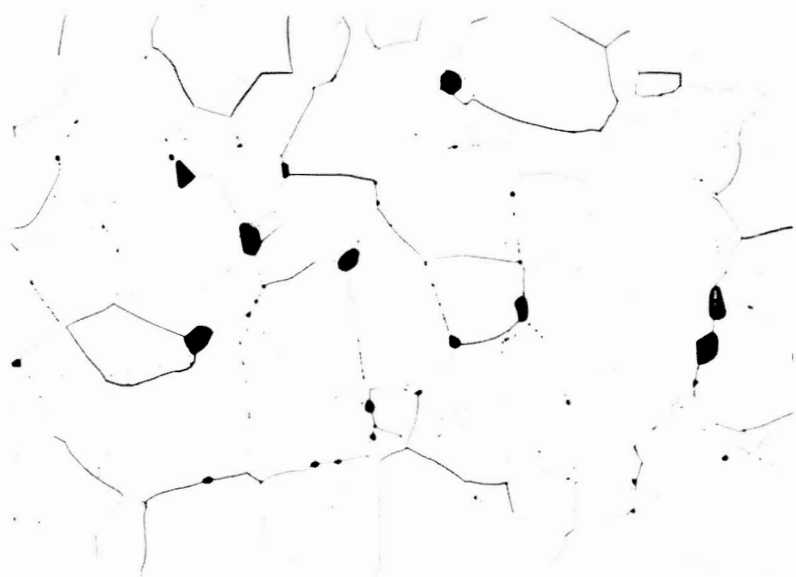
Reference

1. DMIC Report 191, p. A-77 to A-80 (27 September 1963).



64-3300

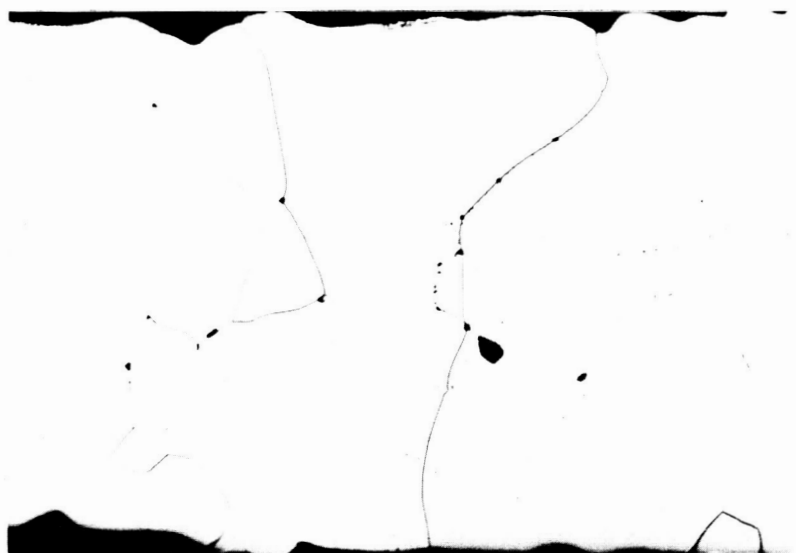
Figure A-4 75 PERCENT TUNGSTEN-25 PERCENT RHENIUM WIRE



P3522

1A

250X

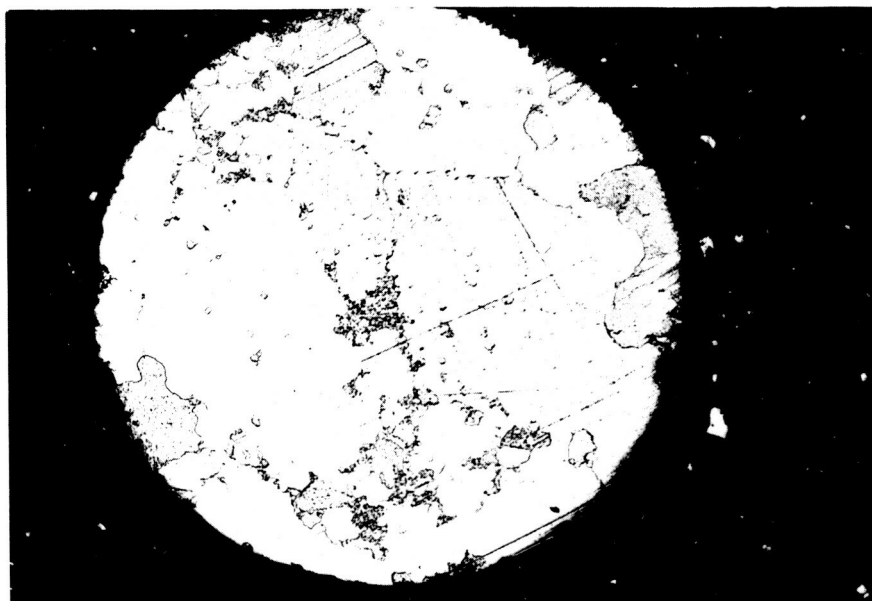


P3522 A

1B

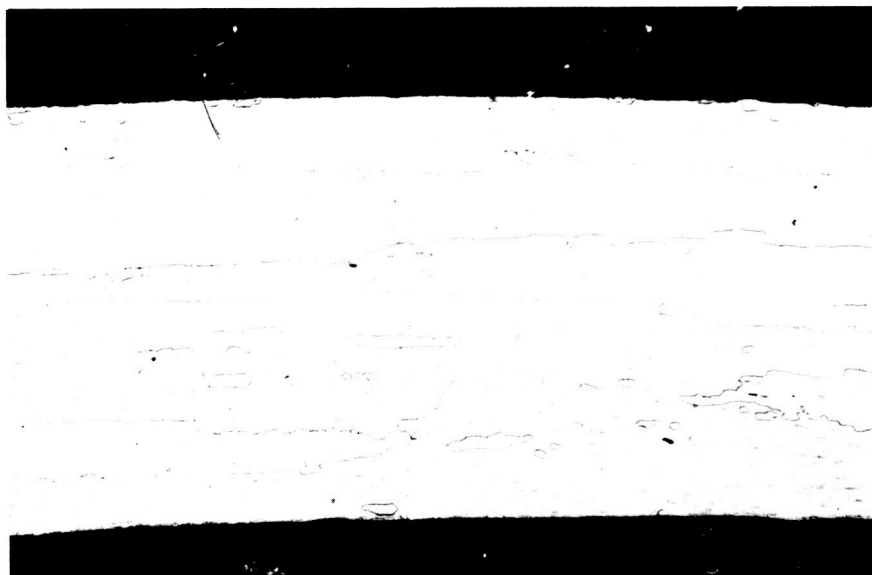
250 X

Figure A-5 75 PERCENT TUNGSTEN-25 PERCENT RHENIUM WIRE, AFTER 293 HOURS AT 2800 °K



P3399 C

100 x



P3399 D
64-772

100 x

Figure A-6 30-MIL THORIATED TUNGSTEN WIRE, 45 MINUTES AT 2400°K WITHOUT BORON NITRIDE CONTACT

APPENDIX B

BORIDE FORMATION

At the time that tungsten, or a tungsten alloy, was chosen for the high temperature heating element and boron nitride was selected for the high temperature thermal and electrical insulator, the only precaution which appeared necessary was the operation of the heater element at a temperature low enough so that wire evaporation would be kept at a tolerable level. However, certain heater element failures after running times of a few hours, which appeared not to be associated with the evaporation of tungsten, led to the initiation of metallographic and x-ray analyses of elements which had failed in order to determine the microstructure and composition of tungsten alloy heater elements which had come into close contact with boron nitride at elevated temperatures.

The structure shown in figure B-1 was found in a wire which had been operated for 240 minutes at 2400°K . This section, parallel to the wire drawing axis, shows a coarse grain structure and also a cast structure. This cast structure (lower left portion of the wire) indicates that melting occurred during operation of the engine at the point of contact between the wire and the boron nitride. X-ray analysis revealed that the melted portions of the wire were composed of tungsten boride (WB) and thorium oxide (ThO_2). Thus, where the wire was in close contact with the boron nitride support mandrel, boron diffused into the wire forming tungsten boride. The tungsten-boron binary system has been studied^{B-1} and is helpful in discerning the cause of the localized melting. The tungsten boride compound has a melting point of $3130 \pm 80^{\circ}\text{K}$ while that of pure tungsten is 3655°K . However tungsten and the tungsten boride compound exhibit a eutectic reaction with a melting point of approximately 2300°K , although the exact melting point has not been determined. On the basis of the positive identification of tungsten boride in the tungsten wires at the locations where melting occurred, and considering the fact that the heater element must be operated at about 2800°K for performance levels of interest, it can be concluded that the wire failures were caused by the eutectic melting of tungsten and tungsten boride.

In a subsequent thruster configuration (the Mark III Mod 2) in which contact between the tungsten wire and boron nitride was avoided, the wire coil heater element was supported on small tungsten pins which were in turn imbedded into boron nitride. After run times of the order of a few hours, it was observed that although the wire showed no signs of erosion or localized heating, the tungsten support pins revealed severe cracking and deformation at the end in contact with boron nitride insulation. Both the wire and the tungsten support pins were submitted to metallographic and X-ray analyses.

The X-ray analysis revealed that in the support pins, two types of tungsten boride has formed during operation of the thruster; they are WB and W_2B_5 . These findings were substantiated by metallographic studies of the distorted ends of



P3399B

100x

64-774

Figure B-1 FAILURE LOCATION OF 30-MIL THORIATED TUNGSTEN WIRE AFTER 240 MINUTES AT 2400°K

the pins which revealed the microstructures shown in figures B-2 and B-3. In figure B-2a the white phase is tungsten while the gray is WB and/or W_2B_5 . The same field is shown in plane polarized light in figure B-2b. In this figure, the solid black is the tungsten, the white dots are thoria particles, and the gray-white, acicular or needle-like crystalline structure is the tungsten boride. In figure B-3, metallographic evidence is shown of the presence of tungsten boride in a region beginning to deform. The crack and the darker gray phase at the pin surface and along the crack surface in figure B-3a indicates that tungsten boride was beginning to form in this pin. The same field is shown in figure B-3b viewed in plane polarized light. The acicular structure is gray-white, similar to that in figure B-2b, and confirms that this structure is tungsten boride.

A portion of the wire microstructure from this same thruster configuration is shown in figure B-4a. Although most of the wire was free of unknown phases, the gray structure was evident at locations where the wire was in contact with the tungsten support pins. Figure B-4b shows this structure in plane polarized light, and its similarity to those of figures B-2b and B-3b is apparent indicating that tungsten boride has begun to form in portions of the wire as well as the support pins.

As an independent check of the above analysis, microhardness measurements were made in the tungsten and the tungsten boride phases of the wire and support pins. Microhardness measurements are made with a constant load on the indenter. Therefore, a larger indentation indicates a softer material. Figure B-5a shows the hardness indentations in the tungsten and tungsten boride phases of one of the support pins. The large indentation is in the tungsten while the smaller one is in the gray tungsten boride. The wire structure is shown in figure B-5b with the hardness indentations present. In both figure B-5a and B-5b the tungsten had an average hardness of 450 to 500 Knoop, and the hardness of the tungsten boride was about 2100 to 2600 Knoop. These hardness values are within the range of accepted values for tungsten and tungsten boride B-2 thereby substantiating the results of the X-ray analyses.

A later modification of the thruster consisted of series connecting five shorter wire coils to large molybdenum segments and succeeded in keeping the wire free of any boride phases throughout runs of up to 293 hours in duration. However, X-ray analysis revealed that boride phases were formed in the molybdenum support segments. A typical photomicrograph of a molybdenum support segment which had been in contact with boron nitride for 293 hours is shown in figures B-6a and B-6b. Figure B-6a shows a second phase with a cast or long, narrow-grained structure oriented perpendicular to the edge of the molybdenum structure (upper portion of the photomicrograph). This phase was identified by X-ray diffraction to the MoB, molybdenum boride, and was found at all locations in the molybdenum where contact with the boron nitride insulators occurred. It should be noted that figure B-6a shows a third phase, the narrow band separating the MoB from the unaffected molybdenum. This is especially apparent in

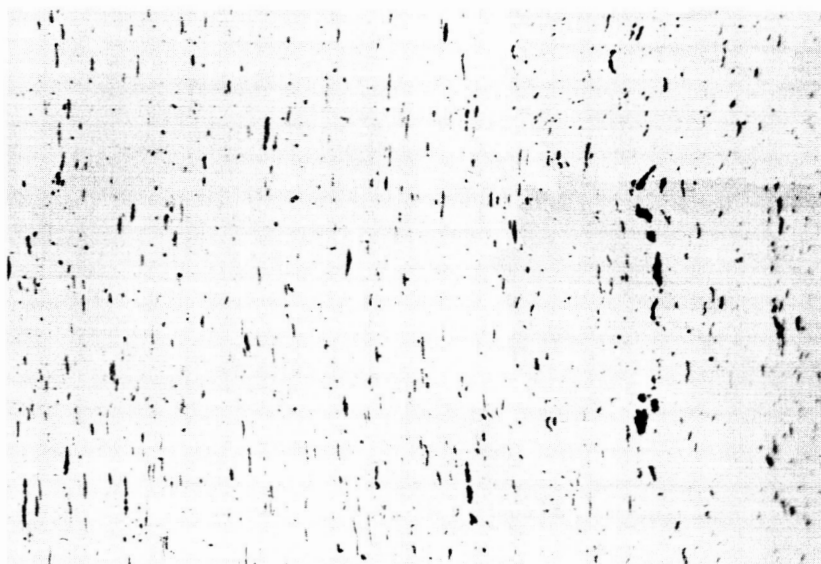
figure B-6b which is the same field viewed in polarized light. The molybdenum-boron phase diagram B-3 shows that molybdenum rich phases Mo_2B and Mo_3B_2 do exist and have melting points below that of MoB which is 2450°K . Hence, this third phase is most probably a mixture of Mo_2B , Mo_3B_2 , and other molybdenum rich borides.

Because of the tendency of boron nitride to combine chemically with other materials at high temperatures to form alloys other insulators were examined as a possible substitute for boron nitride. Almost all of the alternate insulators considered suffered from either a loss of mechanical properties or a loss of insulator characteristics at elevated temperatures.

One of the more promising materials tested was beryllium oxide, BeO . A typical test of this material consisted of heating a BeO rod in contact with a molybdenum plate in a vacuum atmosphere. The rod and plate were first heated to 1550°C and held for two hours in a vacuum of 7×10^{-5} mm Hg. At the conclusion of this test, the BeO rod diameter and weight were unchanged. Also, no visible reaction had occurred between the BeO and molybdenum. However, the BeO and molybdenum sample was next heated to 1900°C for two hours in a vacuum of 2×10^{-4} mm Hg. After the test, the BeO diameter had decreased from 0.128 inch to 0.120-0.123 inch. A weight loss of 0.06 gram was measured, which is a loss of 15 percent from the original weight. No detectable reaction occurred between the BeO and molybdenum. Based on these tests, it appears that BeO and molybdenum are compatible to 1900°C . However, the weight loss of 15 percent in two hours eliminated beryllium oxide as a possible substitute for boron nitride in the resistojet.

References

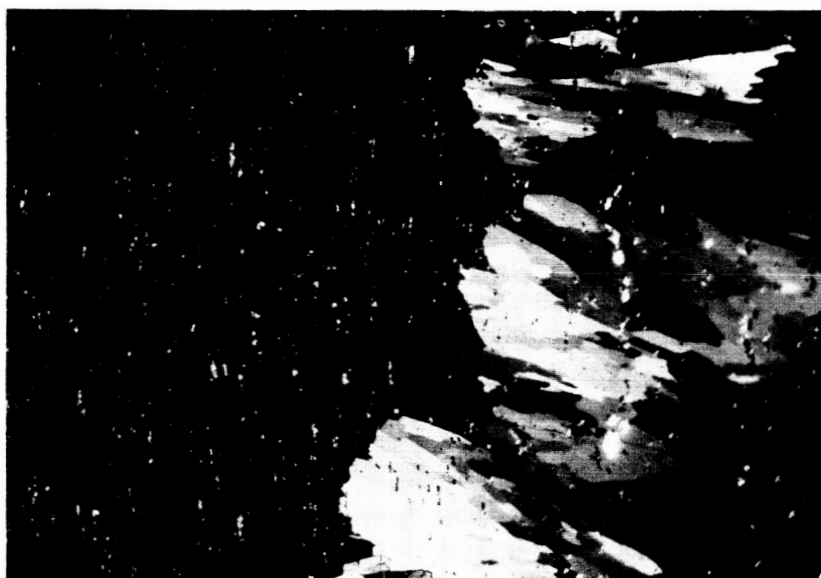
- B-1. Hansen, M., Constitution of Binary Alloys, McGraw-Hill, New York, p. 264 (1958).
- B-2. Mott, B. W., Micro-Identification Hardness Testing, Butterworths Scientific Publications, London, p. 239 and p. 250 (1956).
- B-3. English, J. J., DMIC Report 152, p. 33 (29 April 1961).



P3420B

(A)

250X



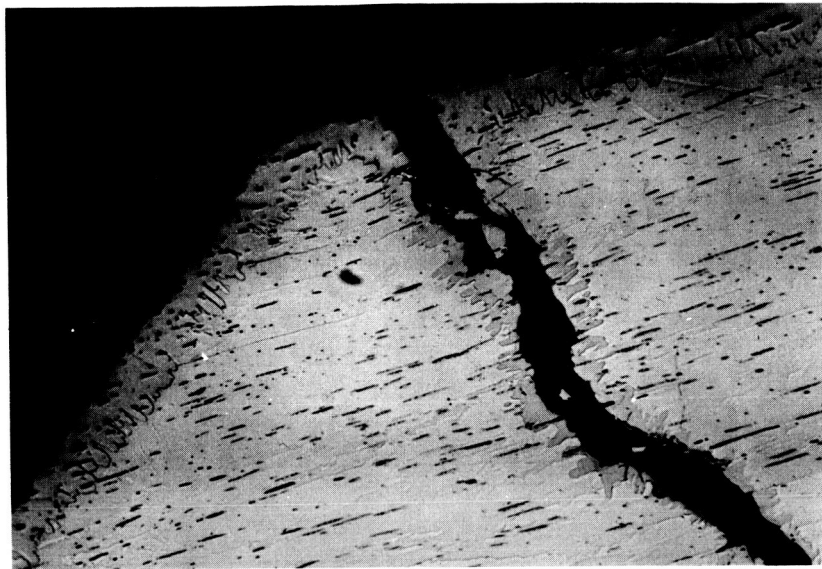
P3420C

(B)

250X

64-3743

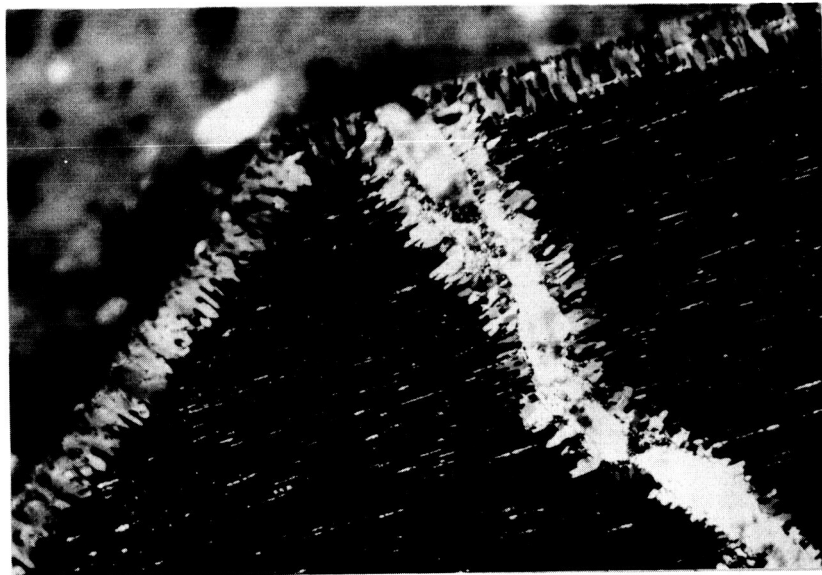
Figure B-2 DISTORTED PORTION OF TUNGSTEN SUPPORT PIN, SHOWING TUNGSTEN BORIDE



P 3420

(A)

250X



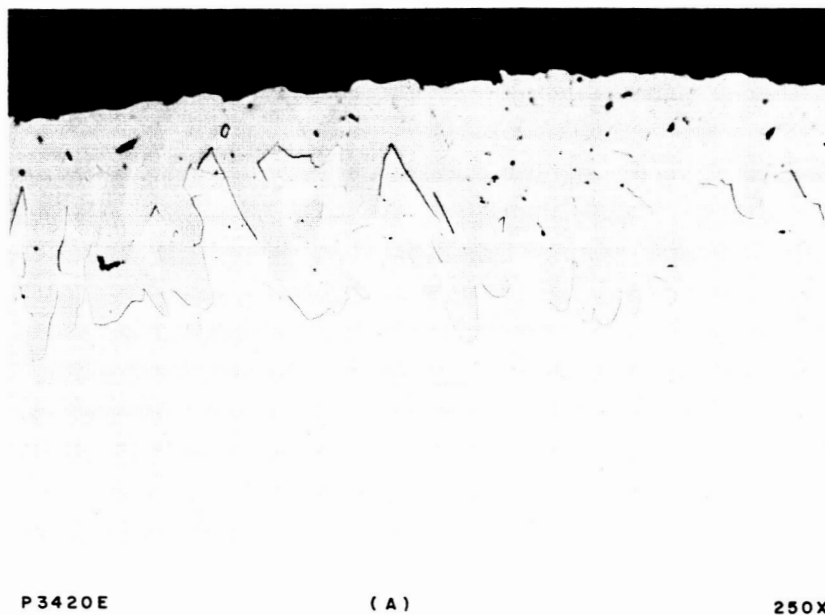
P 3420A

(B)

250 X

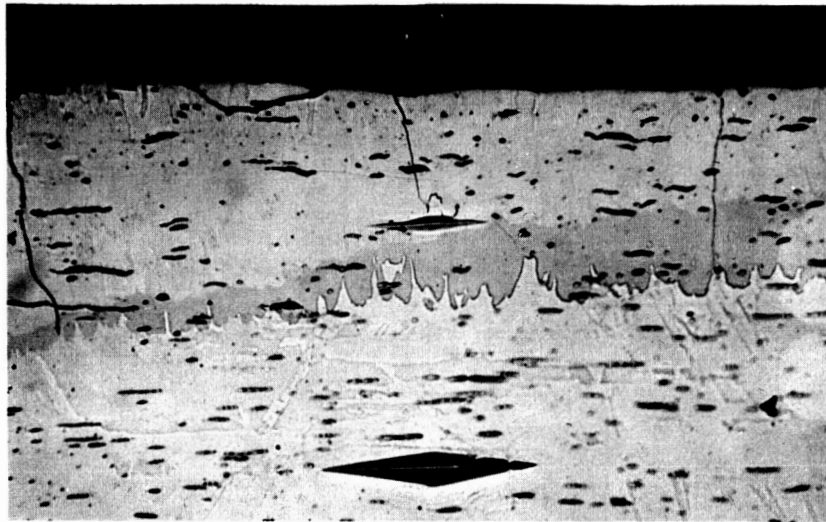
64-3744

Figure B-3 CRACK FORMING IN TUNGSTEN SUPPORT PIN SHOWING TUNGSTEN BORIDE



64-3745

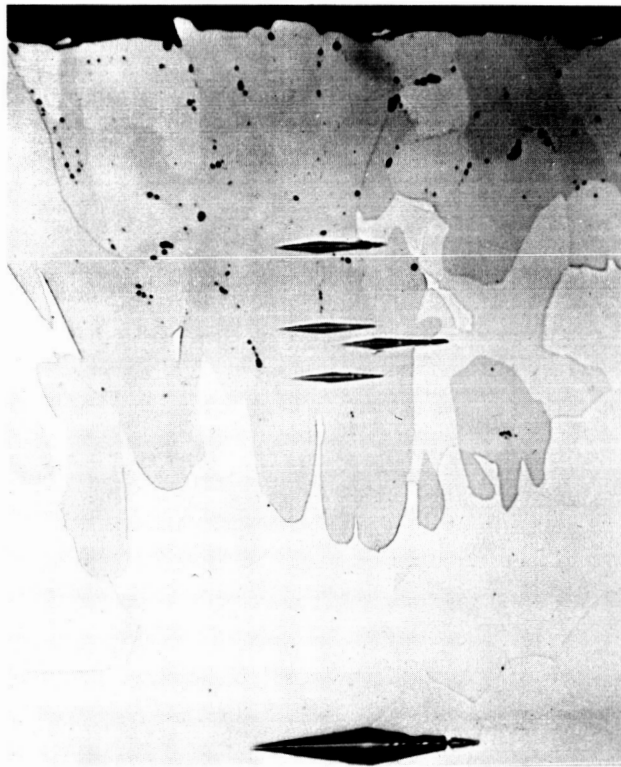
Figure B-4 WIRE MICROSTRUCTURE SHOWING PRESENCE OF TUNGSTEN BORIDE



P 3420 D

(A)

500X



P 3420 G

(B)

500X

64-3746

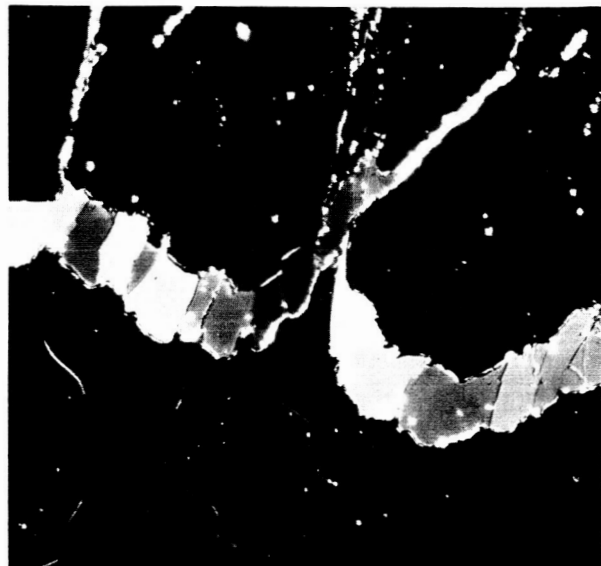
Figure B-5 MICROHARDNESS INDENTATIONS IN THE TUNGSTEN AND TUNGSTEN BORIDE PHASES



P3522G

3A

250X



P3522H

3B

250X

Figure B-6 MOLYBDENUM SUPPORT SEGMENT AFTER 293-HOURS

APPENDIX C

TEST SYSTEM AND EXPERIMENTAL ERROR

Measurements of thruster performance were made in an environmental test facility. The thruster is suspended from a pendulum-type, liquid-cooled thrust stand which is in turn suspended rigidly from an environmental tank. The tank is 7 feet long, 2 feet in diameter, and water cooled. The tank is exhausted by a 6,000 cfm pumping system which produces an ambient tank pressure of the order of $1/2$ to 1 mm Hg at ordinary test mass flows. Visual access to the thruster is provided by water cooled glass viewing ports in the tank.

The direct-force-measuring thrust stand is very similar to the one developed on a program in arc-jet propulsion carried out for NASA Lewis Research Center by Avco RAD. The major modification for use on the 2- to 3-kw thruster program was to equip the thrust stand with lighter kovar flexures to secure greater displacements of the thrust stand at the low thrust levels encountered here. The legs used on this program are strips of 0.015-inch kovar. Actual thrust stand displacements corresponding to the thrust levels produced by the 3-kw resistojet are of the order of 0.25 mm. The thrust stand is calibrated with each use, by pulley and string techniques. The liquid cooling is successful in eliminating thermal loading effects. Thrust readings are thought to be accurate to 3 percent.

Power is supplied to the thruster from a Miller welding power supply and measured with precision dc meters; a voltmeter is placed across the wire coil and an ammeter (actually a calibrated shunt and a second voltmeter) is placed in series with the wire coil. The meters which are used are accurate to 1 percent of full scale reading. Since readings are usually made near the $1/2$ scale point, the readings themselves are accurate to about 2 percent. Hence, the measurement of electrical input power is accurate to about 3 percent.

Mass flow is measured with a rotameter type flow gauge. The gauges employed are calibrated by the manufacturer, the Fisher-Porter Co., and are guaranteed by them to be accurate to 1 percent after calibration. A calibration facility developed at Avco RAD is used to check the flowmeter calibrations periodically, and achieves an accuracy of 3 percent. Mass flow measurements quoted here are thought to be accurate to ± 3 percent.

Combining the estimated errors in power, mass flow, and thrust, the following errors are expected in specific impulse and efficiency:

$$I_{sp} = T/\dot{m}$$

$$\Delta I_{sp} \approx \sqrt{(3)^2 + (3)^2} = 4 \text{ to } 5 \text{ percent}$$

$$Eff = \frac{4.8 \times 10^{-5} T^2}{\dot{m} P_{in}}$$

$$\Delta Eff \approx \sqrt{(2 \times 3)^2 + (3)^2 + (3)^2} = 7 \text{ to } 8 \text{ percent}$$

where

I_{sp} = specific impulse, seconds

\dot{m} = propellant mass flow rate, grams/sec

T = thrust, grams

Eff = thrust efficiency, to be multiplied by 100 to yield percentage

P_{in} = input power, kilowatts

Δ = percentage uncertainty in derived quantity

RMS averaging has been used since the errors in thrust, mass flow, and input power are independent. Some confusion naturally arises because of the definition of the percentage error in efficiency, which is itself often quoted as a percentage. The meaning (as used here) of an 8 percent error in efficiency measurement is that the uncertainty is 0.08 of the measured value; hence, a measured efficiency of 70 percent with an accuracy of 8 percent means

$$Eff = 70 \pm 0.08 (70) = 70 \pm 5.6 \text{ percent.}$$

APPENDIX D

HEAT TRANSFER

An analysis of the general heat flow patterns within the thruster was performed in order to provide information regarding methods of improving performance. The resistojet was regarded as consisting of three major components: the wire, the gas, and the thruster body. The following calculations show the approximate magnitude of the three transfer couplings between these three components; that is, wire to gas (convection), gas to body (convection), and wire to body (radiation), as well as the magnitude of both the axial and radial wire temperature gradients.

1. Wire-Gas Coupling

The primary mechanism by which the gas is heated is convection from the hot heater coil. It can be demonstrated that the coil does in fact have sufficient surface area to transfer all of its heat input to the gas by convection.

For gas flowing normal to a heated cylinder, the film coefficient, h , for heat transfer can be given by an expression of the form^{D-1}

$$\frac{hd}{k} = f \left(\frac{Gd}{\mu} \right)^n \quad (D-1)$$

where

h = film coefficient, watts/cm²-°K

d = cylinder or wire diameter, cm

k = thermal conductivity, watts/cm-°K

G = local mass flux, gm/cm²-sec

μ = viscosity, gm/sec-cm

Consider a typical thruster operating at 3 kw of power and a hydrogen flow rate of 6.3×10^{-2} grams/sec. The mean mass flux through the engine is $(6.3 \times 10^{-2} \text{ grams/sec}) / (0.64 \text{ cm}^2) \approx 10^{-1}$ grams/cm²-sec. The Reynolds number Gd/μ , based on a 30-mil wire diameter evaluated at 2000°K, is approximately $(10^{-1} \text{ grams/cm}^2\text{-sec}) (7.62 \times 10^{-2} \text{ cm}) / (3 \times 10^{-4} \text{ grams/cm-sec}) \approx 25$. From McAdams,^{D-1} for $Gd/\mu = 25$, the Nusselt number, $hd/k \approx 2.5$. Therefore, assuming the gas is at a mean temperature of 2000°K, the thermal conductivity of hydrogen is 10×10^{-5} watts/cm-°K, and the film coefficient h becomes $h = 2.5 k/d = (2.5) (10 \times 10^{-5} \text{ watts/cm-°K}) / (7.62 \times 10^{-2} \text{ cm}) \approx 0.33 \text{ watts/cm}^2\text{-°K}$.

The surface area of the heater element is denoted by $l \pi d = (45 \text{ cm}) (3.14) (7.62 \times 10^{-2} \text{ cm}) = 10.7 \text{ cm}^2$. Therefore, the total heat transfer coefficient for the wire is $(10.7 \text{ cm}^2) (0.33 \text{ watts/cm}^2\text{-}^\circ\text{K}) = 3.52 \text{ watts/}^\circ\text{K}$. Assuming that the mean temperature difference between the wire and the gas is 1000°K , there is sufficient forced convection to transfer 3 kw of power from the heater element to the hydrogen. It is clear that a portion of the energy flux from the wire radiates to the inner chamber wall where convection between the wall and the gas also forms a good energy transfer mode. The previous calculation serves to show the availability of sufficient energy transfer between the heater element and the incoming hydrogen gas.

2. Gas-Thruster Body Coupling

The gas heated by the tungsten coil is then exhausted by passing it through a sonic throat and expanding it to an area ratio of 30. During its passage through the exhaust nozzle, the hot gas transfers heat to the nozzle surface by convection. The heat flux to the throat of a sonic nozzle may be written^{D-2} as

$$q_c = C_H \rho u h \quad (\text{D-2})$$

$$C_H = 0.023 / \text{Pr}^{0.6} \text{Re}^{0.2} \quad (\text{D-3})$$

$$\text{Re} = \frac{\rho u D^*}{\mu} \quad (\text{D-4})$$

where

q_c = throat heat flux

C_H = Stanton number

ρu = mass flux

h = local enthalpy

Pr = Prandtl number

Re = Reynolds number

D^* = throat diameter

μ = viscosity

For the particular nozzle being considered, $D^* = 0.060 \text{ inch} = 0.152 \text{ cm}$ and $A^* = \pi D^{*2} / 4 = (3.14) (0.152)^2 / 4 = 1.82 \times 10^{-2} \text{ cm}^2$. The mass flux, ρu , is then $\rho u = \dot{m} / A^* = (6.3 \times 10^{-2} \text{ grams/sec}) (1.82 \times 10^{-2} \text{ cm}^2) = 3.46$

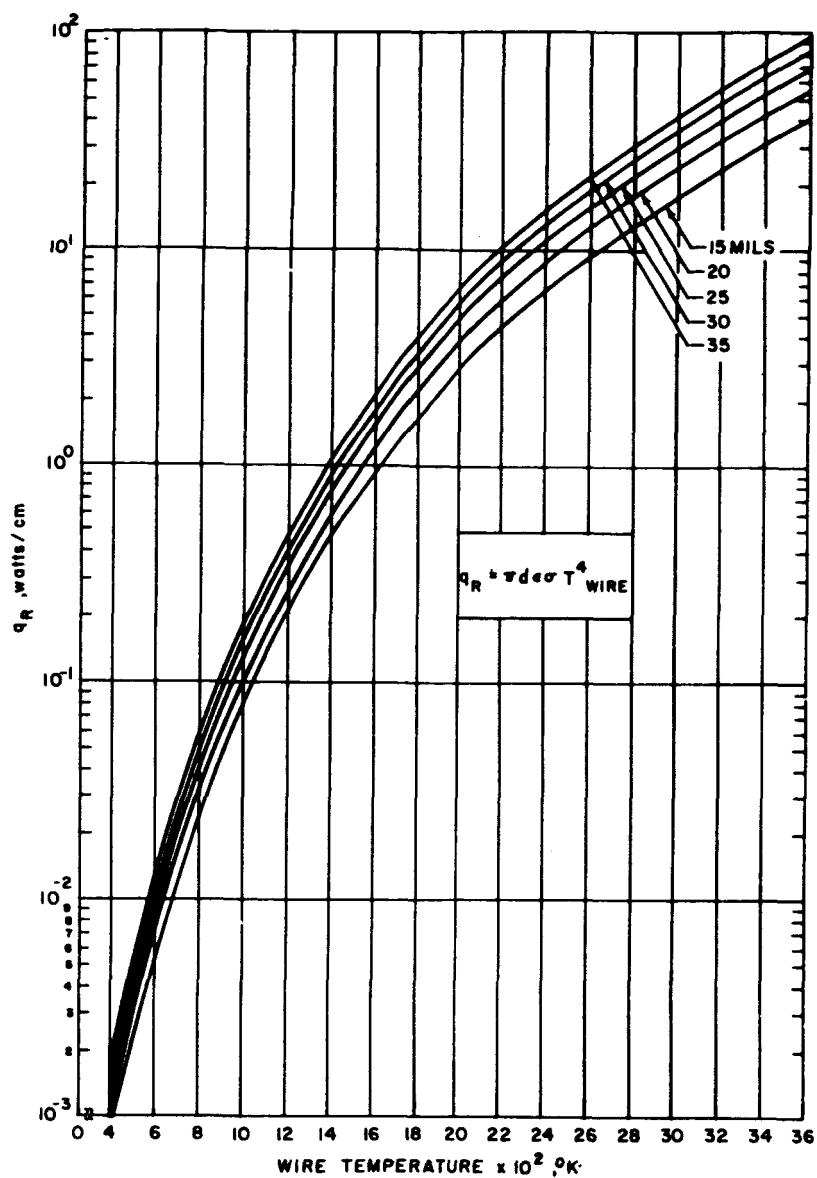
grams/cm²-sec. For hydrogen at 2000°K, the Prandtl number is approximately 0.65 and the viscosity $\mu = 0.32 \times 10^{-3}$ poise. Therefore, $Pr^{0.6} = (0.65)^{0.6} = 0.77$, $Re = (3.46 \text{ grams/cm}^2\text{-sec}) (0.152 \text{ cm}) / (0.32 \times 10^{-3} \text{ grams/cm-sec}) = 1.64 \times 10^3$, and $Re^{0.2} = (1.64 \times 10^3)^{0.2} = 4.54$. The Stanton number therefore becomes $Ch = (0.023 / (0.77) (4.54) (6.6 \times 10^{-3}))$. For a stagnation enthalpy, h_o , of 2×10^4 Btu/lb and a throat velocity of 1.1×10^4 ft/sec, the throat static enthalpy is given by $h_o - u^2/2 = (2 \times 10^4 \text{ Btu/lb}) - (1.1 \times 10^4 \text{ ft/sec})^2 / 2 (32.2 \text{ ft/sec}^2) \times (778 \text{ ft lb/Btu}) = 1.76 \times 10^4 \text{ Btu/lb} = 10^4 \text{ cal/gram}$. The throat heat flux then becomes $q_c = (6.6 \times 10^{-3}) (3.46 \text{ grams/cm}^2\text{-sec}) \times (10^4 \text{ cal/gram}) (4.18 \text{ joules/cal}) (10^{-3}) = 0.96 \text{ kw/cm}^2$. For the hypothetical case where the entire nozzle has a constant diameter (the throat diameter) the affected surface area is $\pi D^* l = (3.14) (0.152 \text{ cm}) (2.2 \text{ cm}) = 1.05 \text{ cm}^2$. The heat flux lost to the nozzle is then $(0.96 \text{ kw/cm}^2 \times 1.05 \text{ cm}^2) \approx 1 \text{ kw}$.

In actuality, the throat surface area that is affected by the heat flux of 0.96 kw/cm^2 is approximately $\pi D^* l = (3.14) (0.152 \text{ cm}) (0.3 \text{ cm}) = 0.143 \text{ cm}^2$. Hence, the power lost by convection at the throat is $(0.96 \text{ kw/cm}^2) (0.143 \text{ cm}^2) \approx 140 \text{ watts}$. As a first order approximation, the average heat transfer coefficient for the divergent section of a nozzle with an area ratio of 30 can be taken as one fourth that at the throat. For the divergent portion, consider the average diameter to be, $D_{avg} = 0.5 \text{ cm}$ and the length to be, $l = 1.3 \text{ cm}$. The total affected surface area is then $\pi D_{avg} l = (3.14) (0.5) (1.3) = 2.04 \text{ cm}^2$. Hence, the power lost by convection to the divergent section of the nozzle is $q \approx (0.25) (0.96 \text{ kw/cm}^2) (2.04 \text{ cm}^2) \approx 0.5 \text{ kw}$. (It should be noted that these estimates are approximate and the results may be accurate only to a factor of two or three). One factor which must be taken into consideration is that the actual driving enthalpy difference appears in equation (D-2) rather than just the static enthalpy.

3. Wire-Thruster Body Coupling

Although the primary source of energy transfer to the gas appears to be convection between the wire and the gas, a certain portion of the total input power to the heater is radiated to the inner chamber wall. The total tungsten radiation is shown in figure D-1 for various wire sizes as a function of temperature. Because of the fourth power temperature dependence, radiation from the heater element can be significant. For example, for a 30-mil diameter, 45-cm long wire at a temperature of 3000°K along its entire length, the total radiation, from figure D-1 is $(37 \text{ watts/cm}) (45 \text{ cm}) = 1.67 \text{ kw}$, a sizable percentage (55.5 percent) of the total electrical input power. This power is not all lost, since the chamber wall transfers power to gas by reradiation and convection.

Assuming that all of the power radiated by the tungsten heater coil is received by the chamber wall as incident radiation, the wall will reach



63-10375

Figure D-1 TUNGSTEN WIRE RADIATION VERSUS TEMPERATURE FOR DIFFERENT DIAMETERS

a radiative equilibrium temperature due to a balance between this incident radiation and radiation at its own temperature. That is, at equilibrium,

$$q_{IR} = \sigma T_w^4 A \quad (D-5)$$

where

q_{IR} = incident radiation, watts

σ = Stefan-Boltzmann constant = 5.67×10^{-12} watts/cm²-°K⁴

T_w = temperature of chamber wall, °K

A = wall surface area, cm²

Equation (D-5) assumes absorptivity equals emissivity.

The radiative equilibrium temperature for the chamber wall is shown in figure D-2 for different wire temperatures. The assumption has been made for figure D-2 that the radiating wire has a diameter of 30 mils, a length of 45 cm, and a constant wire temperature.

4. Wire Temperature Gradients

Since the gas entering the coil heater area is somewhat cooler than the tungsten coil itself, convective heating of the gas will cool the initial turns of the coil. If the heat flux along the wire is large enough, the cooled portion of the wire will be reheated by the hotter downstream portion, thereby providing a larger surface over which to heat the gas and hence better heater efficiency. Consider a wire 30 mils in diameter and 45 cm in length with a total resistance of 1.04 ohms. If the wire temperature was constant along its length, the temperature would be 3105°K. If a linear variation of resistance per unit length is assumed, the maximum temperature gradient that this wire can support is characterized by a temperature at the downstream end of the wire of 3650°K, the melting point of tungsten. At this temperature, the resistance per unit length $R/l = 2.71 \times 10^{-2}$ ohms/cm. The resistance per unit length at the upstream end is therefore $(R/l)_{up} = 1.91 \times 10^{-2}$ ohms/cm, which corresponds to a temperature at the upstream end of 2710°K. The temperature gradient in the wire is then $dT/dx = (3650-2710)^\circ\text{K}/45\text{ cm} = 20.9^\circ\text{K/cm}$. The heat flux associated with this gradient is

$$q_A = kA \frac{dT}{dx} \quad (D-6)$$

where

q_A = axial heat flux, watts

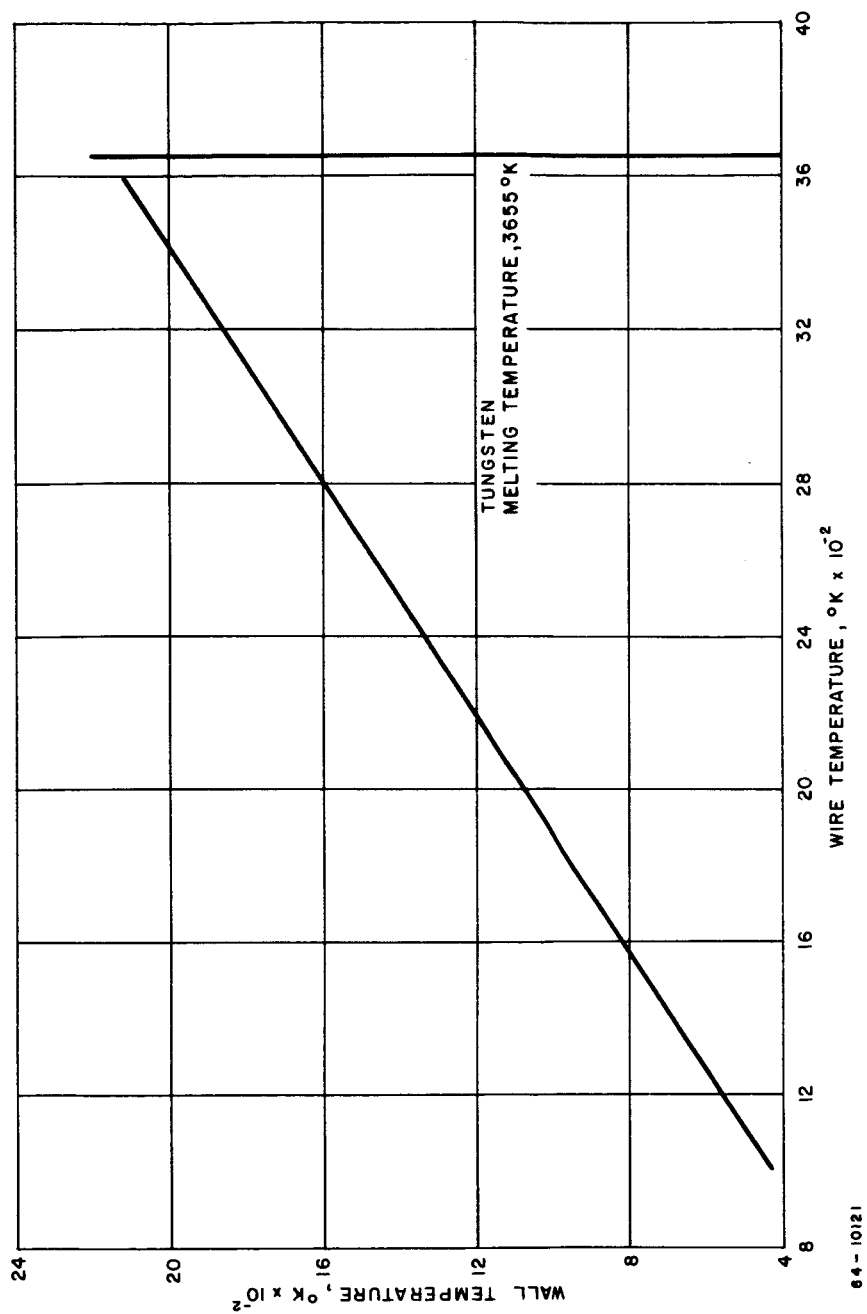


Figure D-2 EQUILIBRIUM INNER CHAMBER WALL TEMPERATURE FOR VARIOUS WIRE TEMPERATURES

k = thermal conductivity, watts/cm-°K

A = wire area, cm²

dT/dx = temperature gradient, °K/cm

For this particular gradient, $q_A = (0.81) (45.6 \times 10^{-4}) (20.9) = 0.077$ watts. This heat flux is negligible compared to the flow of heat from the wire to the gas, and so does not provide a means of relaxing this temperature gradient. The envelope of all possible linear temperature gradient is shown in figure D-3.

The only other mechanism by which the heat lost by the upstream portion of the wire can be resupplied is joule heating. However, since resistivity decreases with a decrease in temperature, the cooled portion of the wire absorb an even smaller amount of the total I^2R input to the heater element.

The transverse temperature gradient through the tungsten wire was investigated to determine whether internal melting of the heater element posed a serious problem. For pure radial conduction of heat produced in a current carrying cylinder, the temperature may be written as D-3.

$$T = T_o - \frac{r^2}{4} \frac{I^2}{k\sigma}$$

or

(D-7)

$$\Delta T = \frac{r^2}{4} \frac{I^2}{k\sigma}$$

where

ΔT = temperature difference, °K

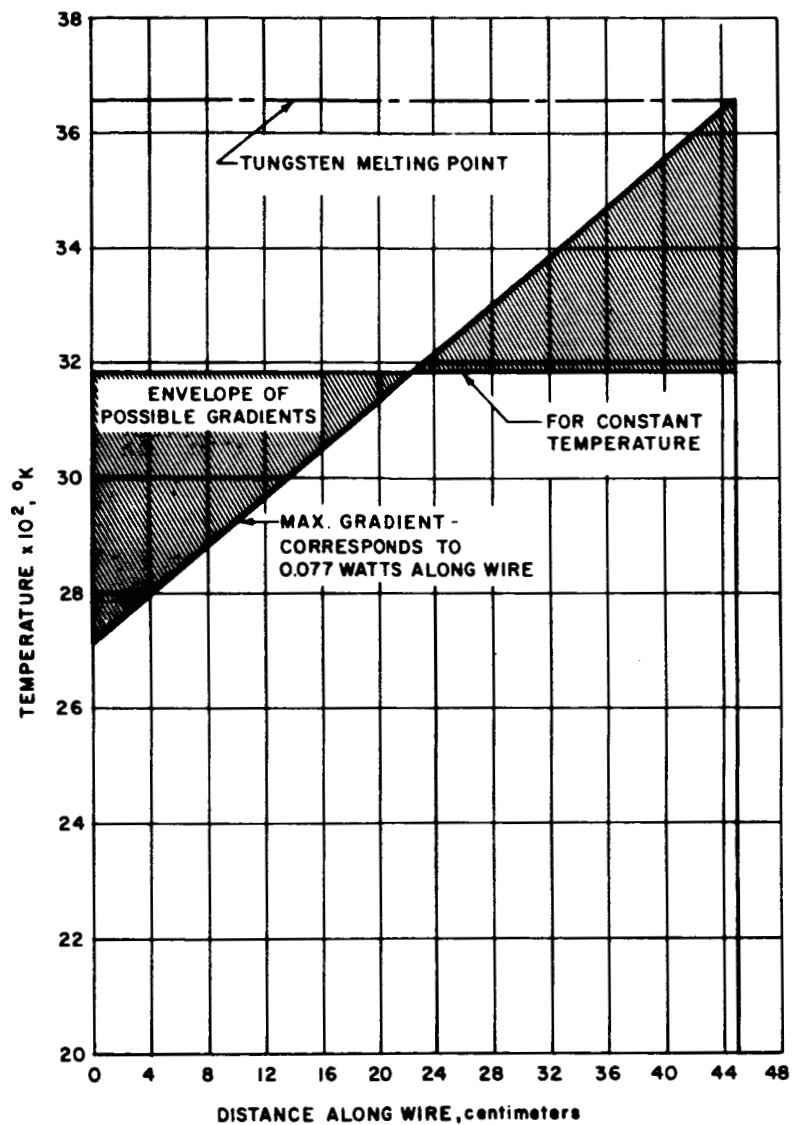
r = radius, cm

I = current per unit area, amps/cm²

k = thermal conductivity, watts/cm-°K

σ = electrical conductivity, ohms/cm.

Assuming initially that the outer surface temperature is 3400°K, the thermal conductivity at this temperature is 0.80 watts/cm-°K and the electrical conductivity is 8.78×10^3 mhos/cm. Since the current necessary to maintain a 30-mil diameter wire at 3400°K is 49 amps and the cross sectional area of this wire is $\pi D^2/4 = (3.14 (7.62 \times 10^{-2} \text{ cm})^2)/4 = 4.56 \times 10^{-3} \text{ cm}^2$, the current per unit area, $I = 49 \text{ amps} / (4.56 \times 10^{-3} \text{ cm}^2) = 1.07 \times 10^4 \text{ amps/cm}^2$.



63-10378 Figure D-3 LINEAR TEMPERATURE GRADIENTS IN TUNGSTEN WIRE

Therefore, $\Delta T = (3.81 \times 10^{-2} \text{ cm})^2 (1.07 \times 10^4 \text{ amps/cm}^2)^2 / 4 (0.80 \text{ watts/cm} \cdot ^\circ\text{K}) (8.78 \times 10^3 \text{ mhos/cm}) = 5.9 ^\circ\text{K}$. The internal temperature of the wire is therefore approximately $3406 ^\circ\text{K}$. Similarly, if the outer temperature were $3000 ^\circ\text{K}$ or $2600 ^\circ\text{K}$, the gradients would be $3.5 ^\circ\text{K}$ or $1.9 ^\circ\text{K}$ respectively, the different values arising from the lower currents necessary to produce the given temperature and the higher values of thermal and electrical conductivity. For radial temperature gradients of this magnitude the problem of internal wire melting can be neglected.

The preceding calculations led to the following conclusions:

- a. Each of the couplings between the three major components of the resistorjet is capable of transferring a large heat flux. The wire-gas coupling is capable of producing a heat flux by forced convection of the total amount of input power. A heat flux of up to 1 kw can be produced by convection in the nozzle, owing to gas-thruster body coupling. Finally, the wire-thruster body coupling is capable of a radiation heat flux of at least 1 kw. Because of these excellent couplings and the resulting heat paths formed in the engine, it is extremely important to have sufficient regenerative cooling.
- b. The wire temperature gradient in the axial direction is not sufficient to support a significant heat flux along the wire. Therefore, accompanied by the unfavorable variation of resistivity with temperature, the upstream portion of the heater element, being cooled somewhat by the incoming gas, tends to operate at lower temperatures.
- c. The wire temperature gradient in the radial direction is small enough so that internal melting of the tungsten wire heater element need not be considered as a problem area.

References

- D-1. McAdams, W.H., Heat Transmission, McGraw-Hill Book Co., Inc., New York (1954). pp. 258-261.
- D-2. Ibid, p. 219.
- D-3. Carslaw, H.S., and J. C. Jaeger, Conduction of Heat in Solids, Clarendon Press, Oxford (1947). p. 168.

APPENDIX E

NOZZLE DESIGN

Because the length of the heat transfer region in the thruster is so great, it is reasonable to assume that the fluid flow at the nozzle throat is uniform. For this reason, the study of nozzle flow characteristics for the resistojet is particularly amenable to one-dimensional nozzle flow analyses. In order, to determine analytically an optimum nozzle for chamber conditions typical of 3-kw resistojet operation, two approaches were taken. The first was a computer program for a one-dimensional isentropic expansion through an ideal nozzle; the second considered one-dimensional isentropic flow through an expansion area which had been reduced by the viscous boundary layer. The second analysis also took into account other nonideal flow characteristics.

1. Ideal One-Dimensional Isentropic Nozzle Flow

a. Computer Program 912C

Program 912C is essentially a one-dimensional program yielding both equilibrium and frozen flow nozzle solutions for a given stagnation pressure and temperature input. The expansion can be made from either a plenum chamber where the velocity is zero or from a nozzle throat where the velocity is equal to the local acoustic speed. The program is valid for any gas with specification of the gas properties; it has been used for hydrogen by writing in the properties of H_2 and H as given in reference E-1.

For a given input of stagnation pressure, stagnation temperature, and area ratio, the program expands down the nozzle, assuming isentropic flow, and gives the flow properties at each point where the static temperature has dropped an additional $100^\circ K$, for both equilibrium and frozen flow. After expanding down to $300^\circ K$, the flow properties for the particular area ratio desired are interpolated between the $100^\circ K$ steps. The flow properties for both equilibrium and frozen flow, printed at each interval of $100^\circ K$ are: static pressure, degree of dissociation, local acoustic speed, velocity, density, area ratio, mach number, length of nozzle required to take the flow to equilibrium, and the recombination rate.

The equations used for the expansion are the standard isentropic expansion equations as found, for example, in reference E-2. For the frozen case, the value of gamma, the ratio of specific heats, is calculated at the stagnation conditions and then considered to be a constant throughout the entire expansion. For the case of equilibrium flow, the value of gamma at the stagnation conditions is assumed to be

constant only for an expansion until the static temperature has dropped 100°K. At this point, the value of gamma is recalculated based on the local conditions and the expansion is continued for another 100°K drop. This is done until a static temperature of 300°K is reached.

The properties which are printed out are combined in the following ways to produce important performance parameters (nomenclature common to the computer program has been used):

- 1) Equilibrium specific impulse, $I_{sp\text{equil}}$ is defined as the exit velocity divided by the acceleration due to gravity

$$I_{sp\text{equil}} = \frac{U_{ex}}{g_0} \quad (E-1)$$

- 2) Actual equilibrium specific impulse, $I_{sp, \text{act, equil}}$, is defined as the thrust divided by the weight flow of fuel.

$$\begin{aligned} T &= \dot{m}U_{ex} + (P_{ex} - P_{amb}) A_{ex} \\ &= \rho UA U_{ex} + (P_{ex} - P_{amb}) A_{ex} \end{aligned}$$

and there

$$I_{sp, \text{act, equil}} = \frac{T}{\rho UA} = \frac{U_{ex}}{32.2} + 2116 \frac{(P_{ex} - P_{amb})}{\rho^* U^*} \frac{A_{ex}}{A^*} \quad (E-2)$$

where

U_{ex} = exhaust velocity, ft/sec

P_{ex} = exhaust pressure, atm

P_{amb} = ambient pressure, atm

A_{ex}/A^* = area ratio

ρ^* = throat density, lb/ft³

U^* = throat velocity, ft/sec

- 3) Actual frozen specific impulse, $I_{sp, \text{act, froz}}$, is defined in precisely the same way as $I_{sp, \text{act, equil}}$, except that exhaust velocity and exhaust pressure are for the frozen flow case.

4) The equilibrium expansion efficiency, MU-EXP, equil, is a measure of the equilibrium exhaust velocity compared to the ideal exhaust velocity.

$$\text{MU-EXP, equil} = \left(\frac{U_{\text{ex, equil}}}{U_e} \right)^2 \quad (\text{E-3})$$

where

$$U_e^2 = 2 h_o$$

$$h_o = \text{stagnation enthalpy}$$

5) The frozen expansion efficiency, MU-EXP, FROZ, is similarly a comparison of the frozen exhaust velocity and the ideal exhaust velocity.

$$\text{MU-EXP, FROZ} = \left(\frac{U_{\text{ex, FROZ}}}{U_e'} \right)^2 \quad (\text{E-4})$$

where

$$(U_e')^2 = 2 h_o \epsilon_f$$

$$\epsilon_f = \text{frozen flow efficiency}$$

6) The frozen flow efficiency, MU-FROZ or ϵ_f , is defined as the power available for thrust compared to the power put into the gas. It is essentially a measure of the power that has gone into dissociating the gas.

Note that the above expansion efficiencies are a comparison of the actual exhaust velocities to the ideal exhaust velocities. A second expansion efficiency can be defined as follows:

7) The actual equilibrium expansion efficiency,

$$\text{EXP EFF, ACT, EQUIL} = g_o^2 \frac{(\text{ISP, TEST, EQUIL})^2}{2 h_o}$$

where ISP, TEST, EQUIL = ISP, ACT, EQUIL at the desired area ratio. Evaluating the constant, the expression becomes

$$\text{EXP EFF, ACT, EQUIL} = 2.07 (10^{-2}) \frac{(\text{ISP, TEST, EQUIL})^2}{h_o} \quad (\text{E-5})$$

where h_o is given in Btu/lb.

8) Similarly, an actual frozen expansion efficiency can be defined

$$\text{EXP, EFF, ACT, FROZEN} = 2.07 (10^{-2}) \frac{(\text{ISP, TEST, FROZ})^2}{c_f h_o} \quad (\text{E-6})$$

where ISP , TEST , FROZ = ISP , ACT , FROZ at the desired area ratio.

9) The overall efficiency may now be defined

$$\text{OVERALL EFF, FROZ} = (\text{EXP, EFF, ACT, FROZ}) \times (\text{MU-FROZ}) \text{ PLENUM}$$

(Note the assumption of freezing at the plenum chamber conditions). It should be observed that for the equilibrium case, OVERALL EFF , EQUIL = EXP EFF, ACT , EQUIL . This is because the frozen flow efficiency, MU-FROZ, is one for equilibrium flow.

The values of test specific impulse, actual expansion efficiencies, and overall efficiencies are all calculated considering a specific ambient pressure. Each of these quantities is calculated also for the case of a zero ambient pressure, i. e. , a ratio of chamber pressure to ambient pressure of infinity. These values are denoted by the additional subscript INF signifying infinite pressure ratio.

b. Program Results

The preceding one-dimensional computer program yielded the primary result that improved thruster performance could be attained by (1) increasing the chamber or stagnation pressure, and (2) increasing the area ratio. These results were obtained from figures and overall efficiency for frozen flow of hydrogen when chamber pressure and area ratio were varied. In figure E-1 overall efficiency represents only frozen flow efficiency and nozzle efficiency, because the inputs to the computer program were a stagnation pressure and temperature at which to start the expansion. These values of pressure and temperature are what would result from the passage of the gas through the heater element area upstream of the nozzle. Therefore, heater efficiency is not pertinent. It should be noted in figure E-1 that when the area ratio goes to infinity, the nozzle efficiency goes to one. However, the overall efficiency will go only to the frozen flow efficiency because the energy that goes into dissociation is not recovered by a recombination process within the nozzle. It should be emphasized that because this program did not consider the viscous boundary layer, all area ratios in these graphs are geometric area ratios.

A more interesting way of examining the increased overall efficiency and specific impulse associated with a constantly increasing area ratio

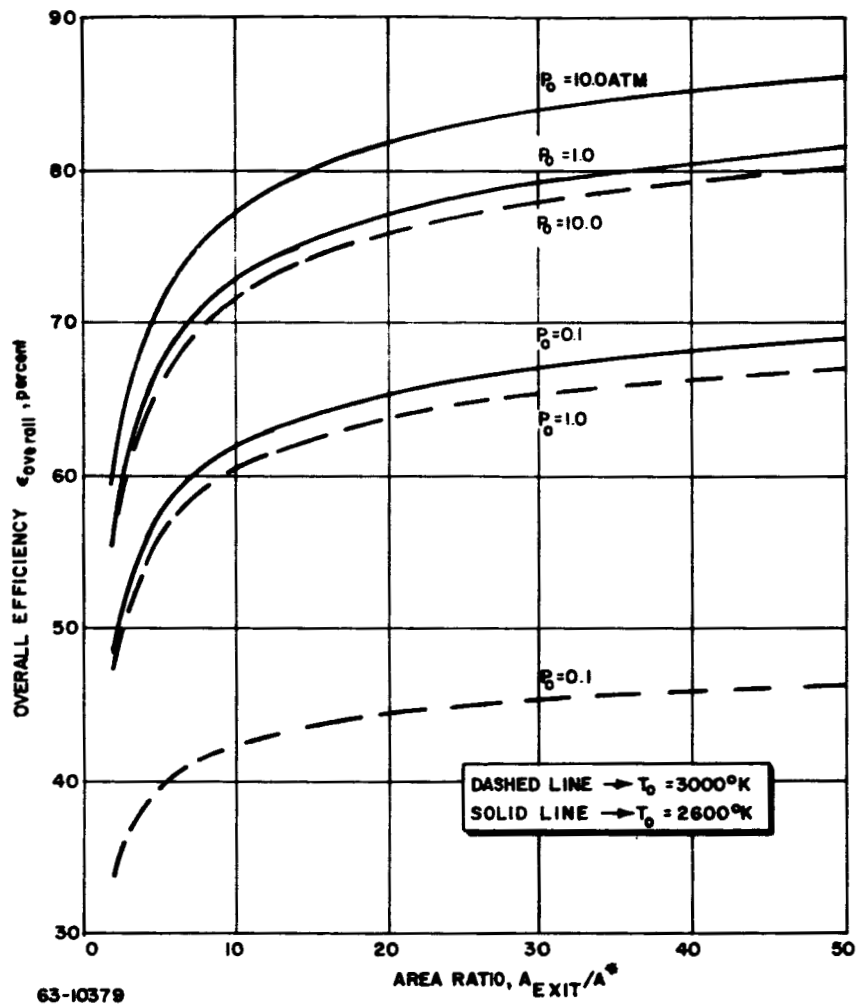


Figure E-1 FROZEN OVERALL EFFICIENCY AS A FUNCTION OF AREA RATIO, HYDROGEN

is shown in figures E-4 and E-5 respectively. In these two graphs, the rate of change of these performance parameters are plotted against area ratio. Although the magnitude of overall frozen specific impulse will change with variations in chamber pressure and temperature, the rates of change of these two variables with area ratio do not vary significantly as can be seen from figures E-1 and E-2. Figures E-4 and E-5 are therefore plotted for only one stagnation temperature and pressure. In analyzing these two figures, it should be first noted that as area ratio goes to infinity for given chamber conditions, overall efficiency and specific impulse continue to increase. This is due to the increase in exhaust velocity with area ratio. The exhaust velocity increase, however, is not linear with area ratio as shown in figure E-6, so that for large area ratio, a given small change in area ratio produces a much smaller change in overall efficiency and specific impulse than would be produced by the same small change in area ratio at a lower absolute value of area ratio. To illustrate, an area ratio increase from 10 to 30 produces an increase in overall frozen efficiency (see figure E-1) of almost 6 percent and an increase in frozen specific impulse (see figure E-2) of greater than 30 seconds. However, an area ratio increase from 30 to 50 produces an overall efficiency change of only about 2 percent and a specific impulse increase of about 10 seconds. Similarly, performance increases although slight, can be shown to exist for each area ratio increase up to an infinite area ratio. The conclusion can be drawn then that on the basis of isentropic one-dimensional inviscid flow through an ideal nozzle, performance monotonically increases with increasing area ratio. The fact remains, however, that no physically realizable situation can be ideal. Departures from ideality should be examined to determine how they affect the nozzle flow which in turn will affect performance. This seems especially important in this case where very small changes in performance are of prime consideration.

2. Nonideal One-Dimensional Isentropic Nozzle Flow

Isentropic equilibrium flow of a perfect fluid through an ideal nozzle represents the most efficient method of changing random thermal energy into directed kinetic energy. It also represents a situation impossible to achieve. Therefore, pertinent deviations from this idealized state should be incorporated into any analysis which evaluates performance of a given thruster configuration. These deviations arise in the following ways.

- a. Spatial nonuniformities in the nozzle flow properties cause the one-dimensional analysis to break down due to the nonuniform momentum distribution in the exhaust. This nonuniform momentum distribution contains a greater flux of kinetic energy than does an equal amount of momentum distributed uniformly. Therefore, for a given amount of available energy, a nonuniform momentum distribution represents a loss of thrust.

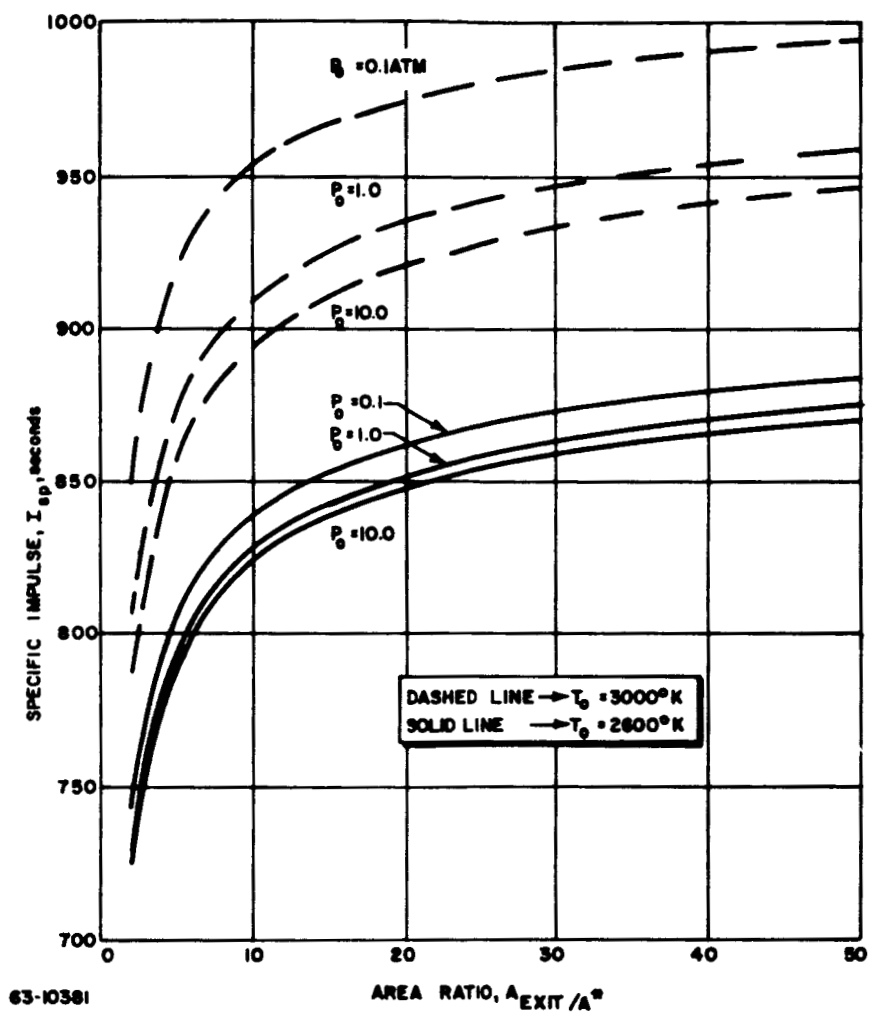


Figure E-2 FROZEN SPECIFIC IMPULSE AS A FUNCTION OF AREA RATIO, HYDROGEN

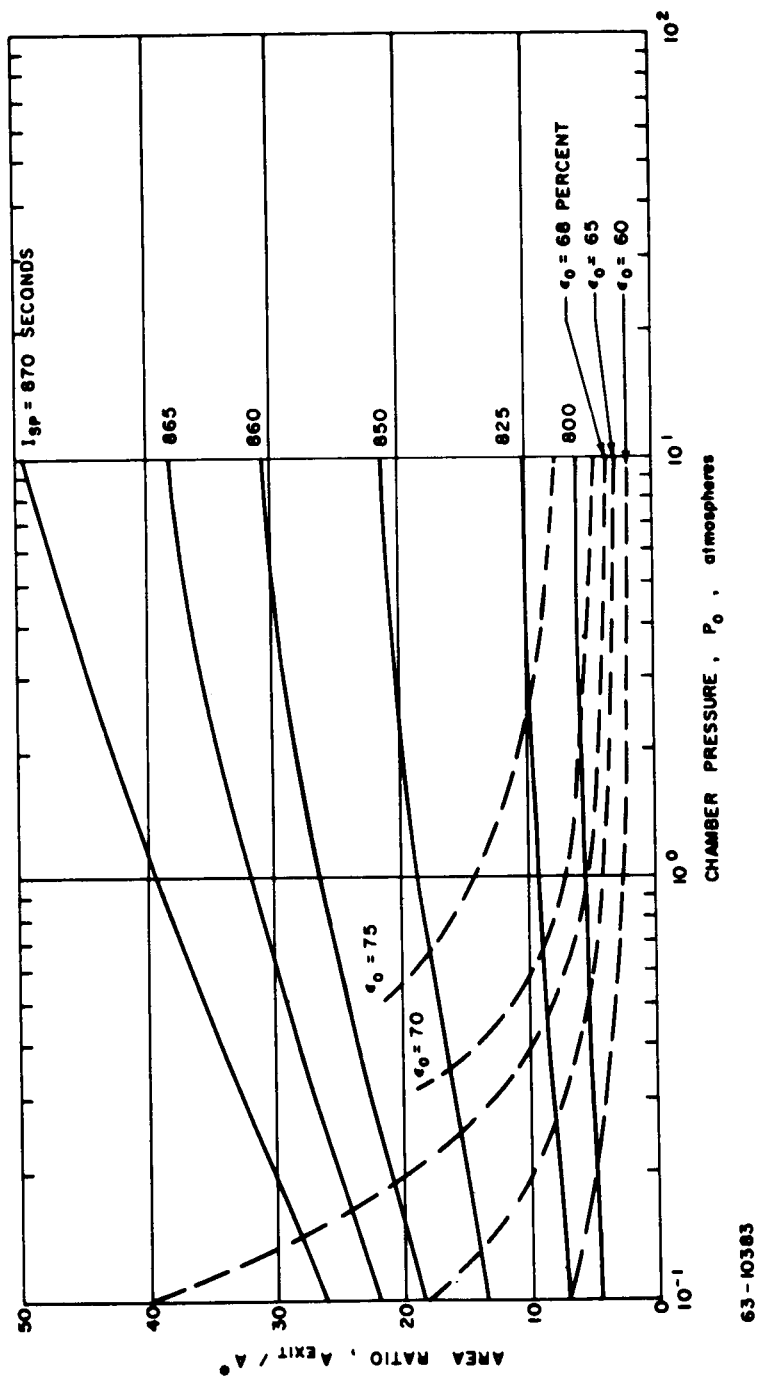
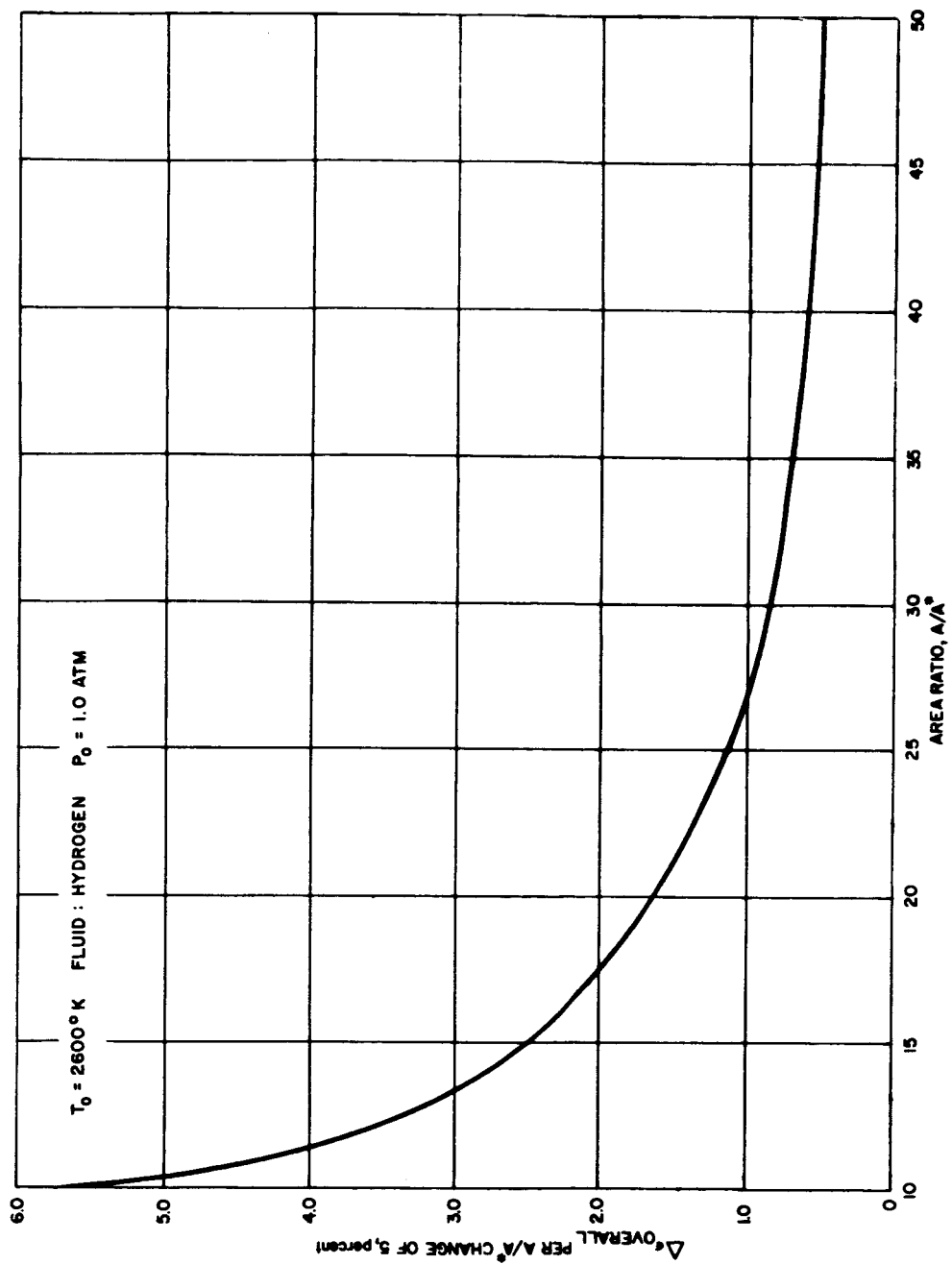


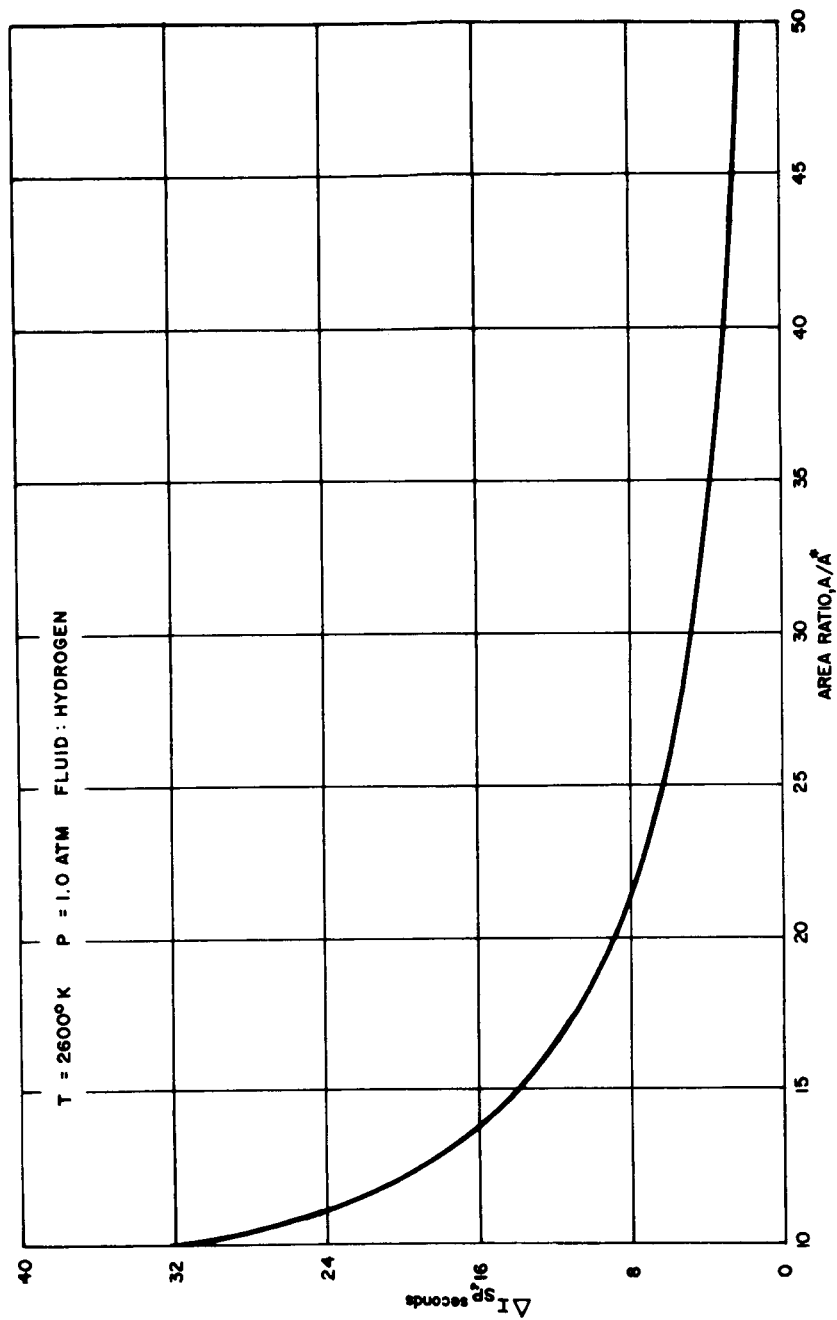
Figure E-3 OPERATING ENVELOPE FOR FROZEN HYDROGEN FLOW, $T_0 = 2600^\circ K$

63-10383



64-786

Figure E-4 OVERALL EFFICIENCY INCREASE WITH AREA RATIO, HYDROGEN



64-787

Figure E-5 FROZEN SPECIFIC IMPULSE INCREASE WITH AREA RATIO, HYDROGEN

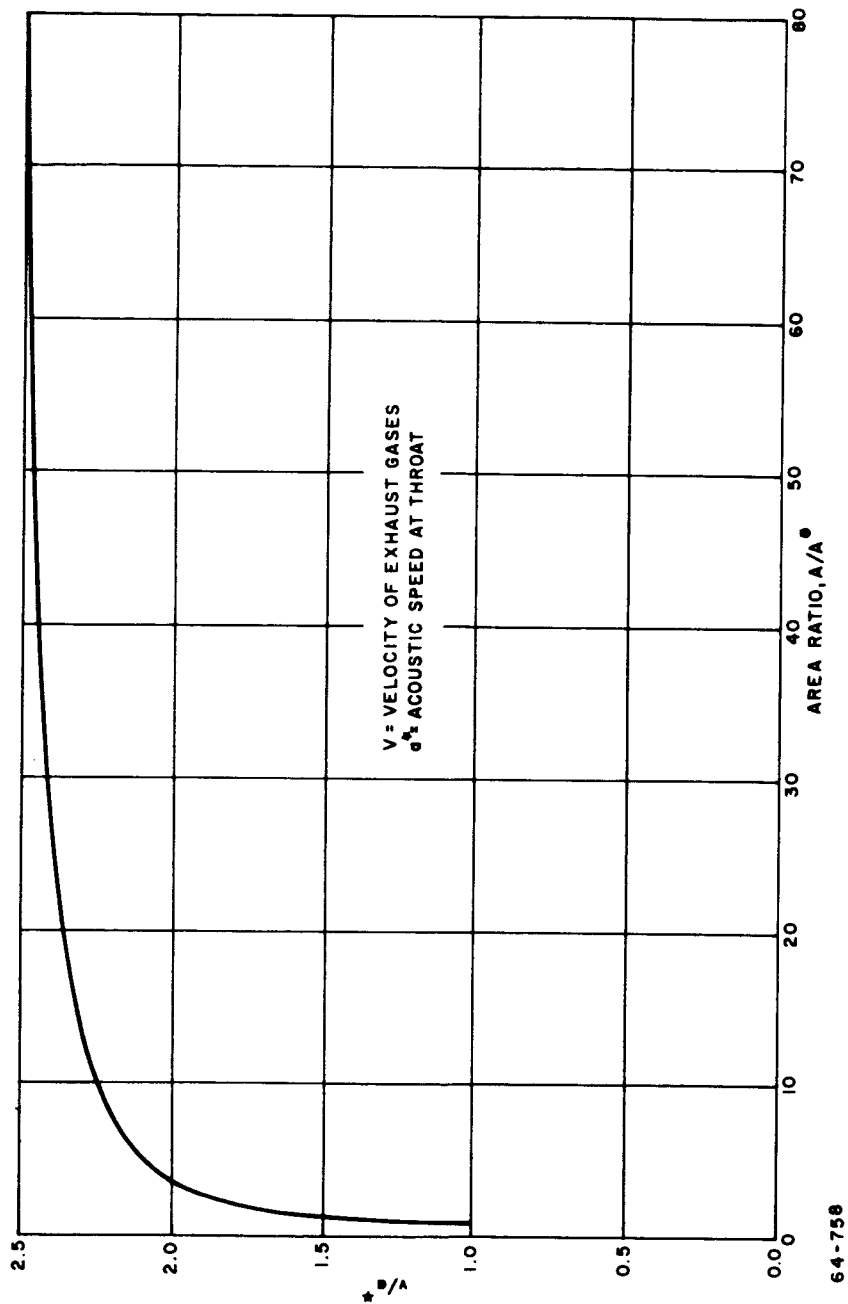


Figure E-6 RATIO OF EXHAUST VELOCITY TO THROAT ACOUSTIC SPEED AS A FUNCTION OF AREA RATIO

c. The equilibrium flow analysis will be invalid when the residence time of an element of fluid in the nozzle becomes negligible compared to the characteristic time associated with the recombination process (assuming the chamber temperature and pressure are such that dissociation and/or ionization will take place). When this is the case, the energy that goes into dissociation and/or ionization remains bound within the propellant and is not available for conversion to directed kinetic energy.

d. The one-dimensional assumption is also affected by the fact that in an actual nozzle the propellant does not all leave the nozzle in an axial direction. This radial component of velocity is of no value for producing thrust.

e. The viscous dissipation of energy affects the calculations made assuming isentropic flow of a perfect fluid in two ways. First, a viscous shearing stress acting on the walls of the nozzle produces a friction drag. Second, the associated boundary layer displacement thickness serves to reduce the geometric area ratio through which the flow expands.

f. Incomplete expansion is a loss associated with both an idealized flow and one considering real nozzle effects. Essentially, it is the loss caused by not expanding the flow to an area ratio of infinity.

To incorporate all of these nonideal effects into an analysis would be a very complex procedure. However, with the following assumptions, the performance of a nonideal nozzle can be evaluated.

- 1) There is no heat transfer to the nozzle walls.
- 2) The flow is one-dimensional, a reasonable assumption considering the very large heat transfer area upstream of the nozzle.
- 3) Outside the nozzle boundary layer, the flow is isentropic.
- 4) The nozzle flow is frozen at the plenum chamber conditions.
- 5) Only conical nozzles are considered for the analysis.

It is interesting to note that independent efforts to minimize each of the three losses being considered (viscous drag, incomplete expansion, and directional loss) would not proceed in the same direction. To decrease the losses caused by viscous dissipation, it is desirable to have a minimum of contact area between the expanding propellant and the nozzle walls. As a result, the general shape of the nozzle made to reduce this loss would be short with a large divergence angle. To minimize both the incomplete

expansion and directional losses, the nozzle would have a large area ratio and a low divergence angle, respectively. For the assumed conical nozzle, the steps necessary to minimize these losses (shorten the nozzle, increase the area ratio, decrease the divergence angle) are conflicting and hence suggest that, because of the trade-off between the methods of approach, there is an optimum conical nozzle for given chamber conditions subject to the previously listed restrictive assumptions. It should also be recalled that on the basis of the ideal analysis of the previous section, slight performance improvements can always be gained by increasing the area ratio (figures E-1, E-2, E-4, and E-5). These improvements are eventually offset by both friction loss and directional loss.

a. Optimum Nozzle Calculation Procedure

At the time this analysis was conducted, two different approaches were available to find the optimum conical nozzle.^{E-3, E-4} These two approaches are different in the following ways. First, the EOS report uses an expression for shear in which the Reynolds number dependence is $(Re)^{-0.5}$, a laminar flow relation. The Neuringer paper uses an expression for shear and boundary layer displacement thickness with Reynolds number dependence of $(Re)^{-0.3}$. This experimental relation was presented by Burke^{E-5} and by Burke and Bird^{E-6} and derived by probing the turbulent boundary layer in the Cornell Aeronautical Laboratory hypersonic conical shock tunnel. Burke characterizes this boundary layer as turbulent with a laminar sublayer. Figure E-7 is a plot of throat Reynolds number as a function of chamber or stagnation pressure. For a chamber pressure of 2.0 atmospheres and a throat diameter of 0.060 inch, the Reynolds number is approximately 1700. Since this is the same order of magnitude as the transition Reynolds number in ordinary pipe flow (≈ 2000), the Neuringer approach appears more satisfactory in this aspect.

The second difference in these approaches occurs when evaluating the friction term. In both papers, this term is a large and complex integral. In the EOS work, numerical and graphical techniques were used on the integral to locate an optimum conical nozzle. Neuringer wrote the integral in terms of Mach number, the ratio of specific heats, γ , and a geometric parameter, then used a computer solution so that the friction term can be evaluated for any particular exit Mach number, specific heat ratio, and geometric parameter. This greatly simplifies the adaptation of this method to any other nozzle analysis which makes the same basic assumptions.

The final difference between the two papers is in their ability to yield a coupled result. The coupling referred to here is the mutual influence of the free stream internal nozzle flow properties and the boundary layer flow properties on each other. That is, the free stream flow

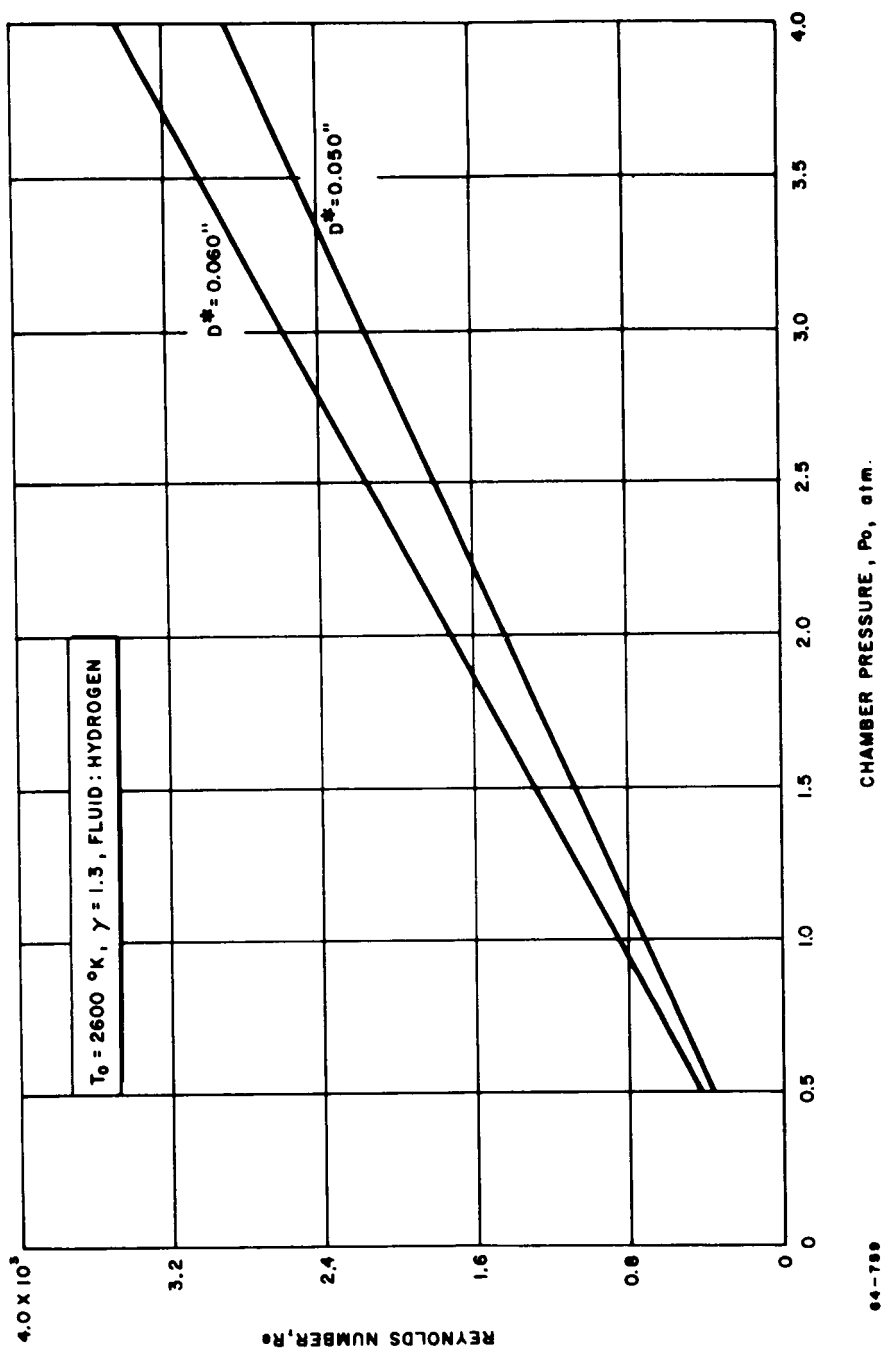


Figure E-7 THROAT REYNOLDS NUMBER VARIATION WITH STAGNATION PRESSURE, HYDROGEN

determines the characteristics of the various parameter profiles in the boundary layer. In turn, the boundary layer displacement thickness associated with these parameter profiles reduces the geometric area ratio to an effective area ratio. The EOS analysis yields a result derived by a strictly uncoupled solution. That is, the area ratios referred to in this analysis are geometric area ratios and the effect of the boundary layer on the expansion area is neglected. In contrast to this and mainly because of the ease with which the friction term can be evaluated, the Neuringer paper can assist in calculating a completely coupled result. Because of this and the more reasonable assumption of the Reynolds number dependence on the boundary layer displacement thickness, the Neuringer paper was used in finding an optimum conical nozzle for the resistojet, within the confines of the assumptions. Briefly, the optimization calculation proceeds as follows:

- 1) For given values of stagnation pressure and temperature, ratio of specific heats γ , and nozzle divergence angle and exit area ratio, and using the isentropic flow tables, find the local static conditions at the nozzle exit.
- 2) Calculate the local reference temperature as used by Burke and Bird:

$$T_R = 0.22 (T_o - T_s) + 0.5 (T_w + T_s) \quad (E-8)$$

where

T_R = reference temperature

T_o = stagnation temperature

T_s = local static temperature

T_w = assumed local wall temperature

- 3) On the basis of this reference temperature, calculate the local reference density ρ_R and viscosity μ_R .
- 4) Calculate the boundary layer displacement thickness at the exit using the Burke and Bird Reynolds number relation:

$$Re_x = \frac{\rho_R U_e x}{\mu_R} ; \frac{\delta^*}{x} = (Re_x)^{-0.3} \quad (E-9)$$

where

- δ^* = boundary layer displacement thickness
- Re_x = Reynolds number based on axial distance
- x = axial distance from nozzle throat to exit plane
- ρ_R = density based on reference temperature
- U_e = propellant velocity at the nozzle exit plane
- μ_R = viscosity based on reference temperature

5) Essentially, the geometric exit area has now been reduced by this boundary layer displacement thickness to an effective exit area given by

$$A_{eff} = \pi (r_g - \delta^*)^2 \quad (E-10)$$

where

- A_{eff} = the effective exit area
- r_g = the geometric radius at the nozzle exit

6) Now, using this effective area ratio, steps 1) through 5) should be repeated until the effective area ratio resulting from step 5) is within tolerable limits of the area ratio used to begin step 1) of the same calculation set. This iterative procedure will yield as a final result, a completely coupled solution between the boundary layer and the free stream flow parameters. This iterative procedure converges rapidly so that, for divergence half-angles greater than 10 degrees, the average of the second and third iterations is usually sufficiently close to yield a completely coupled solution.

7) The total thrust from this particular configuration can now be calculated using the general thrust equation:

$$T = \dot{m} U_e \left(\frac{1 + \cos a_{eff}}{2} \right) + (P_e - P_{amb}) A_{ex} - F^* - F_c \quad (E-11)$$

where

- T = thrust
- \dot{m} = mass flow rate

a_{eff} = the nozzle divergence angle associated effective expansion area

P_e = static pressure at the nozzle exit

P_{amb} = ambient pressure at the nozzle exit

A_{ex} = the geometric area at the nozzle exit

F^* = throat drag

F_c = nozzle divergent cone drag.

The geometric area is used in the second term of the general thrust equation because, although the flow properties are determined by an expansion through the final effective area, it is reasonable to assume that the static pressure is constant across the boundary layer so that the pressure differential between the exit pressure and the ambient pressure acts across the entire geometric area.

From Neuringer, the throat drag can be calculated from

$$F^* = (0.208) (\dot{m})^{0.7} a^* (\pi r^* \mu^*)^{0.3} \left(\frac{T_s^*}{T_R^*} \right)^{0.55} \left(\frac{x_o}{r^*} \right)^{0.7} \quad (E-12)$$

where

a^* = acoustic speed at the throat

r^* = throat radius

μ^* = viscosity at the throat based on the throat static temperature

T_s^* = throat static temperature

T_R^* = throat reference temperature

x_o = assumed length of nozzle throat;

and the exit cone drag can be calculated from

$$F_c = \frac{0.7}{\beta^{0.7}} G (M_e) F^* \quad (E-13)$$

and

$$\beta = \frac{X_o a_{eff}}{r^*}$$

where

β = a geometric parameter

F^* = throat drag as given by equation (E-12)

$$G(M_e) = \int_1^{M_e} B(M) C(M) D(M) E(M) F(M) dM$$

$$B(M) = \left[\frac{\gamma + 1}{2 + (\gamma - 1) M^2} \right]^{\frac{0.7\gamma}{\gamma - 1}}$$

$$C(M) = \left[\frac{M^2 (\gamma + 1)}{M^2 (\gamma - 1) + 2} \right]^{0.85}$$

$$D(M) = \left\{ \frac{1}{M^{1/2}} \left[\frac{2}{\gamma + 1} \left(1 + \frac{\gamma - 1}{2} M^2 \right) \right]^{\frac{\gamma + 1}{4(\gamma - 1)}} + (\beta - 1) \right\}^{-0.3}$$

$$E(M) = \frac{1}{M^{1/2}} \left[\frac{2}{\gamma + 1} \left(1 + \frac{\gamma - 1}{2} M^2 \right) \right]^{\frac{\gamma + 1}{4(\gamma - 1)}}$$

$$F(M) = \frac{M^{1/2}}{2} \left[\frac{2}{\gamma + 1} \left(1 + \frac{\gamma - 1}{2} M^2 \right) \right]^{\frac{5-3\gamma}{4(\gamma-1)}} - \frac{1}{2M^{3/2}} \left[\frac{2}{\gamma-1} \left(1 + \frac{\gamma-1}{2} M^2 \right) \right]^{\gamma+1/4(\gamma-1)}$$

An example of the range of $G(M_e)$ for $\beta = 0.60$ is shown in figure E-8.

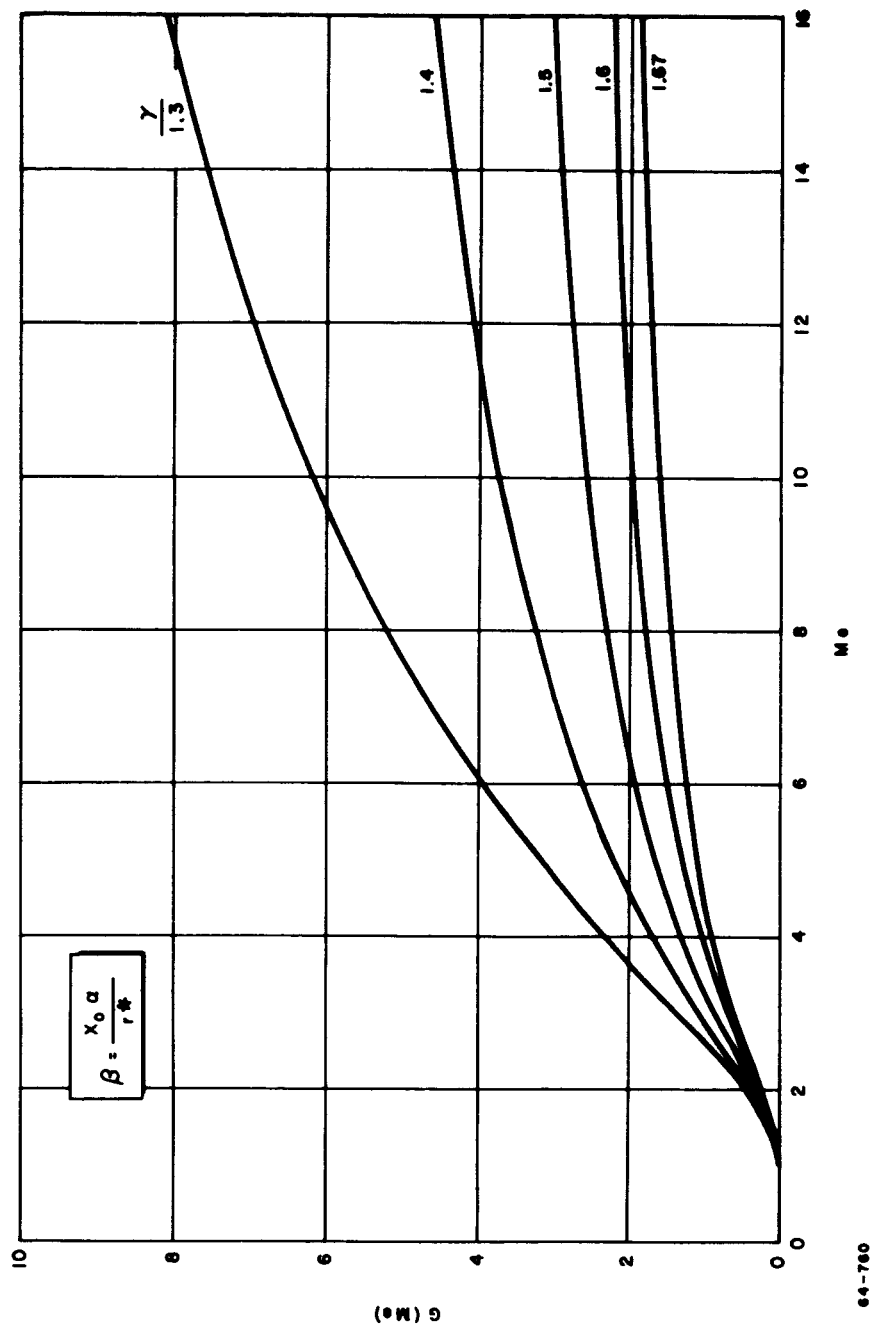


Figure E-8 NOZZLE EXIT CONE DRAG PARAMETER VARIATION WITH MACH NUMBER FOR $\beta = 0.6$

b. Results

A coupled solution, such as can be achieved by using the iterative procedure described previously, yields an expansion area reduction similar to that shown in figure E-9. For a given geometric area ratio, as the geometric expansion half angle increases, the percentage of area ratio reduction decreases. This is due to the larger boundary layer buildup associated with the longer nozzle required to yield the same geometric area ratio at a smaller divergence angle.

Figure E-10 is the result of the above conical optimizing procedure for a stagnation pressure of 2.88 atmospheres, a stagnation temperature of 2600°K , and an ambient or vent pressure of 1 mm Hg. It can be noted from the figure that the optimum conical nozzle area ratio is larger than 60, although little will be gained from a nozzle having an area ratio greater than 30. For any given area ratio, however, there is an optimum geometric exit cone half angle. If a larger divergence angle than this optimum angle is used, the directional loss causes decreased performance; if a smaller angle is used, the excessive friction associated with the longer nozzle becomes dominant.

The extension of this analysis to a conical nozzle with the same stagnation conditions, but operating in a space environment (ambient pressure equal to zero) is shown in figure E-11.

Qualitatively, little has changed between figures E-10 and E-11. The only difference is the increased performance for a given divergence angle and area ratio which is due to the larger influence of the $(P_e - P_{amb}) A_{ex}$ term in the general thrust equation (equation (E-11)). This increase is even greater for the larger area ratios because of the very large areas over which the pressure differential acts.

Figure 3 of the main text of this report is a comparison of the optimum performance in both the laboratory environment ($P_{amb} = 1$ mm Hg as in figure E-10) and the space environment ($P_{amb} = 0$ as in figure E-11). The main conclusion that can be drawn from this graph is that, for conical nozzles subject to the assumptions stated and with an area ratio in the range investigated, performance monotonically increases with increasing area ratio, although little is to be gained from an area ratio larger than 30.

c. Nonconical Nozzle Configurations

Although nozzle contouring was not investigated due to the difficulty in formulating and evaluating the necessary relations between pressure,

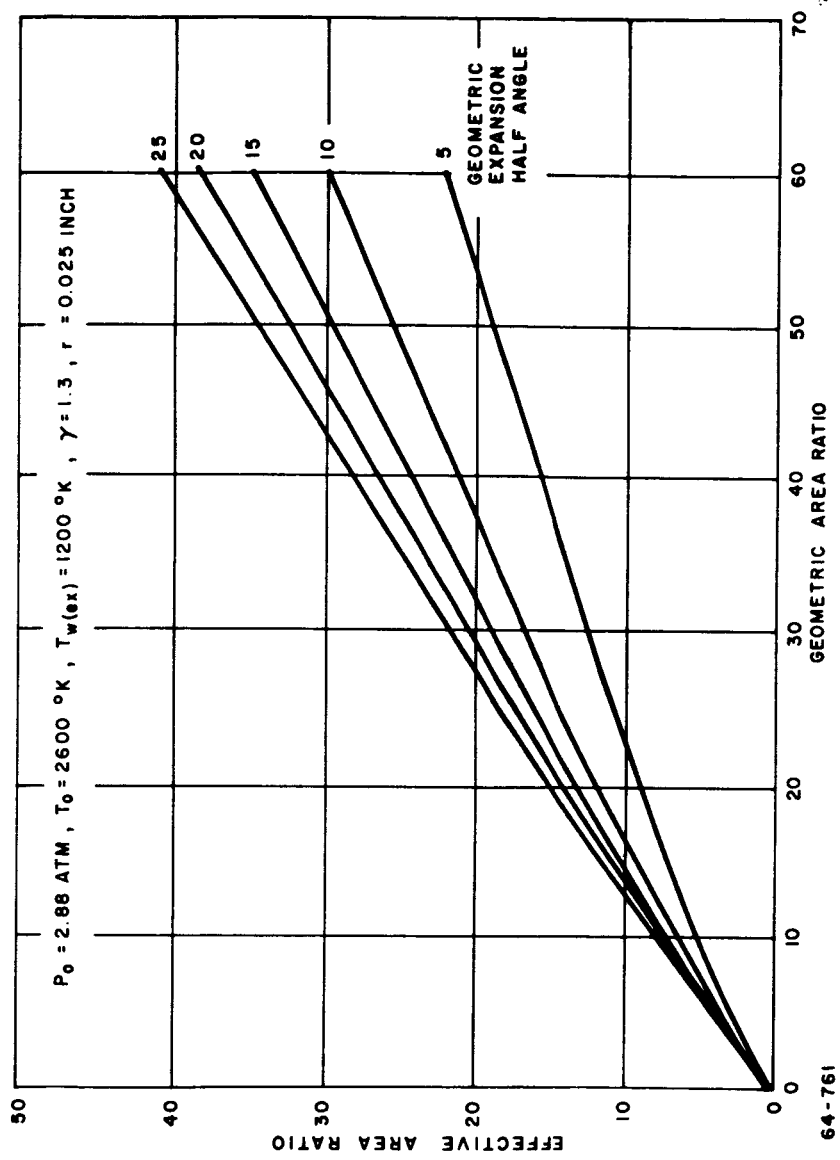
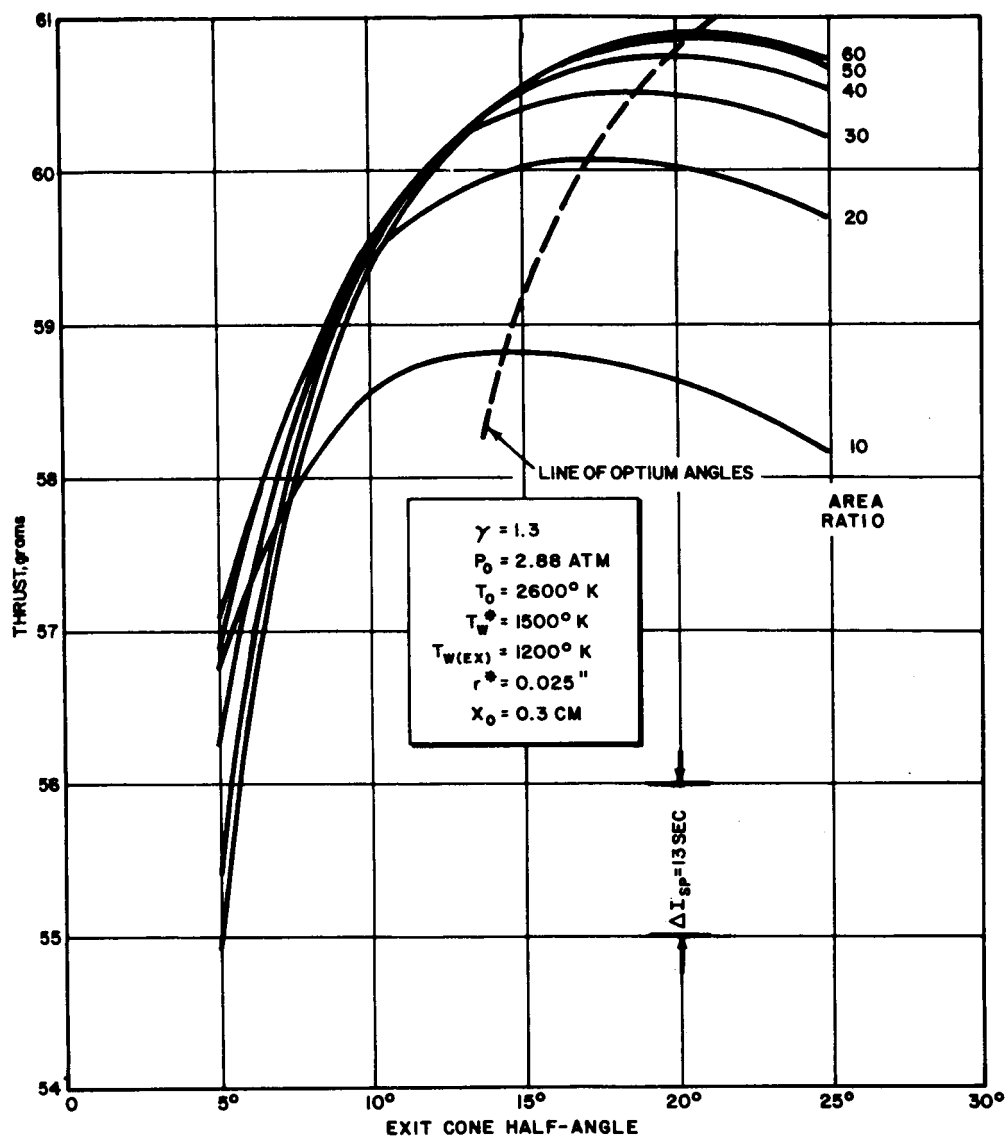
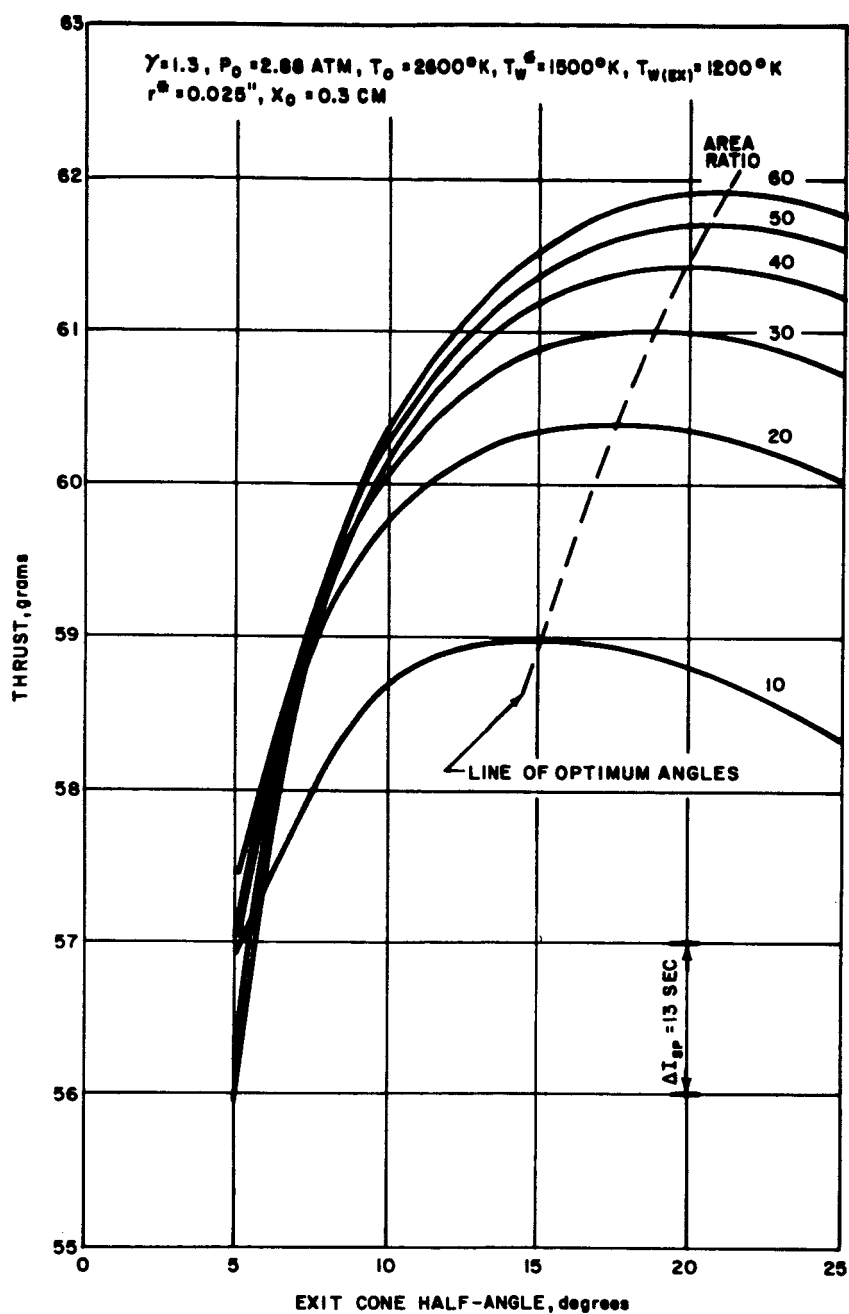


Figure E-9 EFFECT OF BOUNDARY LAYER DISPLACEMENT THICKNESS ON AREA RATIO



64-762

Figure E-10 THRUST VARIATION WITH EXIT CONE HALF ANGLE AT CONSTANT GEOMETRIC AREA RATIO, HYDROGEN. VENTING PRESSURE = 1 MM HG



64-763

Figure E-11 THRUST VARIATION WITH EXIT CONE HALF-ANGLE AT CONSTANT GEOMETRIC AREA RATIO FOR HYDROGEN. VENTING PRESSURE = 0

shear stress, and nozzle wall angle for an arbitrary contour, the following statement^{E-7} was investigated: For low Reynolds numbers, an exit nozzle should be horn-shaped rather than bell-shaped in order that the axial component of pressure on each element of nozzle surface area be greater than the axial component of the drag force, thereby producing a positive thrust element. Basically, the criterion states that, for any elemental area

$$P_s \sin \alpha > \tau_w \cos \alpha \quad (E-14)$$

where

P_s = local static pressure

τ_w = local shear stress

α = local expansion half-angle

The local shear stress was calculated using the formulation of Burke and Bird:

$$\tau_w = \frac{\rho_R U^2 (0.073)}{(Re_x) 0.3} \quad (E-15)$$

$$Re_x = \frac{\rho_R U_x}{\mu_R}$$

where

U = local fluid velocity

The local static conditions were found, using the reduced area ratio, while α was taken as the geometric expansion half-angle. The particular segment of a nozzle that was investigated was the exit plane of a conical nozzle currently being used with the resistojet- a nozzle with a throat diameter of 0.050 inch, an exit area ratio of 30, and a divergence half-angle of 15 degrees. The stagnation pressure and temperature were taken as 2.88 atmospheres and 2600°K respectively, and the wall temperature at this area ratio was assumed to be 1200°K. From figure E-9 the effective expansion area ratio for a geometric area ratio of 30, an expansion half-angle of 15 degrees, and the given stagnation conditions, is approximately 18.9. Using this area ratio and a ratio of specific heats of 1.3, the local static pressure becomes

$$P_s = \frac{(2.88 \text{ atm}) (1.013 \times 10^6 \text{ dynes/cm}^2/\text{atm}) (3.93 \times 10^{-3})}{\text{dynes/cm}^2} = 11.5 \times 10^3$$

and the local static temperature is $T_s = (2600^\circ\text{K}) (0.278) = 724^\circ\text{K}$. The axial component of pressure on this surface element is therefore $P_s (\sin 15 \text{ degrees}) = (11.5 \times 10^3 \text{ dynes/cm}^2) (0.259) = 2.98 \times 10^3 \text{ dynes/cm}^2$. This is to be compared to the axial component of shear which is calculated from equation (E-15). Since the density in this relation is based on the reference temperature, the static temperature is used only to calculate the reference temperature according to equation (E-8). Therefore, $T_R = 0.22 (2600 - 724) + 0.5 (1200 + 724) = 1374^\circ\text{K}$. The viscosity which corresponds to this temperature is approximately $2.4 \times 10^{-4} \text{ gm/cm-sec}$. Using the state equation, $\rho_R = P_s / RT_R = (11.5 \times 10^3 \text{ dynes/cm}^2) / (4.16 \times 10^7 \text{ ergs/gm-}^\circ\text{K}) 1374^\circ\text{K} = 2.01 \times 10^{-7} \text{ gm/cm}^3$. Again, from the isentropic flow tables, the Mach number at an area ratio of 18.9 is 4.15. The speed of sound at this point is $a^* = \sqrt{\gamma RT} = [(1.3) (4.16 \times 10^7) (724)]^{1/2} = 1.98 \times 10^5 \text{ cm/sec}$.

Therefore, the local fluid velocity is $8.22 \times 10^5 \text{ cm/sec}$. The axial distance from the throat to the exit plane is given by $x = (r_{\text{ex}} - r^*) / (\tan 15 \text{ degrees}) = (0.285 \text{ cm}) / (0.268) = 1.06 \text{ cm}$. The Reynolds number based on the axial length is $Re_x = (2.01 \times 10^{-7}) (8.22 \times 10^5) (1.06) / (2.4 \times 10^{-4}) = 730$ and $(Re_x)^{0.3} = 7.22$. Therefore, the shear stress at this particular area ratio is $\tau_w = (2.01 \times 10^{-7}) (8.22)^2 (10^{10}) (0.073) / (7.22) = 1.37 \times 10^3 \text{ dynes/cm}^2$. It follows that the axial component of shear is just $\tau_w (\cos 15 \text{ degrees}) = (1.37 \times 10^3) (0.966) = 1.32 \times 10^3 \text{ dynes/cm}^2$. Hence, the axial component of shear is much less than the axial component of pressure ($2.98 \times 10^3 \text{ dynes/cm}^2$) and the stated criterion has been fulfilled by the conical nozzle without resorting to a contoured shape of any kind. This result tends to validate the previously drawn conclusion that the optimum conical nozzle for the resistojet has an area ratio somewhat greater than 30. If the axial component of the shear stress was greater than the axial component of the pressure, then better performance could be attained by removing that portion of the nozzle where this relation between the stresses existed, that is, a smaller area ratio nozzle would be the optimum.

* These calculations have assumed a molecular weight of 2 and a ratio of specific heats, γ , of 1.3. These values were taken from an Avco computer program which evaluates the thermodynamic properties of hydrogen over a wide range of temperatures and pressures. Data from the program reveal that within a hydrogen temperature range of 2500 to 2700°K and a pressure range of 0.5 to 2.0 atmospheres, the molecular weight varies only between 1.95 and 2.00 while the frozen ratio of specific heats, γ_{froz} , varies between 1.30 and 1.31.

References

- E-1. Huff, V. N., S. Gordon, and V. E. Morrell, General Method and Thermodynamic Tables for Computation of Equilibrium Composition and Temperature of Chemical Reactions, NACA Report 1037 (1951).
- E-2. Liepmann, H. W. and A. Roshko, Elements of Gasdynamics, John Wiley and Sons, Incl., New York (1957).
- E-3. Neuringer, J. L., Calculation of the Total Turbulent Shear Force and Heat Transfer in a Conical Nozzled Arcjet Engine, Avco Technical Release, (8 June 1962).
- E-4. Thermal Arcjet Research, Prepared by EOS for the Air Force Aeropropulsion Laboratory, ASD-TDR-63-632 (15 August 1963).
- E-5. Burke, A. F., Turbulent Boundary Layers on Highly Cooled Surfaces at High Mach Numbers, Presented at ASD Symposium on Aeroelasticity (30 October 1961).
- E-6. Burke, A. F., and K. D. Bird, The Use of Conical and Contoured Expansion Nozzles in Hypervelocity Facilities, Proceedings of the Second Symposium on Hypervelocity Techniques, Plenum Press, New York (1962)
- E-7. Greco, R. V., and W. A. Stoner, Research and Development of a 1-kw Plasmajet Thrustor, AIAA Journal, 1, 2 (1963).

APPENDIX F

BIBLIOGRAPHY OF REFERENCES ON BORON NITRIDE

1. Ingles, T.A., and P. Popper, The Preparation and Properties of Boron Nitride, Special Ceramics, Heywood and Co., London (1960), p. 144-167.
2. Anon., High Temperature Technology Symposium, Stanford Research Institute, McGraw-Hill, New York (1960), p. 54-144.
3. O'Connor, T.E., J. Am. Cer. Soc., 84, (9), 1753 (1962).
4. Modylevskaya, K. D., M. D. Lyutaya, J. N. Nazarchuk, Zavodskaya Lab., 27, 1345 (1961).
5. Steptsov, V. M., and G. V. Samsonov, Voprosy Poroshkovoi Meti Prochnosti Materialov, Akad. Nauk. Ukr. S. S. R., 6, 65 (1958).
6. Belfort, D., S. Blum, B. Bovarnick, Nature 4779, 901 (3 June 1961).
7. Anon., Mat. in Design Eng., 57 (5), 91 (May 1963).
8. Dreger, L. H., V. V. Dadape, And J. L. Margrave, J. Phys. Chem. 66, 1556, (1962).
9. Hildebrad, D. L., and W. F. Hall, J. Phys. Chem. 67, 888 (1962).
10. Taylor, K. M., Industr. Engng. Chem. 47, 2506 (1955).
11. Ingles, T. A., and P. Popper, B. Ceram. R. A. Res Paper 398 (1958).
12. Kubaschewski, O., and E. Evans, Metallurgical Thermochemistry, Pergamon Press, London, (1958).

FINAL DISTRIBUTION LIST

CONTRACT NAS3-4101

<u>Addressee</u>	<u>No. of Copies</u>
NASA Lewis Research Center Mail Stop 21-5 21000 Brookpark Road Cleveland, Ohio 44135 Attn: H. Hunczak	12
NASA Lewis Research Center Spacecraft Technology Procurement Section 21000 Brookpark Road Cleveland, Ohio 44135 Attn: J. DeFord	1
NASA Lewis Research Center Library 21000 Brookpark Road Cleveland, Ohio 44135	1
NASA Lewis Research Center 21000 Brookpark Road Cleveland, Ohio 44135 Attn: J. Jack	1
NASA Ames Research Center Moffett Field, California 94035 Attn: Dr. G. Goodwin	1
NASA Ames Research Center Library Moffett Field, California 94035	1
NASA Goodard Space Flight Center Greenbelt, Maryland 20771 Attn: W. Isley Bldg. 6	1